Rochester Institute of Technology

RIT Digital Institutional Repository

Theses

11-1-2005

Pushing the limits of Hyper-NA optical lithography

Yongfa Fan

Follow this and additional works at: https://repository.rit.edu/theses

Recommended Citation

Fan, Yongfa, "Pushing the limits of Hyper-NA optical lithography" (2005). Thesis. Rochester Institute of Technology. Accessed from

This Dissertation is brought to you for free and open access by the RIT Libraries. For more information, please contact repository@rit.edu.

PUSHING THE LIMITS OF HYPER-NA OPTICAL LITHOGRAPHY

by

YONGFA FAN

A DISSERTATION

Submitted in partial fulfillment of the requirements
For the degree of Doctor of Philosophy
in
Microsystems Engineering
at the
Rochester Institute of Technology

November 2005

Author: ______________________________
Microsystems Engineering Program

Certified by: ______________________________
Bruce W. Smith
Intel Professor of Microelectronics Engineering

Approved by: ______________________________
Mustafa A.G. Abushagur
Director of Microsystems Engineering Program

Certified by: ______________________________
Harvey J. Palmer
Dean Kate Gleason College of Engineering

NOTICE OF COPYRIGHT

© 2005

Yongfa Fan

REPRODUCTION PERMISSION STATEMENT

Permission Granted

TITLE:

"PUSHING THE LIMITS OF HYPER-NA OPTICAL LITHOGRAPHY"

I, Yongfa Fan, hereby grant permission to the Wallace Library of the Rochester Institute of Technology to reproduce my dissertation in whole or in part. Any reproduction will not be for commercial use or profit.

Signature of Author: ______________________ Date: 11-8-2005

ABSTRACT

Kate Gleason College of Engineering

Rochester Institute of Technology

Degree Doctor of Philosophy **Program** Microsystems Engineering

Name of Candidate Yongfa Fan

Title PUSHING THE LIMITS OF HYPER-NA OPTICAL LITHOGRAPHY

The evolution of optical lithography to pattern smaller geometries was witnessed the shrinkage of source wavelength as a way to increase optical resolution. Shrinking of source wavelength into vacuum ultra-violet (VUV) faces a number of technical barriers with respect to imaging materials. Instead of source wavelength shrinking, the optical resolution can also be enhanced by increasing numerical aperture (NA) with immersion techniques. This dissertation is devoted to experimentally studying the imaging behaviors of hyper-NA optics in the context of liquid immersion and solid immersion lithography.

In this dissertation, the full-vector interference theory is described for two-beam and multi-beam interference. Polarization effects, resist absorption effects and BARC optimization are analyzed respectively. The experimental setup is analyzed in consideration of vibration, source temporal coherence and spatial coherence. Imaging with TE and TM polarization is studied respectively. A solid immersion technique is investigated experimentally to push the NA beyond what are available using fluids and imaging at NA values up to the index of the photoresist has been investigated. Moreover, NA values have been pushed higher than the refractive index of the resist, exposing resist using "evanescent wave imaging". This approach removes the index of a photoresist as a physical resolution limit, opening up new possibilities of resolution enhancement.

The ultimate resolution limits of optical lithography have been discussed for a long time but the limits have not been met yet. The achievements in this dissertation have shed light on this long-sought curiosity in the lithography community. Our experimental results proved the feasibility of 25 nm regime optical lithography. However, resolution beyond that would require innovations on higher index imaging materials, which are believed to be very limited.

Air bubble induced light scattering effects on lithographic imaging have also been studied using geometrical optics and Mie scattering model. Lithographic imaging of "bubbles" in an immersion water gap was studied by mimicking air bubbles with polystyrene spheres. By counting the number of "bubbles" which are actually imaged and evaluating the number which are present in the optical path, the distance beyond which bubbles will not print can be estimated.

Abstract Approval:	Committee Chair	Bruce W. Smith
	Program Director	Mustafa A. Abushagur
	Dean KGCOE	Havery Palmer

DISSERTATION APPROVAL FORM

Submitted by Yongfa Fan in partial fulfillment of the requirements for the degree of Doctor of Philosophy in Microsystems Engineering and accepted on behalf of the Rochester Institute of Technology by the dissertation committee.

We, the undersigned members of the Faculty of the Rochester Institute of Technology, certify that we have advised and/or supervised the candidate on the work described in this dissertation. We further certify that we have reviewed the dissertation manuscript and approve it in partial fulfillment of the requirements of the degree of Doctor of Philosophy in Microsystems Engineering.

Bruce W. Smith ______ 11/18/05 ______ Committee Chair
(Date)

______________________ Advisor (if different from Chair)

Santosh K. Kurinec ______________________

Karl D. Hirschman ______________________

Mustafa A. G. Abushagur ______________________

Donis G. Flagello ______________________

Mustafa A. G. Abushagur ______________________ Ph.D. Program Director

Harvey Palmer ______________________ Kate Gleason College of Engineering Dean

ACKNOWLEDGEMENTS

First of all, I would like to thank my advisor, Dr. Bruce W. Smith, for giving me the opportunity to be his student. Under his influence and guidance, I entered this marvelous world of optical lithography engineering, which I have enjoyed working on with great enthusiasm and great success. I clearly remember that my first year classes with Dr. Smith had kindled so much of my interest in optical lithography. Over the course of completing this dissertation, his guidance, advice, insight and encouragement were essential in moving my research from one stage to the next. Many a time, he shared the happiness of success with me. Definitely, my experience in Dr. Smith's group will benefit me for a life long time.

My special thanks are given to Dr. Donis Flagello for his invaluable discussions on vector interference theory, solid immersion issues, as well as the whole structure of the dissertation. His precious time is greatly appreciated. My thanks are also given to Dr. Mustafa A. G. Abushagur, Dr. Santosh K. Kurinec and Dr. Karl D. Hirschman for their time serving in my dissertation advisory committee.

I am grateful to all the staff members from Semiconductor & Microsystems Fabrication Laboratory at RIT. Special thanks are given to John Nash and Bruce Tolleson who have given me a lot of help with our experimental facilities. Without their support, it would not to possible to complete my research experiments. Their hard work has made the laboratory an excellent place for education and research.

I would like to acknowledge all the members in Dr. Smith's group, Anatoly Bourov, Frank Croponese, Neal Lafferty, Andrew Estroff, Lena Zavyolova, Jianming

Zhou, Michael Slocum, James Park and Emil Piscani, for their valuable support in completing this dissertation, as well as the time together which made my life at RIT enjoyable, unforgettable.

Thanks to SRC for the generous funding. Thanks to Rohm & Haas, AZ Electronic Materials, Brewer Science, and TOK for the use of their excellent materials. Also, thanks to Lambda Physik for the 193-nm excimer laser.

Finally, I would like to thank my parents, my sister and brothers for their consistent support, understanding, encouragement and endless love.

TABLE OF CONTENTS

LIST OF ACRONYMS x

LIST OF FIGURES xi

LIST OF TABLES xx

1. INTRODUCTION 1

1.1 Basics of optical lithography 2

1.2 Resolution enhancement technologies 5

1.3 Motivation of this dissertation 12

1.4 Research directions 16

2. VECTOR INTERFERENCE THEORY 19

2.1 Introduction 19

2.2 Interference imaging 20

2.3 Light propagation in a stack of thin films 26

2.4 Summary 35

3. NUMERICAL ANALYSIS OF HYPER-NA INTERFEROMETRIC LITHO 36

3.1 Introduction 35

3.2 Polarization effects at hyper-NA interferometric imaging 36

3.3 BARCs for hyper-NA imaging 46

3.4 Resists for hyper-NA imaging 50

3.5 Summary 53

4. EXPERIMENTAL APPROACH 54

4.1 Introduction 54

4.2 Setup for 2-beam interferometric immersion lithography 54

4.3 Half cylinders, half balls and prisms 56

4.4 Illumination source 58

4.5 Polarization control 59

4.6 Summary 60

5. ANALYSIS OF THE EXPERIMENTAL SETUP CONFIGURATION 61

5.1 Introduction 61

5.2 Effects of beam pointing instability on imaging 61

5.3 Temporal coherence considerations 74

5.4 Spatial coherence considerations 79

5.5 Summary 80

6. EXPERIMENTAL INVESTIGATION OF HYPER-NA EFFECTS IN PHOTORESIST 82

6.1 Introduction 82

6.2 Experimental methods 83

6.3 Experimental results and discussion 86

6.4 Summary 100

7. EXPERIMENTAL INVESTIGATION OF SOLID IMMERSION 102

7.1 Introduction 102

7.2 Theoretical considerations 103

7.3 Experimental methods 108

7.4 Results and discussion 110

7.5 Summary 122

8. AIR BUBBLE INDUCED LIGHT SCATTERING EFFECTS ON IMAGE QUALITY IN 193 nm IMMERSION LITHOGRAPHY 123

8.1 Introduction 123

8.2 Geometrical optics model of bubble scattering 125

8.3 Exact computation of scatter 127

8.4 Scattering measurements 136

8.5 Lithographic imaging of "bubbles" 138

8.6 Summary 143

9. CONCLUSIONS 145

APPENDIX A1: A brief description of ILSim 148

APPENDIX A2 Programming Flowchart for ILSim 154

REFERENCES 155

LIST OF ACRONYMS

ArF	Argon Fluoride
BARC	Bottom Anti-Reflection Coating
CD	Critical Dimension
DOF	Depth Of Focus
DUV	Deep Ultra Violet
EUV	Extreme Ultra Violet
HPLC	High Performance Liquid Chromatography
NA	Numerical Aperture
OAI	Off-Axis Illumination
OPC	Optical Proximity Correction
PAB	Post Apply Bake
PEB	Post Exposure Bake
PMMA	Poly-Methyl Methacrylate
PSM	Phase Shifting Mask
PST	Polystyrene
RET	Resolution Enhancement Technologies
TE	Transverse Electric
TM	Transverse Magnetic
VASE	Variable Angle Spectroscopic Ellipsometry
VUV	Vacuum Ultra-Violet

LIST OF ILLUSTRATIONS

Figure 1.1 Illustration for optical contact/proximity printing lithography and optical projection lithography........ 3

Figure 1.2 Definition of θ, the half angle subtended by the objective lens at the image plane........ 5

Figure 1.3 Illustration for on-axis and off-axis illumination........ 6

Figure 1.4 Examples of off-axis illumination schemes........ 8

Figure 1.5 Schematic for the diffraction of a binary mask and the correspondent alternating phase shift mask........ 10

Figure 1.6 Schematic for the diffraction of a chromeless phase shifting mask and an attenuated phase shift mask........ 11

Figure 1.7 Comparison of the resist images from mask pattern without OPC and with OPC........ 12

Figure 2.1 Interference of two monochromic plane waves with TE with equal oblique angle θ........ 22

Figure 2.2 Interference of two monochromic plane waves with TM with equal oblique angle θ........ 24

Figure 2.3 Thin film stack on a substrate with incident plane wave........ 29

Figure 2.4 Relationship between x and z components for reflection and transmission coefficients of a TM polarized wave incident on a stack of thin films........ 32

Figure 3.1 Two-Beam interferometric imaging at a wavelength of 193 nm in a uniform media with refractive index of 1.70........ 39

Figure 3.2 Intensity contours versus resist film thickness Z and lateral position X for 0.5NA two-beam interference. 43

Figure 3.3 Intensity contours versus resist film thickness Z and lateral position X for 0.8NA two-beam interference. 43

Figure 3.4 Intensity contours versus resist film thickness Z and lateral position X for 1.0NA two-beam interference 44

Figure 3.5 Intensity contours versus resist film thickness Z and lateral position X for 1.2NA two-beam interference 44

Figure 3.6 Intensity contours versus resist film thickness Z and lateral position X for 1.4NA two-beam interference 45

Figure 3.7 Intensity contours versus resist film thickness Z and lateral position X for 1.6NA two-beam interference 45

Figure 3.8 Reflectance at the BARC-resist interface versus BARC thickness at various refractive indices of BARC materials for 1.40 NA imaging 49

Figure 3.9 Illustration for the oblique beam which experiences a longer path in the resist film than the film thickness 51

Figure 3.10 Simulation results of light intensity distribution within the resist layer for two-beam interference 52

Figure 4.1 Schematic of interferometric immersion lithography setup 55

Figure 4.2 Photography of the interferometric immersion lithography setup 55

Figure 4.3 Aluminum oxide half cylinder used for high NA coupling. 56

Figure 4.4 Equilateral triangle aluminum oxide prism used for high NA coupling 57

Figure 4.5 A schematic of Rochon polarizer. 59

Figure 5.1 Shift of interference fringe from tilted beam relative to that from normal beam, causing imaging blurring 62

Figure 5.2 A schematic showing laser beam tilt 63

Figure 5.3 Fringe phase shift versus laser beam tilt angle 66

Figure 5.4 Fringe phase shift versus laser beam tilt angle 67

Figure 5.5 Fringe phase shift versus laser beam tilt angle. 68

Figure 5.6. Illustration for interference fringe contrast loss due to fr‘nge pitch change from tilted beam 70

Figure 5.7 Tilt coherence length versus laser beam tilt angle 71

Figure 5.8 Interference fringe contrast versus the standard deviation 73

Figure 5.9 Beat frequency (1/L) normalized to $2n/\Delta l_c$ versus the first diffraction order angle α and oblique angle θ. 77

Figure 5.10 Interference contrast versus the distance from field center at various NA values. The source has a wavelength of 193nm and a temporal coherence length of 7 mm. The grating pitch is 600 nm 78

Figure 5.11 Illustration of a wafer with a displacement of d from the “focal plane” 79

Figure 6.1 Characterization of resist line cross-sections. 84

Figure 6.2 Illustration for the effectiveness of side develop technique 86

Figure 6.3 SEM photographs and simulation results for 1.05NA, TE polarization using resist assembly in Table 6.3 88

Figure 6.4 SEM photographs and simulation results for 1.05NA, TM polarization using resist assembly in Table 6.3 90

Figure 6.5 Fringe contrast versus resist thickness for the simulations results shown in Figure 6.4 (d). 91

Figure 6.6 Reflection as a function of incident angle of TE polarization for two single layer BARC's and a bi-layer BARC 93

Figure 6.7 SEM photographs two-beam interferometric lithography with TE polarization using the resist film assembly in Table 6.6 94

Figure 6.8 Numerical calculation and SEM cross-sectional photograph of two-beam interferometric lithography with TE polarization at 0.7NA, 69 nm half pitch 96

Figure 6.9 Numerical calculation and SEM cross-sectional photograph of two-beam interferometric lithography with TE polarization at 0.8NA, 60 nm half pitch 97

Figure 6.10 Numerical calculation and SEM cross-sectional photograph of two-beam interferometric lithography with TE polarization at 0.9NA, 53 nm half pitch 97

Figure 6.11 Numerical calculation and SEM cross-sectional photograph of two-beam interferometric lithography with TE polarization at 1.05NA, 45 nm half pitch 98

Figure 6.12 Numerical calculation and SEM cross-sectional photograph of two-beam interferometric lithography with TE polarization at 1.35NA, 35 nm half pitch 99

Figure 6.13 Numerical calculation and SEM cross-sectional photograph of two-beam interferometric lithography with TE polarization at 1.50NA, 32 nm half pitch 100

Figure 7.1 Illustration of a gap between the solid material and the resist film due to surface topography. 104

Figure 7.2 Analysis of gap transmittance for solid immersion at wavelength of 193nm for various NA values 105

Figure 7.3 Relative light intensity distribution in the resist at various air gap thickness 107

Figure 7.4 Mechanical fixture is used to hold the resist wafer against one lateral of the equilateral triangle prism 109

Figure 7.5 Photography of the mechanical fixture for solid immersion 109

Figure 7.6 Illustration for measuring light that is coupled into the resist 110

Figure 7.7 Visible appearance of the interface before and after pressure application 111

Figure 7.8 Reflectance at the resist-sapphire interface versus air gap thickness using parameters in Table 7.3 112

Figure 7.9 BARC thickness calculation for resist stack in Table 7.4 113

Figure 7.10 SEM for 1.42 NA, 34nm half/pitch, TE polarization using film stack in Table 7.4 114

Figure 7.11 Light intensity distribution within the resist layer for 1.4NA using TE polarization 114

Figure 7.12 BARC thickness calculation for resist stack in Table 7.5 115

Figure 7.13 SEM for 1.60NA, 30 nm half/pitch, TE polarization using film stack in Table 7.5 116

Figure 7.14 Light intensity distribution within the resist layer for 1.60NA using TE polarization ... 116

Figure 7.15 BARC thickness calculation for resist stack in Table 7.5 but for 1.66NA .. 116

Figure 7.16 SEM for 1.66NA, 29 nm half/pitch, TE polarization using film stack in Table 7.5 ... 117

Figure 7.17 Light intensity distribution within the resist layer for 1.66NA using TE polarization ... 117

Figure 7.18 Illustration for homogeneous propagation region and evanescent wave region ... 119

Figure 7.19 Energy percentage Coupled into photoresist versus NA in an aluminum oxide final lens element system ... 120

Figure 7.20 Light intensity distribution within the resist layer for 1.85NA using TE polarization ... 121

Figure 7.21 SEM for 1.85NA, 26 nm half/pitch, TE polarization using film stack in Table 7.6 ... 121

Figure 8.1 Reflection of a ray from a spherical bubble in water. Total reflection occurs when the incident angle i is larger than the critical angle ... 126

Figure 8.2 Lateral distribution of relative scattered irradiance of an air bubble in diameter of 2 μm from various distances from the bubble. ... 128

Figure 8.3 Lateral distribution of relative scattered irradiance of polystyrene sphere 2 μm in diameter from various distances from the bubble ... 129

Figure 8.4 Lateral distribution of relative scattered irradiance of a PMMA sphere 2 μm in diameter from various distances from the bubble ... 130

Figure 8.5 Distribution of relative scattered irradiance of an air bubble 2 μm in diameter in water. 130

Figure 8.6 Distribution of relative scattered irradiance of a polystyrene sphere 2 μm in diameter in water. 130

Figure 8.7 Distribution of relative scattered irradiance of a PMMA sphere 2 μm in diameter in water. 130

Figure 8.8 Distribution of relative scattered irradiance of an air bubble 1 μm in diameter in water. 130

Figure 8.9 Distribution of relative scattered irradiance of an air bubble 0.5 μm in diameter in water. 133

Figure 8.10 Distribution of relative scattered irradiance of 2 air bubbles 2 μm in diameter separated by 100 μm in water under unpolarized irradiation. 133

Figure 8.11 Distribution of relative scattered irradiance of 2 air bubbles 2 μm in diameter separated by 100 μm in water under TE-polarized irradiation. 134

Figure 8.12 Distribution of relative scattered irradiance of 2 air bubbles 2 μm in diameter separated by 100 μm in water under TM-polarized irradiation. 134

Figure 8.13 Distribution of relative scattered irradiance of an air bubble 2 μm in diameter in water illuminated by two oblique (±56°) beams without polarization 135

Figure 8.14 Distribution of relative scattered irradiance of an air bubble 2 μm in diameter in water illuminated by two oblique (±56°) beams with TE-polarization 136

Figure 8.15 Distribution of relative scattered irradiance of an air bubble 2 μm in diameter in water illuminated by two oblique (±56°) beams with TM-polarization 136

Figure 8.16 Measured relative scattered irradiance of PST beads (2 μm in diameter, 2×10^{-4} %) at 10° off the forward direction 137

Figure 8.17 Mie Scattering calculation for PST beads (2 μm in diameter), at 10° off the forward direction 138

Figure 8.18 Set-up for direct lithographic imaging of "bubbles" 140

Figure 8.19 Total number of "bubbles" in optical path versus total number eventually imaged 140

Figure 8.20 SEM pictures of a PST sphere and their image in resist 141

Figure 8.21 Interferometric system for "bubble" imaging 142

Figure 8.22 Set-up for two-beam interference through scattering media 142

Figure 8.23 Interferometric image in water suspended with polystyrene beads of 2 μm diameter at $5\text{x}10^{-5}$ weight concentration 142

Figure 8.24 Interferometric image in water suspended with polystyrene beads of 0.5 μm diameter at $2.5\text{x}10^{-5}$ weight concentration 143

Figure A1-1 Graphical interface of ILSim 152

Figure A1-2 Image in immersion media. 152

Figure A1-3 2-D image in resist 152

Figure A1-4 2-D image in resist. 152

Figure A1-5 3-D image in resist 152

Figure A1-6 Image contrast in resist 152

Figure A1-7 2-Pass, orthogonal pol., top down 152

Figure A1-8 2-Pass, orthogonal pol., cross-section.. 153

Figure A1-9 Substrate (BARC) reflection.. 153

Figure A1-10 Top surface reflection 153

LIST OF TABLES

Table 1.1 2004 ITRS lithography technology requirements 2

Table 3.1 Optical constants and film thickness for resist assembly used for simulation in section 3.2.1 42

Table 6.1 A set of resist processing parameters 85

Table 6.2 Refractive indices of some materials at 193-nm 85

Table 6.3 Resist Film stack for polarization study 87

Table 6.4 Resist film stack for 1.05NA and 1.30NA 94

Table 6.5 Resist film stack used for 0.7-1.05NA 95

Table 6.6 Resist film stack used for 1.35-1.50NA 98

Table 7.1 Optical constants and film thickness for resist assembly used for analysis in Figure 7.2 107

Table 7.2 Optical constants and film thickness for resist assembly used for analysis in Figure 7.3 107

Table 7.3 Film stack used for measuring gap thickness 112

Table 7.4 Resist film stack used for 1.42NA 113

Table 7.5 Resist Film stack used for 1.60NA 115

Table 7.6 Resist Film stack used for 1.85NA 121

Table A1-1 Summary of ILSim's inputs and outputs 148

Table A1-2 Simulation parameters for Example A1-2146 150

Table A1-3 Simulation parameters for Example A1-2 150

CHAPTER 1 INTRODUCTION

The advance of semiconductor industry has cultivated the advent of Information Technology era, which has had significant impact on people from all walks of life around the globe. Currently, the semiconductor industry is mainly involved with manufacturing of integrated circuits which have found their applications in computing, telecommunication, aerospace technologies etc. Poised as the next phase of the semiconductor revolution is microsystems technology, which integrates micro-scale, even nano-scale sensors, probes, lasers, and actuators into a single chip capable of sensing, analyzing, and communicating.[1] The technology will find applications in the areas of telecommunications, imaging, electronics, and biomedical diagnostics and treatment. The manufacturing of integrated circuits and microsystems involves microfabrication, the process of making micro-scale and nano-scale devices. One cornerstone of microfabrication is optical lithography. The evolvement of optical lithography to pattern smaller geometries is mainly responsible for the observation of Moore's law: the number of transistors per unit area on an integrated circuit is doubled every 12-18 months while the cost holds constant.[2]

International Technology Roadmap for Semiconductors (ITRS), the most widely cited strategic plan for semiconductors industry, identifies the challenges and needs facing semiconductor industry in the future. Its projections for some of the lithography technology requirements are listed in Table 1.1. Currently, the technology node of 90 nm

half pitch (half the distance between repeating structures, abbreviated as hp) is under projection. The 65nm half pitch technology node will under production in 2007, the 45 nm half pitch in 2010, the 32 nm half pitch in 2013 and the 22 nm half pitch in 2016. One of the technology concerns is when the transition from optical lithography to other innovative patterning technology will be needed. Since the resolution of optical lithography is diffraction limited, the physical resolution limit will be met sooner or later. Therefore, alternative non-optical lithographic technologies are being developed to replace optical lithography. However, this dissertation is dedicated to increasing the life of optical lithography by extending the optical resolution limits.

Table 1.1 2004 ITRS lithography technology requirements*

Year of production	2004	2007	2010	2013	2016
Technology node	hp90	hp65	hp45	hp32	hp22
DRAM ½ pitch (nm)	90	65	45	32	22
DRAM Contact in resist (nm)	110	80	55	40	30
MPU 1 ½ pitch (nm)	90	65	45	32	22
MPU Contact in resist (nm)	122	80	59	42	30
ASIC ½ pitch (nm)	90	65	45	32	22
ASIC Contact in resist (nm)	122	80	59	42	30

* http://public.itrs.net/

1.1 Basics of Optical Lithography

The first generation of optical lithography is proximity/contact printing, as illustrated in Figure 1.1 (a).[3] The mask is placed in contact or close proximity to the wafer. Upon exposure, the geometric shadow of the mask is formed on the resist. After development, the mask patterns are transferred to the resist film on the wafer. Thereafter, the resist patters are transferred to the underlying material layers in the subsequent processing procedures. In the case of contact printing, the masks are in contact with resist film, inevitably causing mask damages and subsequent yield loss. Proximity printing can avoid mask damages problems but the necessary gap dimensions (a few microns) limit

the minimum feature size that could be printed since further propagation of the mask geometrical shadow results in a distorted image due to Fresnel diffraction. Those issues

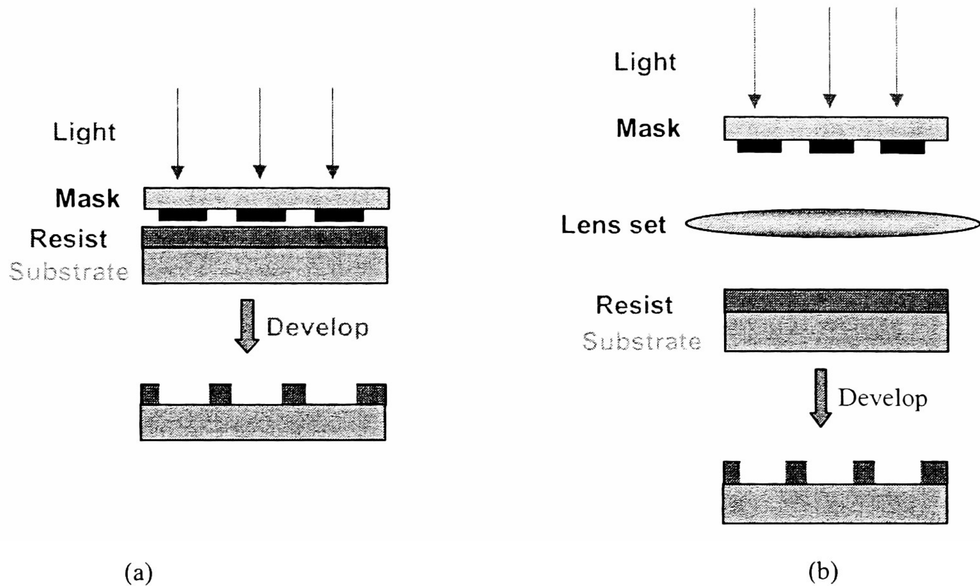

Figure 1.1 Illustration for optical contact/proximity printing lithography and optical projection lithography. (a) Contact/proximity printing; (b) Optical projection lithography.

can be resolved with the adoption of an optical projection system, where the optical image of the mask is projected onto the wafer through a set of lenses, as illustrated in Figure 1.1 (b).[3] Another advantage associated with projection printing is that the reduction optics can be used, thus alleviating the difficulties of mask masking.

The performance of an optical projection system can be characterized by two parameters, *Resolution* and *Depth Focus (DOF)*.[4] The resolution is described by Rayleigh's criterion

$$R = \frac{k_1 \lambda}{n \sin \theta} = \frac{k_1 \lambda}{NA} \qquad [1\text{-}1]$$

where R is the minimum resolvable dimension (also known as critical dimension, CD), λ is the vacuum wavelength of imaging source, n is the refractive index of the imaging media, θ is the half angle subtended by the objective lens at the image plane (as

illustrated in Figure 1.2), *NA* is knows as the numerical aperture, k_1 is a process dependent factor. The depth of focus based Rayleigh's criterion takes the form of

$$DOF = \pm\frac{k_2\lambda}{n\sin\theta^2} = \pm\frac{k_2 n\lambda}{NA^2} \qquad [1\text{-}2]$$

where k_2 is also a process dependent factor. Rayleigh's criterion indicates that the minimum resolvable dimension is directly proportional to the wavelength of the source and inversely proportional to the numerical aperture of the objective lens. Thereby, it is straightforward to increase resolution by employing shorter wavelength sources and larger aperture lenses. As a matter of fact, advances in optical lithography over the past decades witnessed the shrinking of source wavelengths, namely *g*-line (436nm), *i*-line (365nm), KrF(248nm), ArF(193nm), F2(157nm), EUV(13nm). With ArF(193nm) lasers as the workhorse in the current production lines, researchers are aiming at F_2(157nm) and EUV(13nm) as the natural extension of the current generation lithography.[5-19] Unfortunately, at those wavelengths, the inherent properties of high energy photons have generated a plethora of technical barriers to lithographic practice with respect to imaging, masking, especially pellicle materials. Foremost among those technical barriers is the lack of transparent materials in this portion of the electromagnetic spectrum. In addition, the performance of those sources is still needed to be improved. Those have made the extension of optical lithography without switching to a shorter wavelength appear more important.

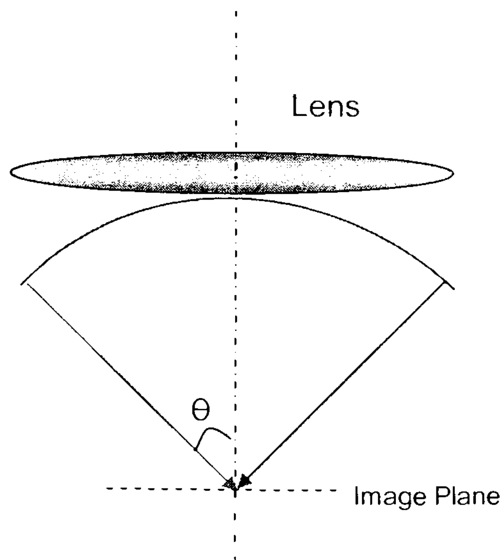

Figure 1.2 Definition of θ, the half angle subtended by the objective lens at the image plane. $NA=n\sin\theta$ is known as the numerical aperture, where n is the index of the imaging media.

1.2 Resolution Enhancement Technologies

While solutions are pursued to break down those barriers associated with shorter wavelength lithography, alternative approaches are being actively exploited to afford higher resolution without resorting to a shorter wavelength. Imaging at high numerical apertures is one of the approaches. The newly developed, very high NA 193-nm lenses (NA>0.85) have made it possible to print 65 nm critical dimension features, for which 157-nm lithography had been positioned. The extension of optical lithography without switching to a shorter wavelength transition is as well ascribed to Resolution Enhancement Technologies (RETs), including Off Axis Illumination (OAI), Phase Shift Masking (PSM) Optical Proximity Correction (OPC), etc. A brief review of those technologies is given in the following subsections.

1.2.1 Off Axis Illumination[20-30]

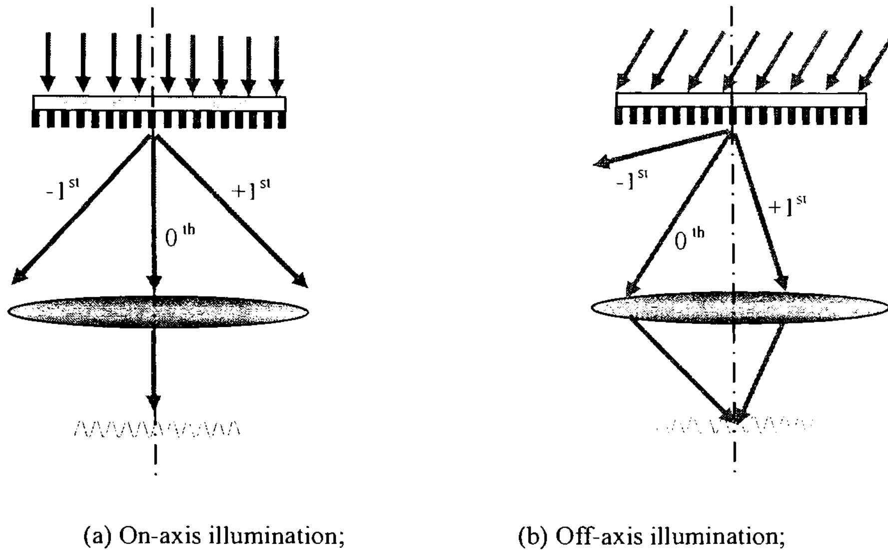

(a) On-axis illumination; (b) Off-axis illumination;

Figure 1.3 Illustration for on-axis and off-axis illumination. With on-axis illumination, only the zero diffraction order is collected by the lens. With off-axis illumination, both zero and first diffraction orders can be collected by the lens.

For a simple grating mask, the illuminating beam is split into discrete diffraction orders, some of which may be collected by the objective lens, subsequently forming an image of the mask in the wafer plane. With normally incident illumination on the mask, the objective lens may collect only the zero order if the grating pitch is small enough, as illustrated in Figure 1.3 (a), which is a resolution limiting case due to diffraction since one plane wave (the zero order) will not produce any spatial modulation on the wafer plane. However, with obliquely incident illumination on the mask, it is possible that both the zero and first orders enter the entrance pupil of the objective lens, as illustrated in Figure 1.3 (b), where the zero order is shifted to one side of the entrance pupil while the other side is able to capture the first order. At the wafer plane, the interference of the zero and the first order forms a sinusoidal fringe, an image of the grating mask. The foregoing

simple analysis shows that off-axis illumination can increase the resolution of an optical projection system.

In addition to a resolution boost, off-axis illumination also will enhance depth-of-focus. For on-axis illumination, the depth-of-focus is defined as the defocus distance at which the wavefront phase difference between the zero order and an order that is just captured by the margin of the entrance pupil is $\frac{\pi}{2}$. With this phase difference, the two orders do not interference at this defocus. For the case of off-axis illumination illustrated in Figure 1.3 (b), the phase difference at the defocus between the zero order and the first order is always smaller than that in the case of on-axis illumination. Therefore, a larger depth-of-focus is obtained with off-axis illumination. Actually, if the zero and the first orders are distributed symmetrically on the entrance pupil, the depth-of-focus will be infinite, an optimal situation for off-axis illumination. From the grating equation, it is found that this will occur when the illumination oblique angle θ_0 is expressed as

$$\sin(\theta_0) = \frac{\lambda}{2p} \qquad [1\text{-}3]$$

where λ is the illumination wavelength and p is the grating pitch. Equation [1-3] indicates that the optimal off-axis illumination is a function of mask dimension. As a matter of fact, a mask pitch that is just a little larger than the optimized pitch is imaged with less DOF than the optimized feature size. The worst case is when the diffraction order is in the center of the entrance pupil, as no benefits of focus enhancement is received. This worst pitch ($p = \frac{\lambda}{\sin(\theta_0)}$), the so-called "forbidden" pitch, is exactly twice the pitch that is optimized with this illumination. It should be avoided during circuit design.

For the simple off-axis illumination example described above, it is noted that the features that are perpendicular to the plane of the illumination is better resolved while the features that are parallel to the plane of the illumination do not gain any enhancement in resolution. To accommodate various mask feature orientations, the illumination must be configured accordingly. Geometrical shapes of the apertures that could be used to shape the illumination are used to represent the illumination configuration. A few examples of illumination configurations are sketched in Figure1.4. Figure 1.4 (a) represents dipole illumination, which only enhances resolution in one orientation. Quadrupole illumination, as illustrated in Figure 1.4(b), can boost resolution for both vertical and horizontal orientations. Annular illumination depicted in Figure 1.4 (c) works best for arbitrary orientations.

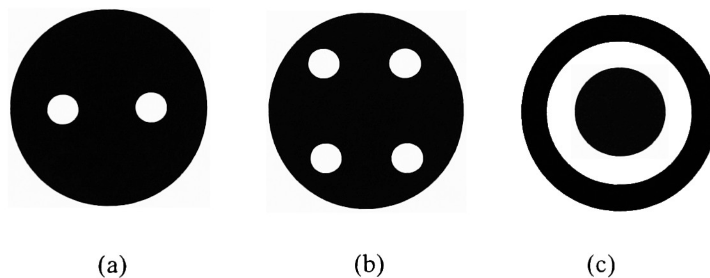

Figure 1.4 Examples of off-axis illumination schemes. (a) dipole illumination; (b) quadrupole illumination; (c) Annular illumination.

The above analysis for periodic mask patterns leads to the optimal off-axis illumination condition for a certain mask pitch. For isolated lines, off-axis illumination can not be optimized to enhance depth-of-focus since the diffraction of an isolated line consists of a continuous broad angle spectrum, of which only an extremely small portion

falls into the optimal angle. In general, off-axis illumination minimally enhances depth-of-focus of isolated lines.

1.2.2 Phase Shift Masking[31-38]

In addition to amplitude, phase information also plays an important role in diffraction and interference. Therefore, the manipulation of mask phase information may allow improved imaging. The diffraction of a binary grating mask and the correspondent alternating phase shift mask is depicted in Figure 1.5. The binary mask contains amplitude information but no phase information, as shown in Figure 1.5 (a). The corresponding alternating phase shifting mask adds a "phase shifter" over every other space to shift the phase of the light by 180°, as shown in Figure 1.5 (b). In the resolution limit case of the binary mask, only the zero and the first orders pass through the lens, with the first order diffraction angle $\sin\theta = \pm\frac{\lambda}{p}$. The interference of the zero with the first orders produces the image of the grating mask. Now consider the situation of the corresponding alternating shifting mask. Due to destructive interference of light passing through adjacent spaces, the zero order vanishes. The interference of the first orders produces the image of the grating mask. The first orders order are diffracted at $\sin\theta = \frac{\lambda}{2p}$, which is exactly halved in comparison with the case of binary mask owing to that the actual pitch of the alternating mask is 2p. This indicates that higher spatial frequencies could be resolved. If the spatial frequency of the grating mask is doubled, the first orders will be pushed onto the edge of the lens, the resolution limiting situation. Thus, the application of alternating phase shift masking can double the spatial resolution of the optical projection system. Also, it is noted that the zero order is zero and the first

orders are distributed symmetrically on the lens, the theoretical depth-of-focus becomes infinite, using the same argument applied in the previous analysis regarding off-axis illumination.

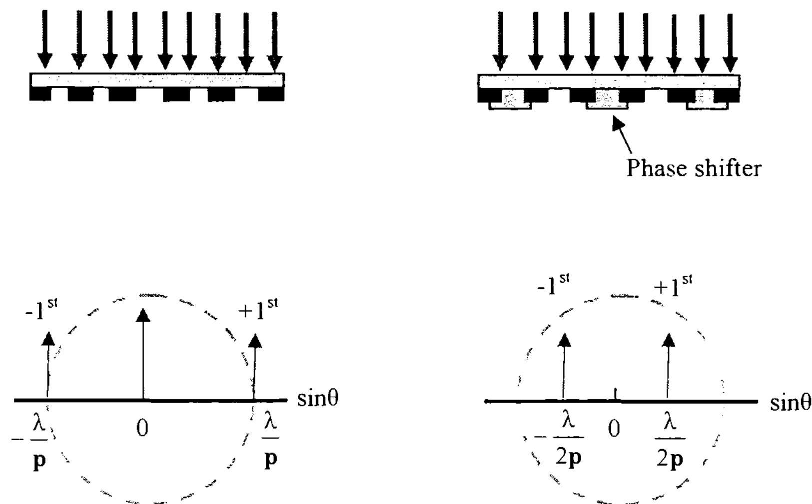

(a) Binary mask; (b) Alternating phase shifting mask,;

Figure 1.5 Schematic for the diffraction of a binary mask and the corresponding alternating phase shift mask.

Besides alternating phase shifting masks, other phase shifting mask schemes include chromeless phase shifting masks, attenuated phase shifting masks, etc. The chromeless phase shifting masks contain phase information only, as illustrated in Figure 1.6 (a). The phase is shifted 180° at the phase shifters. The destructive interference at the phase edges are used to print resist lines. Just as the reason argued for alternating phase shifting masks discussed in the previous paragraph, chromeless phase shifting masks can double the spatial resolution of the optical projection system. Multiple patterning steps are necessary to fabricate alternating phase shifting masks but only one patterning step is required is required for chromeless phase shifting masks.

For alternating phase shifting masks and chromeless phase shifting masks, unwanted resist features are likely to be printed at the edge of the phase shifters. Usually, additional processes are required to get ride of those extra resist features. However, this drawback is not associated with phase shift masking scheme called attenuated phase shifting mask, as depicted in Figure 1.6 (b). The opaque materials on the mask are replaced with partially transparent (6-40% range is common) materials with 180° phase shift. This technique does not boost the spatial resolution limit relative to binary masks but the image contrast can be enhanced due to the attenuation of the zero order, the background signal, from destructive interference. It is easy to understand that, together with off-axis illumination and with proper balance between zero order and the first orders, attenuated phase shift masking can enhance both spatial resolution limit and image contrast.

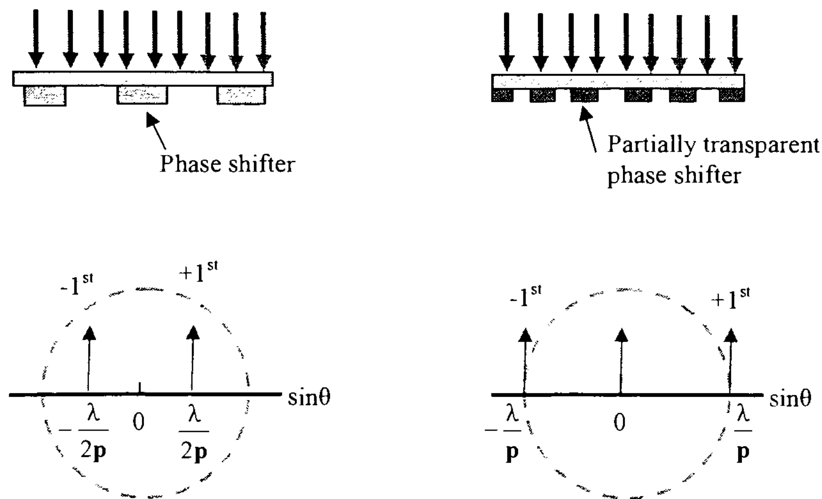

(a) Chromeless phase shifting mask; (b) Attenuated phase shifting mask;

Figure 1.6 Schematic for the diffraction of a chromeless phase shifting mask and an attenuated phase shift mask.

1.2.3 Optical Proximity Correction[39-41]

An optical projection imaging system is a low-pass filter of spatial frequencies. At the resolution limits, a minimal set of diffracted orders are passed by the low-pass filter. Optical lithography using a minimal set of diffracted orders is associated with loss of image fidelity due to the absence of high spatial frequency information. As a result, one printed resist shape is not only dependent on the mask pattern itself but also may be affected by other geometries proximate to it, the so called proximity effects. One example is that the printed resist line-width is a function of the pitch of the grating, in which the line sits. Other examples of proximity effects include corner rounding, line-end shortening, line-width narrowing, etc. One easy approach of correcting the proximity effects is to pre-bias the mask in a way so that the printed resist geometry is more like the desired shape. This technique is termed Optical Proximity Corrections (OPC). One simple example of OPC is shown in Figure 1.7. Without OPC, the L shape pattern on the mask is printed with rounded corners and shortened ends, shown in Figure 1.7 (a). By adding sub-resolution serifs to the L shape, the resulting resist pattern becomes more like an L shape, as shown in Figure 1.7 (b).

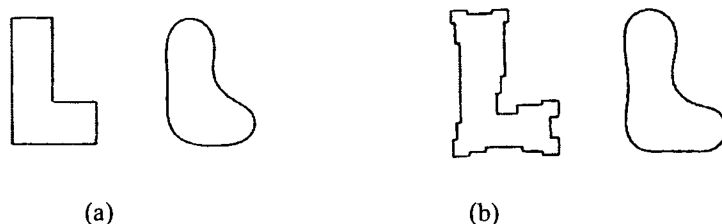

(a) (b)

Figure 1.7 Comparison of the resist images from mask pattern (a) without OPC and (b) with OPC.[39]

1.3 Motivation of This Dissertation

Together with resolution enhancement technologies reviewed in the previous section, 193-nm wavelength excimer laser lithography has been shown capable of printing 65 nm half pitch features. However, it is not theoretically possible with conventional 193- nm lithography to print half pitch of 45 nm features, a technology node proposed by Internal Technology Roadmap for Semiconductor (ITRS) (see Table 1.1). The theoretical limit is 48.3 nm, one quarter of the wavelength, for a maximum NA of 1.0. It is theoretically achievable with 157-nm excimer laser or shorter wavelength lithography. Nevertheless, the aforementioned difficulties associated with shorter wavelength have generated virtually insurmountable barriers to lithographic practice in the aspects of imaging and masking materials. In the past few years, the difficulties in tackling these barriers have turned attentions to another alternative: immersion imaging at the wavelength of 193-nm, driving the resolution further without switching to a shorter wavelength.[42-52]

Enhancement of optical resolution in immersion imaging with respect to conventional imaging is due to the enhancement of numerical apertures, as described by Rayleigh's criterion, $R = \frac{k_1\lambda}{n\sin\theta} = \frac{k_1\lambda}{NA}$, where n is the refractive index of the imaging media. The NA in a thin layer of photoresist could be as high as 1.5~1.8, the typical value of the refractive index of a photoresist. However, it is limited by the refractive index of the media between the photoresist layer and the final lens surface. Governed by Snell's law, the maximum NA is determined by the refractive index of the photoresist or the media, whichever is smaller. In conventional optical lithography, the maximum NA obviously is 1.0, the refractive index of air. The introduction of a layer of fluid between

the photoresist layer and the final lens surface would bring up the opportunities of imaging at NA higher than 1.0. It has been argued that the shrinkage of wavelength in the fluid relative to vacuum wavelength results in resolution improvement. Nevertheless, the wavelength in the photoresist remains the same, either in the case of conventional lithography or immersion lithography. The difference is that the oblique angle (θ) in the resist can be brought higher by immersion fluid. Considering we are interested in imaging in the photoresist layer, the justification by numerical aperture enhancement is more accurate than the wavelength shrinkage argument. In addition to resolution enhancement, immersion lithography also affords a larger paraxial depth of focus, $DOF = \pm k_2\lambda/(n\sin^2\theta) = \pm k_2 n\lambda/NA^2$, in comparison to imaging in air for the same NA. For the industry, the transition from 193-nm "dry" to 193-nm immersion would not require a dramatic change of the lithography system in view of the fact that techniques developed over previous generations regarding reticles, lenses, and even photoresists can be retained, minimizing introduction of technical risks. It is generally agreed that immersion imaging is viable to extend 193-nm lithography to the 45 nm node.

The refractive index of water, the candidate fluid for 193-nm immersion lithography, is 1.44.[53, 54] Endeavors are being put into seeking fluids with high refractive indices. At Rochester Institute of Technology, an aqueous solution of phosphoric acid is found to possess a refractive index of 1.54.[53] However, fluids with refractive indices rivaling those of solids will not be immediately available. For example, the indices of some solids are 1.56 for fused silica, 1.58 for BaF_2, 1.64 for LaF_3, 1.92 for Al_2O_3 sapphire, etc. at the wavelength of 193 nm.[55] Just like liquid immersion, solid immersion also increases numerical aperture when a piece of high refractive index solid is inserted

between the objective lens and the imaging plane. Concerning production reality, solid immersion technique is less practical than liquid immersion since the direct contact of lens surface with resist film would cause severe resist defects, lens damage, as well as lens contamination.

Although not appearing to be production friendly, solid immersion imaging techniques could provide opportunities to probe high NA imaging behaviors at values that are not currently available in fluid immersion imaging. For instance, sapphire (n=1.92 @193nm) immersion imaging could allow imaging with a 193-nm resist (typically, n=1.70 @193nm) at numerical numbers close to 1.7, which is the physical resolution limit of the resist materials with a refractive index near 1.70. The physical resolution limit of a photoresist at a given source wavelength is determined by the refractive index of the resist, *i.e.*, $R = \frac{\lambda}{4n}$, where R is the minimum resolvable dimension. It seems that 193nm or 157nm will be the ultimate wavelength for optical imaging. Therefore, the ultimate optical resolution limit depends on the refractive index of the resist. Researches are going on to increase the refractive index of resists. With the capability of imaging at physical resolution limit, solid immersion technique will greatly facilitate these researches.

In addition, solid immersion allows the study of polarization effects on imaging at high numerical apertures. Projection of an optical image can be viewed as the interference of light beams emitting from the exit pupil, and this interference is polarization dependent. Take two-beam interference as an example. The interference contrast of two beams polarized perpendicular to the plane of incidence (TE) does not depend on incident angle due to that the electrical vectors of the two interfering beams

are always parallel to each other at any incident angle. The interference contrast of two beams polarized in the plane of incidence (TM) depends on the incident angle since the orientation of the electrical vectors of the two interfering beams is a function of incident angle. At an incident angle of 45° (90o between two beams) in the case of TM, no interference will result because the electrical vectors of the two beams are perpendicular to each other. Solid immersion imaging could bring the incidence angle in the resist close to 90°, allowing the study of polarization effects on imaging at the limits of high numerical apertures.

Milster's group at University of Arizona has developed a direct-writing system with solid immersion technology.[56-59] In their system, a hemisphere lens is placed in proximity to the recording media, where the focused light spot is coupled into the recording media through the 50 nm or so air gap. The gap is controlled by observing the reflected-light distribution in the pupil of the objective lens using a CCD. The solid immersion technology being proposed here is a projection imaging system instead of direct-writing. The interference image is coupled into the resist through the air gap. Other work has also been carried out in a solid immersion lens at longer wavelength.[60]

In a brief summary, this dissertation is motivated to study the imaging behaviors of hyper-NA optics in the context of liquid immersion and solid immersion lithography. It is also devoted to exploring the resolution limits of this newly emerging lithographic technique. This work will shed on light on the ultimate resolution limits of optical lithography, a long-sought curiosity in lithography community. Optical lithography in 25 nm regime will be experimentally explored. This would be the ultimate resolution limits of optical lithography if no higher index imaging materials could be found.

1.4 Research Directions

The research conducted in the areas described has been organized in the remainder of this dissertation in chapter format starting with Chapter 2 and ending in Chapter 9. Chapter 2 describes vector interference theory and its application in hyper-NA lithography. This allows for the calculation of light intensity distribution within the resist film as a function of NA, polarization as well as the optical constants of the materials. The theory is the optical basis of hyper-NA interferometric lithography. Using this vector interference theory, Chapter 3 presents simulation examples of hyper-NA imaging, revealing polarization effects, BARC behaviors, resist properties, etc. Each example is intended to exhibit an important scenario. Chapter 4 is a description in detail of the experiment setup. An analysis of the experimental configuration is conducted in Chapter 5. The effects of beam direction stability, spatial coherence and temporal coherence on interferometric fringe are analyzed. Chapter 6 is an experimental results discussion chapter. The polarization effects at hyper-NA were experimental studied. SEM pictures are compared against simulation results. Chapter 7 is devoted to solid immersion lithography. With solid immersion, the NA value has been pushed higher than the index of the resist. Imaging at NA close to the refractive index of the resist and imaging at NA higher than the refractive index of the resist are experimental studied. The results have shown that the refractive index of a resist material is not a resolution limiting factor. Instead, higher NA imaging is possible using evanescent waves. Chapter 2 through Chapter 7 is focused on hyper-NA imaging, with interference lithography as a research

tool. One of the practical issues, air bubbles scattering effects in immersion lithography is studied in Chapter 8. Chapter 9 presents a whole summary of the Dissertation.

CHAPTER 2

VECTOR INTERFERENCE THEORY

2.1 Introduction

In a conventional lithographic imaging system, the patterns on the mask are projected through a set of lenses on a wafer coated with photoresist where the image of the patterns is recorded. With interference lithography, a series of periodic patterns are produced in a photoresist film by the interfering of two coherent laser beams. For a few special cases, diffraction-limited projection imaging is analogous to interference imaging. The first case is the projection imaging of a phase shifting grating mask (1:1 duty ration, alternating 180° phase, 100% transmission) with coherent illumination. The grating's zero diffraction order vanishes. If the pitch of the grating is such that only the first diffraction orders are captured in the entrance pupil, the resulting image is simply the interference fringes of two plane waves with oblique angle θ (half of the angle subtended by the lens at the image plane). The second case is the projection imaging of a 1:1 binary grating mask with coherent illumination. If the pitch of the grating is such that only the zero and first diffraction orders are captured in the entrance pupil, the resulting image is the interference fringes of three plane waves, two beams with oblique angle θ, one normal to the image plane. The third case is the projection imaging of a 1:1 binary grating mask with off-axis coherent illumination. If the pitch of the grating is such that

only the zero and one of the first diffraction orders are captured in the entrance pupil, the resulting image is the interference fringes of two plane waves of different amplitudes with oblique angle θ(since the amplitude of the zero order is different from that of the first orders). For the above cases with partial coherence illumination, the resulting images still can be considered as interference fringes but with weaker first diffraction orders since only part of the first orders is captured in the entrance pupil. Simply put, imaging of the above grating objects in an optical projection system can be reduced to the problems of plane wave interference.

The resemblance of projection imaging to interference imaging in the cases analyzed in the preceding paragraph has stimulated studies of optical projection systems using an interferometric setup. Although those are special cases, they represent a system's resolution limits, which mostly define the system's capability. An advantage of using an interferometric setup is that the costly lenses are not needed. At the same time, a single interferometric setup possesses the flexibility of emulating various lenses. The polarization of beams can be conveniently manipulated, allowing study of polarization effects. An extra flexibility is that the relative amplitude of the beams can be easily controlled. In view of these advantages, a rigorous analysis of plane wave interference is performed in the following sections to afford a better understanding.

2.2 Interference Imaging

Interference fringes will be formed in the intersection region of two or more sets of coherent monochromatic optical plane waves. Interference due to two or three polarized coherent monochromatic optical plane waves is analyzed here. The "beams" in the following discussion generally refer to monochromatic optical plane waves.

2.2.1 Two-beam interference with TE polarization

As illustrated in the Figure 2.1, two beams with equal oblique angle θ intersect at a plane. The electrical vectors of the plane waves are perpendicular to the plane of the figure (TE polarization). The intersection line is set as x axis with origin at the center of the beams. y axis is the normal direction. With the time dependence factor suppressed and the origin as phase reference point, the fields E_1 (left beam) and E_2 (right beam) at the intersection as a function of location x can be expressed respectively as

$$\mathbf{E}_1 = |\mathbf{E}_1| e^{-i(kx \sin\theta)} \qquad [2\text{-}1]$$

$$\mathbf{E}_2 = |\mathbf{E}_2| e^{-i(-kx \sin\theta)} \qquad [2\text{-}2]$$

where k is the propagation vector, $\frac{2n\pi}{\lambda}$ with n being the refractive index of the imaging media. The total field E at the intersection is the sum of the two:

$$\begin{aligned} \mathbf{E} = \mathbf{E}_1 + \mathbf{E}_2 &= |\mathbf{E}_1| e^{-i(kx \sin\theta)} + |\mathbf{E}_2| e^{-i(-kx \sin\theta)} \\ &= (|\mathbf{E}_1| + |\mathbf{E}_2|)\cos(kx \sin\theta) + i(|\mathbf{E}_1| - |\mathbf{E}_2|)\sin(kx \sin\theta). \end{aligned} \qquad [2\text{-}3]$$

The corresponding intensity is proportional to the square of the amplitude of the field,

$$\begin{aligned} I \propto |\mathbf{E}|^2 &= |\mathbf{E}_1 + \mathbf{E}_2|^2 \\ &= [(|\mathbf{E}_1| + |\mathbf{E}_2|)\cos(kx \sin\theta)]^2 + [(|\mathbf{E}_1| - |\mathbf{E}_2|)\sin(kx \sin\theta)]^2 \\ &= |\mathbf{E}_1|^2 + |\mathbf{E}_2|^2 + 2|\mathbf{E}_1||\mathbf{E}_2|\cos(2kx \sin\theta). \end{aligned} \qquad [2\text{-}4]$$

The distribution of intensity along x direction is sinusoidal, the pitch (spatial period) of which is

$$p = \frac{2\pi}{2k\sin\theta} = \frac{\lambda}{2n\sin\theta} . \quad [2\text{-}5]$$

For the phase shifting grating case discussed in the previous section, $|\mathbf{E}_1| = |\mathbf{E}_2|$, the intensity distribution is reduced to

$$I \propto 2|\mathbf{E}_1|^2[1 + \cos(2kx\sin\theta)] = 4|\mathbf{E}_1|^2 \cos^2(kx\sin\theta) . \quad [2\text{-}6]$$

For the case of binary grating with off axis illumination discussed in the previous section, $|\mathbf{E}_2| = \frac{1}{2\pi}|\mathbf{E}_1|$, the intensity distribution is reduced to

$$I \propto |\mathbf{E}_1|^2[1 + \frac{1}{4\pi^2} + \frac{1}{\pi}\cos(2kx\sin\theta)] . \quad [2\text{-}7]$$

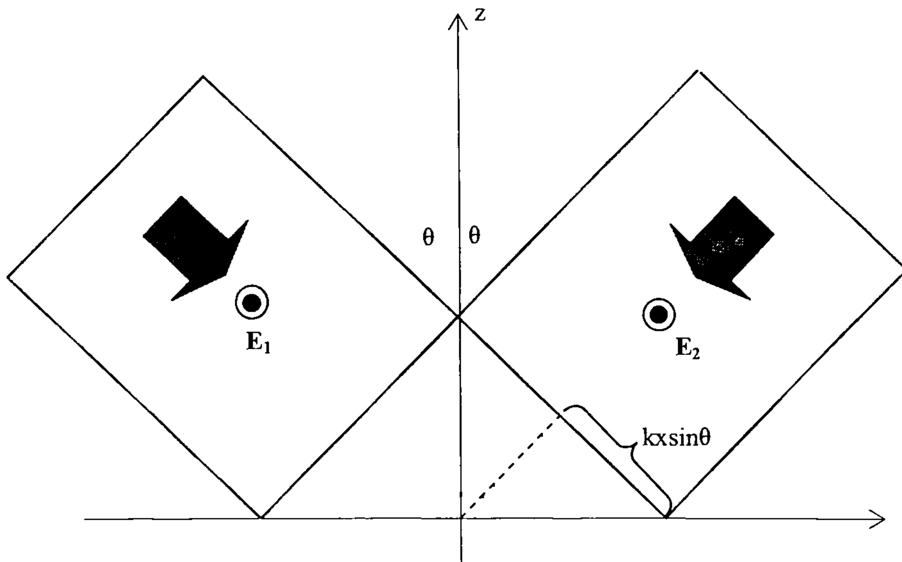

Figure 2.1 Interference of two monochromic plane waves with TE with equal oblique angle θ. The intersection line is set as x axis with origin at the center of the beams. z axis is the normal direction.

2.2.2. Two-beam interference with TM polarization

TM polarization refers to the polarization state where the electrical vectors of the plane waves are parallel to the plane of the figure, as illustrated in the Figure 2.2. For TE polarization, the total field is simply the scalar summation of the two plane waves since their electrical vectors are parallel to each other. For TM polarization, the electrical vector is a function of oblique angle θ, requiring vector operation for summation. E_1 and E_2 can be expressed respectively as

$$\begin{aligned}\mathbf{E}_1 &= \mathbf{E}_{1x}\hat{\mathbf{i}} + \mathbf{E}_{1z}\hat{\mathbf{j}} \\ &= |\mathbf{E}_1|\mathbf{e}^{-i(kx\sin\theta)}(\hat{\mathbf{i}}\cos\theta + \hat{\mathbf{j}}\sin\theta)\end{aligned} \quad [2\text{-}8]$$

$$\begin{aligned}\mathbf{E}_2 &= \mathbf{E}_{2x}\hat{\mathbf{i}} + \mathbf{E}_{2z}\hat{\mathbf{j}} \\ &= |\mathbf{E}_2|\mathbf{e}^{-i(-kx\sin\theta)}(\hat{\mathbf{i}}\cos\theta - \hat{\mathbf{j}}\sin\theta)\end{aligned} \quad [2\text{-}9]$$

where $\hat{\mathbf{i}}$ and $\hat{\mathbf{j}}$ are unit vectors in x and z direction respectively, subscripts x, z designate x, z components of the electrical vectors. The total field E thus is

$$\begin{aligned}\mathbf{E} &= \mathbf{E}_1 + \mathbf{E}_2 \\ &= (\mathbf{E}_{1x} + \mathbf{E}_{2x})\hat{\mathbf{i}} + (\mathbf{E}_{1z} + \mathbf{E}_{2z})\hat{\mathbf{j}} \\ &= (|\mathbf{E}_1|\mathbf{e}^{-i(kx\sin\theta)} + |\mathbf{E}_2|\mathbf{e}^{-i(-kx\sin\theta)})(\cos\theta)\hat{\mathbf{i}} + (|\mathbf{E}_1|\mathbf{e}^{-i(kx\sin\theta)} - |\mathbf{E}_2|\mathbf{e}^{-i(-kx\sin\theta)})(\sin\theta)\hat{\mathbf{j}} \\ \mathbf{E} &= [(|\mathbf{E}_1| + |\mathbf{E}_2|)\cos(kx\sin\theta) + i(|\mathbf{E}_1| - |\mathbf{E}_2|)\sin(kx\sin\theta)](\cos\theta)\hat{\mathbf{i}} \\ &\quad + [(|\mathbf{E}_1| - |\mathbf{E}_2|)\cos(kx\sin\theta) + i(|\mathbf{E}_1| + |\mathbf{E}_2|)\sin(kx\sin\theta)](\sin\theta)\hat{\mathbf{j}}.\end{aligned} \quad [2\text{-}10]$$

The intensity distribution is evaluated as

$$\begin{aligned}I &\propto |\mathbf{E}|^2 = |\mathbf{E}_1 + \mathbf{E}_2|^2 \\ &= |(E_{1x} + E_{2x})|^2 + |(E_{1z} + E_{2z})|^2 \\ &= [|\mathbf{E}_1|^2 + |\mathbf{E}_2|^2 + 2|\mathbf{E}_1||\mathbf{E}_2|\cos(2kx\sin\theta)]\cos^2\theta + [|\mathbf{E}_1|^2 + |\mathbf{E}_2|^2 - 2|\mathbf{E}_1||\mathbf{E}_2|\cos(2kx\sin\theta)]\sin^2\theta \\ &= |\mathbf{E}_1|^2 + |\mathbf{E}_2|^2 + 2|\mathbf{E}_1||\mathbf{E}_2|\cos(2kx\sin\theta)(\cos^2\theta - \sin^2\theta) \\ I &\propto |\mathbf{E}_1|^2 + |\mathbf{E}_2|^2 + 2|\mathbf{E}_1||\mathbf{E}_2|\cos(2kx\sin\theta)\cos(2\theta).\end{aligned} \quad [2\text{-}11]$$

For the phase shifting grating case discussed in the previous section, $|\mathbf{E}_1| = |\mathbf{E}_2|$, the intensity distribution is reduced to

$$I \propto 2|\mathbf{E}_1|^2[1 + \cos(2kx\sin\theta)\cos(2\theta)]. \qquad [2\text{-}12]$$

For the case of binary grating with off axis illumination discussed in the previous section, $|\mathbf{E}_2| = \frac{1}{2\pi}|\mathbf{E}_1|$, the intensity distribution is reduced to

$$I \propto |\mathbf{E}_1|^2[1 + \frac{1}{4\pi^2} + \frac{1}{\pi}\cos(2kx\sin\theta)\cos(2\theta)]. \qquad [2\text{-}13]$$

The pitch of the intensity distribution remains as $p = \frac{\lambda}{2n\sin\theta}$

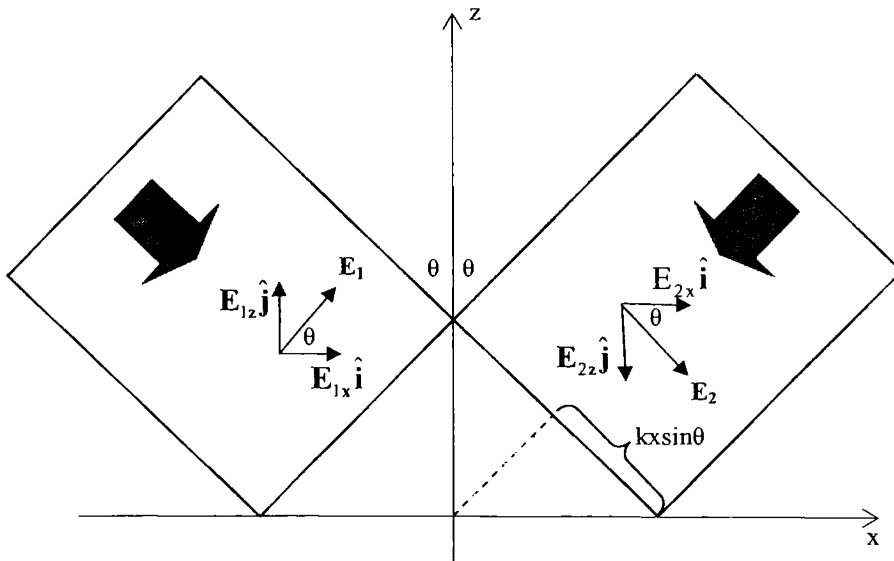

Figure 2.2 Interference of two monochromic plane waves with TM with equal oblique angle *θ*. The intersection line is set as *x* axis with origin at the center of the beams. *z* axis is the normal direction.

2.2.3 Three-beam interference with TE polarization

If there is a third beam E_0 that is normal to the intersection of the two beams as discussed in the preceding sections, their interference can be analyzed in a similar way.

Note that the beam E_0 has a constant phase across the intersection. For TE polarization, the total field can be expressed as

$$\begin{aligned}\mathbf{E} &= \mathbf{E}_0 + \mathbf{E}_1 + \mathbf{E}_2 \\ &= |\mathbf{E}_0| + |\mathbf{E}_1| e^{-i(kx\sin\theta)} + |\mathbf{E}_2| e^{-i(-kx\sin\theta)} \\ &= |\mathbf{E}_0| + (|\mathbf{E}_1| + |\mathbf{E}_2|)\cos(kx\sin\theta) + i(|\mathbf{E}_1| - |\mathbf{E}_2|)\sin(kx\sin\theta).\end{aligned}$$

The intensity distribution therefore is

$$\begin{aligned}I \propto |\mathbf{E}|^2 &= |\mathbf{E}_0 + \mathbf{E}_1 + \mathbf{E}_2|^2 \\ &= |\mathbf{E}_0|^2 + |\mathbf{E}_1|^2 + |\mathbf{E}_2|^2 + 2|\mathbf{E}_1||\mathbf{E}_2|\cos(2kx\sin\theta) + 2|\mathbf{E}_0|(|\mathbf{E}_1| + |\mathbf{E}_2|)\cos(kx\sin\theta).\end{aligned}$$

$$\text{if } |\mathbf{E}_1| = |\mathbf{E}_2| = \frac{1}{2\pi}|\mathbf{E}_0|$$

$$I = (1 + \frac{1}{2\pi^2})|\mathbf{E}_0|^2 + \frac{1}{2\pi^2}|\mathbf{E}_0|^2\cos(2kx\sin\theta) + \frac{2}{\pi}|\mathbf{E}_0|^2\cos(kx\sin\theta). \qquad [2\text{-}14]$$

Note that the intensity distribution has two frequencies, $\frac{\lambda}{2n\sin\theta}$ and $\frac{\lambda}{n\sin\theta}$, the latter of which dominates the modulation.

2.2.4 Three-beam interference with TM polarization

Regarding to three-beam interference with TM polarization, the total field can be derived similarly

$$\begin{aligned}\mathbf{E} &= \mathbf{E}_0 + \mathbf{E}_1 + \mathbf{E}_2 \\ &= (E_{0x} + E_{1x} + E_{2x})\hat{\mathbf{i}} + (E_{0z} + E_{1z} + E_{2z})\hat{\mathbf{j}} \\ &= (E_0 + E_{1x} + E_{2x})\hat{\mathbf{i}} + (E_{1z} + E_{2z})\hat{\mathbf{j}} \\ &= [|\mathbf{E}_0| + (|\mathbf{E}_1| e^{-i(kx\sin\theta)} + |\mathbf{E}_2| e^{-i(-kx\sin\theta)})(\cos\theta)]\hat{\mathbf{i}} + (|\mathbf{E}_1| e^{-i(kx\sin\theta)} - |\mathbf{E}_2| e^{-i(-kx\sin\theta)})(\sin\theta)\hat{\mathbf{j}} \\ &= [|\mathbf{E}_0| + (|\mathbf{E}_1| + |\mathbf{E}_2|)\cos(kx\sin\theta)\cos\theta + i(|\mathbf{E}_1| - |\mathbf{E}_2|)\sin(kx\sin\theta)\cos\theta]\hat{\mathbf{i}} \\ &\quad + [(|\mathbf{E}_1| - |\mathbf{E}_2|)\cos(kx\sin\theta) + i(|\mathbf{E}_1| + |\mathbf{E}_2|)\sin(kx\sin\theta)](\sin\theta)\hat{\mathbf{j}}.\end{aligned}$$

The intensity distribution is

$$
\begin{aligned}
I &\propto |\mathbf{E}|^2 = |\mathbf{E}_0 + \mathbf{E}_1 + \mathbf{E}_2|^2 \\
&= |(E_0 + E_{1x} + E_{2x})|^2 + |(E_{1z} + E_{2z})|^2 \\
&= |\mathbf{E}_0|^2 + [|\mathbf{E}_1|^2 + |\mathbf{E}_2|^2 + 2|\mathbf{E}_1||\mathbf{E}_2|\cos(2kx\sin\theta)]\cos^2\theta + 2|\mathbf{E}_0|[(|\mathbf{E}_1| + |\mathbf{E}_2|)\cos(kx\sin\theta)\cos\theta] \\
&\quad + [|\mathbf{E}_1|^2 + |\mathbf{E}_2|^2 - 2|\mathbf{E}_1||\mathbf{E}_2|\cos(2kx\sin\theta)]\sin^2\theta \\
&= |\mathbf{E}_0|^2 + |\mathbf{E}_1|^2 + |\mathbf{E}_2|^2 + 2|\mathbf{E}_1||\mathbf{E}_2|\cos(2kx\sin\theta)(\cos^2\theta - \sin^2\theta) + 2|\mathbf{E}_0|[(|\mathbf{E}_1| + |\mathbf{E}_2|)\cos(kx\sin\theta)\cos\theta] \\
&= |\mathbf{E}_0|^2 + |\mathbf{E}_1|^2 + |\mathbf{E}_2|^2 + 2|\mathbf{E}_1||\mathbf{E}_2|\cos(2kx\sin\theta)\cos(2\theta) + 2|\mathbf{E}_0|[(|\mathbf{E}_1| + |\mathbf{E}_2|)\cos(kx\sin\theta)\cos\theta].
\end{aligned}
$$

if $|\mathbf{E}_1| = |\mathbf{E}_2| = \frac{1}{2\pi}|\mathbf{E}_0|$

$$
I \propto (1 + \frac{1}{2\pi^2})|\mathbf{E}_0|^2 + \frac{1}{2\pi^2}|\mathbf{E}_0|^2\cos(2kx\sin\theta)\cos(2\theta) + \frac{2}{\pi}|\mathbf{E}_0|^2\cos(kx\sin\theta)\cos(\theta). \quad [2\text{-}15]
$$

Note that the intensity distribution has two frequencies, $\frac{\lambda}{2n\sin\theta}$ and $\frac{\lambda}{n\sin\theta}$, the latter of which dominates the modulation.

2.3 Light Propagation in a Stack of Thin Films

2.3.1 Tranmission and reflection coefficients of a thin-film assembly

Transmission and reflection coefficients of a thin-film assembly can be computed using the well established thin-film matrix techniques based on Macleod's work.[61] The optical characteristic of a layer of thin film is expressed using a matrix

$$
M_j = \begin{bmatrix} \cos\delta_j & i\sin\delta_j/\eta_j \\ i\eta_j\sin\delta_j & \cos\delta_j \end{bmatrix} \quad [2\text{-}16]
$$

where δ_j is phase factor and η_j is the oblique optical admittance, which are defined respectively as

$$
\eta_j = N_j\cos\theta_j \text{ for TE polarization;} \quad [2\text{-}17]
$$

$$\eta_j = \frac{N_j}{\cos\theta_j} \quad \text{for TM polarization;} \qquad [2\text{-}18]$$

$$\delta_j = \frac{2\pi d_j N_j \cos\theta_j}{\lambda}. \qquad [2\text{-}19]$$

The characteristic matrix of an assembly with q layers is simply the product of the individual matrices

$$\begin{bmatrix} B \\ C \end{bmatrix} = \left(\prod_{j=1}^{j=q} M_j \right) \begin{bmatrix} 1 \\ \eta_{sub} \end{bmatrix} \qquad [2\text{-}20]$$

where subscript *sub* denotes the substrate.

The transmission and reflection coefficients of the thin film assembly are respectively expressed as

$$\tau = \frac{2\eta_0}{B\eta + C} \qquad r = \frac{B\eta_0 - C}{B\eta_0 + C} \qquad [2\text{-}21]$$

where η_0 the oblique optical admittance in the incident media.

2.3.2 Intensity distribution within a thin film layer

A uniform medium is assumed in the preceding analysis on interference imaging. However, photoresist, the image recording media, is often in the form of a layer of thin film among an assembly of thin films. A typical film stack in modern lithography may include a top coat layer, a resist layer and a BARC (bottom antireflective coating) layer on a substrate. The top layer protects the resist layer by isolating it from the immersion fluid in the context of immersion lithography. The BARC layer functions to alleviate standing waves due to reflection from the substrate. Reflection from the substrate is reduced by destructive interference of the light reflected from the top interface of the

BARC and the light reflected from the substrate. The BARC thickness is chosen such that the phase difference is π. The optical constants (n, k) of the BARC are tuned to result in equal amplitude destructive interference, minimizing reflection from substrate. The film stack forms an inhomogeneous medium. Reflections/refractions at the interfaces result in redistribution of light intensity within the photoresist layer. Other workers have analyzed the light intensity distribution within the resist film which is on the top of the film stack.[62-64] When a top coat layer is present above the resist film, a similar analysis can be conducted to derive the light intensity distribution within the resist film.

A ray incident on the film stack is illustrated in Figure 2.3. The total field at any point within the resist layer is the sum of the downward field and upward field. The downward field and upward field at interface *X* are denoted as E_{iX} and E_{rX}, respectively, where *X* indicates the specific media interface. The downward and upward fields at interface III are E_{iIII} and E_{rIII}, respectively. The downward field and upward field at any point within the resist layer can be expressed as

$$\begin{aligned} \mathbf{E}_{\downarrow} &= \mathbf{E}_{iIII} e^{+i\frac{2\pi N_2}{\lambda}(d_2-z)\cos\theta_2} \\ \mathbf{E}_{\uparrow} &= \mathbf{E}_{rIII} e^{-i\frac{2\pi N_2}{\lambda}(d_2-z)\cos\theta_2} \end{aligned} \qquad [2\text{-}22]$$

where z is the distance from interface II, the phase is referenced at interface III. The total field in the resist layer at any point z is therefore,

$$\begin{aligned} \mathbf{E}(z) &= \mathbf{E}_{\downarrow} + \mathbf{E}_{\uparrow} \\ &= \mathbf{E}_{iIII} e^{+i\frac{2\pi N_2}{\lambda}(d_2-z)\cos\theta_2} + \mathbf{E}_{rIII} e^{-i\frac{2\pi N_2}{\lambda}(d_2-z)\cos\theta_2}. \end{aligned} \qquad [2\text{-}23]$$

It can be shown that E_{iIII} and E_{rIII} are related to the incident field E_{iI} at interface I. The transmission and reflection coefficients at the interface I are defined as:

$$\tau_I = \frac{\mathbf{E}_{sub}}{\mathbf{E}_{iI}} \qquad r_I = \frac{\mathbf{E}_{rI}}{\mathbf{E}_{iI}} \qquad [2\text{-}24]$$

where E_{sub} is the field transmitted at the last interface. Similarly, the transmission and reflection coefficients at interface II, III are defined as

$$\tau_{II} = \frac{\mathbf{E}_{sub}}{\mathbf{E}_{iII}} \qquad r_{II} = \frac{\mathbf{E}_{rII}}{\mathbf{E}_{iII}} \qquad [2\text{-}25]$$

$$\tau_{III} = \frac{\mathbf{E}_{sub}}{\mathbf{E}_{iIII}} \qquad r_{III} = \frac{\mathbf{E}_{rIII}}{\mathbf{E}_{iIII}}. \qquad [2\text{-}26]$$

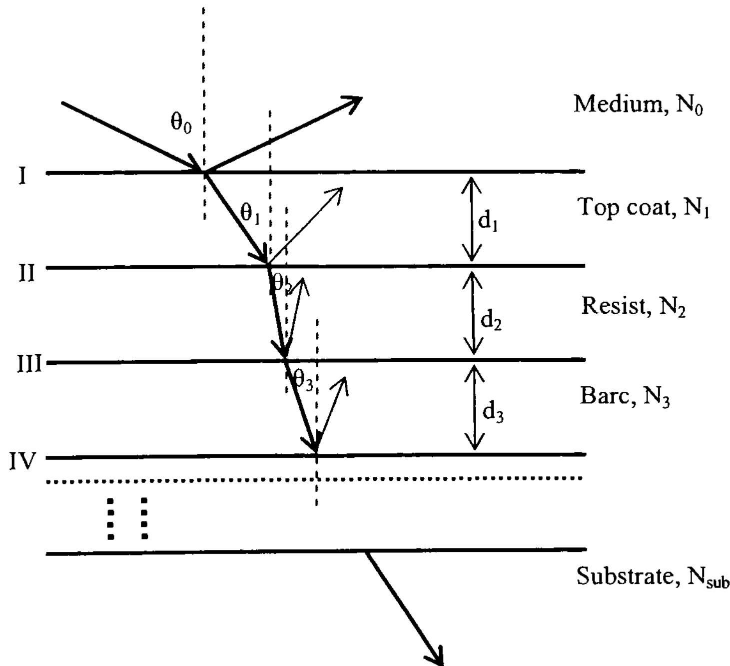

Figure 2.3 Thin film stack on a substrate with incident plane wave. The film thicknesses, optical constants, interfaces, incident angles are denoted. The optical constants may be complex.

From the above equations, the following relations can be derived

$$\mathbf{E}_{iIII} = \frac{\tau_I}{\tau_{III}}\,\mathbf{E}_{iI} \qquad \mathbf{E}_{rIII} = r_{III}\frac{\tau_I}{\tau_{III}}\,\mathbf{E}_{iI}\,. \qquad [2\text{-}27]$$

The total field E(z) at any point within the resist layer is derived by substituting the above equations into Equation [2-23]

$$\mathbf{E}(z) = \frac{\tau_I}{\tau_{III}}\left(e^{+i\frac{2\pi N_2}{\lambda}(d_2 - z)\cos\theta_2} + r_{III}e^{-i\frac{2\pi N_2}{\lambda}(d_2 - z)\cos\theta_2}\right)\mathbf{E}_{iI} \qquad [2\text{-}28]$$

Further substitute of

$$F = \frac{\tau_I}{\tau_{III}}\left(e^{+i\frac{2\pi N_2}{\lambda}(d_2 - z)\cos\theta_2} + r_{III}e^{-i\frac{2\pi N_2}{\lambda}(d_2 - z)\cos\theta_2}\right) \qquad [2\text{-}29]$$

results in

$$\mathbf{E}(z) = F\mathbf{E}_{iI} \qquad [2\text{-}30]$$

where F is termed as the Film Function. It describes the standing-wave behavior due to the reflection from below the resist layer. Evaluation of F requires computing τ_I, τ_{III}, r_{III}, which can be done using the Equation [2-21].

2.3.3 The Film Function (F)

As discussed in the preceding section, the Film Function (F) describes the standing-wave effects within the resist layer due to reflection from the lower interface of the resist layer. From Equation [2-29], F can be evaluated using coefficients τ_I, τ_{III} and r_{III}, which are polarization dependent. For TE polarization, the film function F is simply expressed as,

$$F_S = \left[\frac{\tau_I}{\tau_{III}}\right]_S \left(e^{i\frac{2\pi N_2}{\lambda}(d_2-z)\cos\theta_2} + [r_{III}]_S e^{-i\frac{2\pi N_2}{\lambda}(d_2-z)\cos\theta_2} \right) \qquad [2\text{-}31]$$

where the subscript S denotes S or transverse electric (TE) polarization. In the case of P or transverse magnetic (TM) polarization, the corresponding coefficients computed using standard thin film matrix techniques can not applied to equation [2-30] directly in that a vector summation of the downward and upward fields is needed since their polarization directions are not parallel to each other. Decomposition of the incident electrical vector into x and z components which are then treated separately is necessary. The corresponding F functions are expressed as

$$F_{xP} = \left[\frac{\tau_I}{\tau_{III}}\right]_{xP} \left(e^{+i\frac{2\pi N_2}{\lambda}(d_2-z)\cos\theta_2} + [r_{III}]_{xP} e^{-i\frac{2\pi N_2}{\lambda}(d_2-z)\cos\theta_2} \right) \qquad [2\text{-}32]$$

$$F_{zP} = \left[\frac{\tau_I}{\tau_{III}}\right]_{zP} \left(e^{+i\frac{2\pi N_2}{\lambda}(d_2-z)\cos\theta_2} + [r_{III}]_{zP} e^{-i\frac{2\pi N_2}{\lambda}(d_2-z)\cos\theta_2} \right) \qquad [2\text{-}33]$$

where subscripts x and z denote the related decomposition components. The coefficients τ_I, τ_{III} and r_{III} of x components can be computed using standard thin film matrix techniques but not the z components. However, the relationship between the coefficients of x and z components can be established using Figure 2.4.

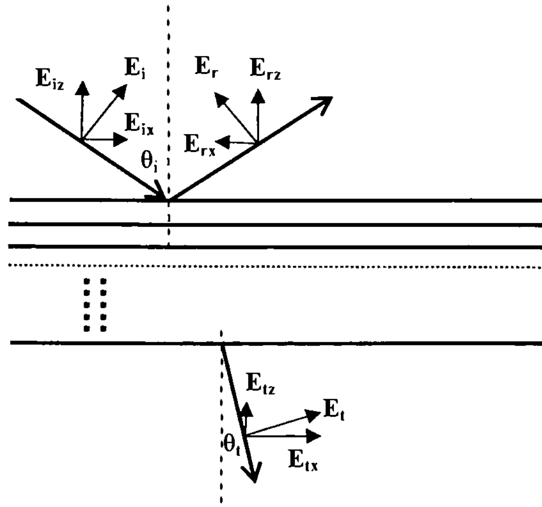

Figure 2.4 Relationship between x and z components for reflection and transmission coefficients of a TM polarized wave incident on a stack of thin films. Incident angle is θ_i and refractive angle is θ_t. The electrical vectors are decomposed into x and z components.

As illustrated in Figure 2.4, a TM polarized incident wave incident on a stack of thin films with angle θ_i diffracts into a substrate with an angle θ_t. The electrical vectors of incident (denoted with subscript i) and diffracted waves (denoted with subscript t) are decomposed into x component (denoted with subscript x) and z component (denoted with subscript z). The reflection coefficient of x component is expressed as

$$r_{xP} = \frac{E_{rx}}{E_{ix}} . \qquad [2\text{-}34]$$

The z component is related to the x component by a simple tangent function. Also, it is noted that the E_{rz} is 180° out of phase with E_{rx}. Therefore,

$$r_{zP} = \frac{E_{rz}}{E_{iz}} = -\frac{\tan\theta_r E_{rx}}{\tan\theta_i E_{ix}} = -\frac{E_{rx}}{E_{iz}} = -r_{xP}$$

$$r_{zP} = -r_{xP} . \qquad [2\text{-}35]$$

Similarly, the transmission coefficient of x component is expressed as

$$\tau_{xP} = \frac{E_{tx}}{E_{ix}} . \qquad [2\text{-}36]$$

And the z component is related to the x component by a simple tangent function. Along with Snell's law, we have,

$$\tau_{zP} = \frac{E_{tz}}{E_{iz}} = \frac{\tan\theta_t E_{tx}}{\tan\theta_i E_{ix}} = \frac{\sin\theta_t \cos\theta_i E_{tx}}{\sin\theta_i \cos\theta_t E_{iz}} = \frac{N_i \cos\theta_i E_{tx}}{N_t \cos\theta_t E_{iz}}$$

$$\tau_{zP} = \frac{N_i \cos\theta_i}{N_t \cos\theta_t} \tau_{xP} . \qquad [2\text{-}37]$$

Application of the relationships from Equation [2-35] and [2-37] to Equation [2-33] yields the film function F for z component of TM polarization

$$F_{zP} = \frac{N_0 \cos\theta_0}{N_2 \cos\theta_2} \left[\frac{\tau_I}{\tau_{III}}\right]_{xP} \left(e^{i\frac{2\pi N_2}{\lambda}(d_2 - z)\cos\theta_2} - [r_{III}]_{xP} e^{-i\frac{2\pi N_2}{\lambda}(d_2 - z)\cos\theta_2} \right) \qquad [2\text{-}38]$$

where θ_0 is the incident angle in the media above the film assembly.

Equation [2-31], [2-32] and [2-38] constitute the whole Film Function (F). They are summarized here as

$$F_S = \left[\frac{\tau_I}{\tau_{III}}\right]_S \left(e^{i\frac{2\pi N_2}{\lambda}(d_2 - z)\cos\theta_2} + [r_{III}]_S e^{-i\frac{2\pi N_2}{\lambda}(d_2 - z)\cos\theta_2} \right) \qquad [2\text{-}31]$$

$$F_{xP} = \left[\frac{\tau_I}{\tau_{III}}\right]_{xP} \left(e^{i\frac{2\pi N_2}{\lambda}(d_2 - z)\cos\theta_2} + [r_{III}]_{xP} e^{-i\frac{2\pi N_2}{\lambda}(d_2 - z)\cos\theta_2} \right) \qquad [2\text{-}32]$$

$$F_{zP} = \frac{N_0 \cos\theta_0}{N_2 \cos\theta_2} \left[\frac{\tau_I}{\tau_{III}}\right]_{xP} \left(e^{i\frac{2\pi N_2}{\lambda}(d_2 - z)\cos\theta_2} - [r_{III}]_{xP} e^{-i\frac{2\pi N_2}{\lambda}(d_2 - z)\cos\theta_2} \right) . \qquad [2\text{-}38]$$

The light intensity distribution within the resist film resulting from interference is found simply by applying the Film Function defined in the preceding paragraph. For example, applying film function F to Equation [2-6] and Equation [2-12], the intensity distributions within the resist film resulting from two-beam interference for TE and TM polarization are found respectively as

$$I_{TE} \propto 2|F_S|^2|\mathbf{E}_1|^2[1+\cos(2kx\sin\theta_0)] = 2|F_{TE}|^2|\mathbf{E}_1|^2\cos^2(kx\sin\theta_0) \ . \qquad [2\text{-}39]$$

$$\begin{aligned} I_{TM} &\propto |\mathbf{E}|^2 = |\mathbf{E}_1+\mathbf{E}_2|^2 \\ &= |(E_{1x}+E_{2x})|^2 + |(E_{1z}+E_{2z})|^2 \\ &= [|\mathbf{E}_1|^2+|\mathbf{E}_2|^2+2|\mathbf{E}_1||\mathbf{E}_2|\cos(2kx\sin\theta_0)]\cos^2\theta_0 + [|\mathbf{E}_1|^2+|\mathbf{E}_2|^2-2|\mathbf{E}_1||\mathbf{E}_2|\cos(2kx\sin\theta_0)]\sin^2\theta_0 \\ &= 2|F_{xP}|^2|\mathbf{E}_1|^2\cos^2\theta_0[1+\cos(2kx\sin\theta_0)] + 2|F_{zP}|^2|\mathbf{E}_1|^2\sin^2\theta_0[1-\cos(2kx\sin\theta_0)] \\ &= 4|F_{xP}|^2|\mathbf{E}_1|^2\cos^2\theta_0\cos^2(kx\sin\theta_0) + 4|F_{zP}|^2|\mathbf{E}_1|^2\sin^2\theta_0\sin^2(kx\sin\theta_0). \end{aligned}$$

[2-40]

$|F|^2$ describes the standing wave effect in the vertical direction, which is not desirable in lithographic practice. It is convenient to express r_{III} in the form of

$$r_{III} = |r_{III}|e^{i\varphi} \qquad [2\text{-}41]$$

where φ is a real number. Then film function Equation [2-29] becomes

$$F = \frac{\tau_1}{\tau_{III}}\left(e^{i\frac{2\pi N_2}{\lambda}(d_2-z)\cos\theta_2} + |r_{III}|e^{-i\left[\frac{2\pi N_2}{\lambda}(d_2-z)\cos\theta_2-\varphi\right]}\right)$$

Evaluation of $|F|^2$ gives

$$
\begin{aligned}
|F|^2 &= \left|\frac{\tau_I}{\tau_{III}}\right|^2 \left|\left(e^{i\frac{2\pi N_2}{\lambda}(d_2-z)\cos\theta_2} + |r_{III}| e^{-i\left[\frac{2\pi N_2}{\lambda}(d_2-z)\cos\theta_2-\varphi\right]}\right)\right|^2 \\
&= \left|\frac{\tau_I}{\tau_{III}}\right|^2 \left|\left(1 + |r_{III}| e^{-i\left[\frac{4\pi N_2}{\lambda}(d_2-z)\cos\theta_2-\varphi\right]}\right)\right|^2 \\
&= \left|\frac{\tau_I}{\tau_{III}}\right|^2 \left\{1 + |r_{III}|^2 + 2|r_{III}|\cos\left[\frac{4\pi N_2}{\lambda}(d_2-z)\cos\theta_2 - \varphi\right]\right\}.
\end{aligned}
\qquad [2\text{-}42]
$$

It indicates that the sinusoidal standing wave has a pitch of $\frac{\lambda}{2\,\mathrm{Re}(N_2)\cos\theta_2}$. The amplitude of the standing wave is determined by $|r_{III}|$. Complete suppression of the standing wave requires that r_{III} vanishes.

2.4 Summary

The full-vector interference theory was described in this Chapter. The theory is valid at extremely high NA values, such as those projected for use with immersion lithography. For TE polarization, the total field distribution is obtained by the scalar summation of the incident plane waves since the electrical vectors are parallel to each other no matter what the incident angle is. For TM polarization, the electrical vectors is decomposed into x and z components before the summation of the incident waves. The field distribution within the resist is derived using the standard thin film calculation techniques

CHAPTER 3

ANALYSIS OF HYPER-NA INTERFEROMETRIC LITHOGRAPHY

3.1 Introduction

Based on the model described in Chapter 2, a simulation tool called ILSIM has been developed (Appendix A1). Simulation examples of hyper-NA interferometric imaging are presented this chapter to illustrate some special phenomena associated with hyper-NA imaging. Examples in section 3.2 are intended to manifest polarization effects at hyper-NAs. In the first case, a uniform media is used to study the imaging properties of different polarization states. The second case is focused on the effects of substrate reflection on imaging in the resist layer at different polarization states. Then, examples are given on optimizing BARC parameters. Finally, the optical properties for hyper-NA resists are discussed.

3.2 Polarization Effects at Hyper-NA Interferometric Imaging

The imaging dependence on polarization at hyper-NA is one of the most important attributes that makes invalid the scalar approximation used for low NA imaging. As was discussed in Chapter 2, two-beam interference is a special case of the projection imaging. Therefore, hyper-NA two-beam interference is also polarization

dependent. The polarization effects at hyper-NA interferometric imaging will be discussed in this section.

3.2.1 Two-beam interference in a uniform media

In a uniform media, the polarization dependence is manifest in Equation [2-6] and Equation [2-12], which describe the two-beam interference in a uniform media with TE and TM polarization respectively

$$I_{TE} \propto 2|\mathbf{E}_1|^2[1+\cos(2kx\sin\theta)], \qquad [2\text{-}6]$$

$$I_{TM} \propto 2|\mathbf{E}_1|^2[1+\cos(2kx\sin\theta)\cos(2\theta)]. \qquad [2\text{-}12]$$

For both polarizations, the pitch of the sinusoidal interference fringe depends on the interference angle θ, where pitch, $p=\frac{\lambda}{2\sin\theta}$. However, the visibility or the contrast of the fringe depends on the polarization sate and the interference angle θ. Image contrast is defined as

$$C=\left|\frac{I_{max}-I_{min}}{I_{max}+I_{min}}\right| \qquad [3\text{-}1]$$

where I_{max} and I_{min} is the maxima and minima intensities of the fringe. Then the contrast for TE polarization and TM polarization can be expressed as

$$C_{TE}=1, \qquad [3\text{-}2]$$

$$C_{TM}=\cos(2\theta), \qquad [3\text{-}3]$$

The contrast for TE polarization is always 1 but the contrast for TM polarization is a function of the interference angle θ, cos(2θ). The underlying physics is that for TE polarization, the electrical vectors of the two interfering beams are always parallel to each

other at any interference angle θ but for TM polarization, the electrical vectors of the two interfering beams are with an angle 2θ relative to each other. For TM polarization, the contrast is zero at $\theta = \frac{\pi}{4}$. It is negative for $\theta > \frac{\pi}{4}$, which means that the fringe bright stripes and dark stripes switch positions, a phenomenon called "image reversal" in imaging science. This is more obvious if rearranging Equation [2-12] as

$$I_{TM} \propto 2|\mathbf{E}_1|^2[1+\cos(2kx\sin\theta)]\cos^2\theta + 2|\mathbf{E}_1|^2[1-\cos(2kx\sin\theta)]\sin^2\theta . \quad [3\text{-}4]$$

The first term is the decomposed component on the x direction, which behaves the same as TE polarization. The second term is the decomposed component on the z direction, which is π out of phase with the x component. If $\theta < \frac{\pi}{4}$, the x component predominate but the contrast is somewhat cancelled by the z component. If $\theta > \frac{\pi}{4}$, the z component predominate then we see the image reversal. In a medium with refractive index of n, the corresponding NA of the reversal point is

$$NA = n\sin\frac{\pi}{4} \quad [3\text{-}5]$$

Using unpolarized illumination, the field distribution is the average of TE imaging and TM imaging. In this case, the image reversal is not seen but the contrast decreases towards high NA values, finally reaching to zero at $\theta = \frac{\pi}{2}$. In Figure 3.1, 2-Beam interferometric imaging at a wavelength of 193 nm in a uniform media with refractive index of 1.70 is shown, with TE, TM and unpolarized imaging compared at various NA's.

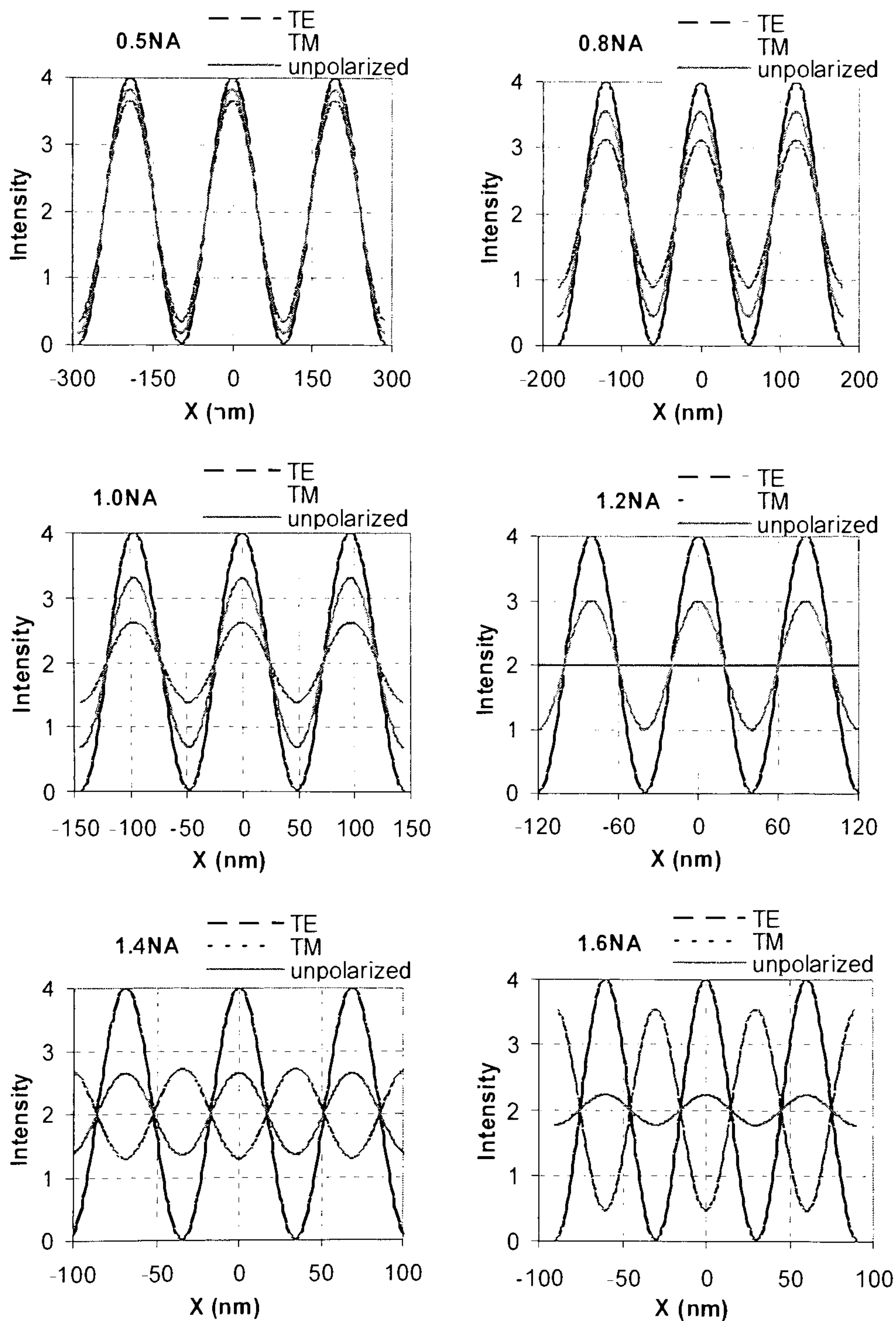

Figure 3.1 Two-Beam interferometric imaging at a wavelength of 193 nm in a uniform media with refractive index of 1.70. TE, TM and unpolarized imaging are compared at various NA's. Relative Intensity is plotted versus position.

At low NA's (<0.5), TE polarization and TM polarization behave in a closely similar way, indicating negligible polarization effects. Starting at around 0.8NA, TM polarization imaging begins losing contrast. The contrast is completely lost at 1.2NA. Image reversal starts appearing at higher NA's. The absolute value of the contrast of the reversed image finally reaches 1.0 at 1.7NA. The contrast for the image with unpolarized illumination, however, keeps decreasing as the NA is increased and finally reaches zero at 1.7NA. The refractive index of a 193-nm lithography resist is typically around 1.70. Therefore, the above discussion covers the representative scenarios of polarization effects for hyper-NA imaging.

3.2.1 Two-beam interference in a resist assembly

In the previous section, the polarization effects for hyper-NA interferometric imaging in a uniform media were discussed. However, the recording media is often in the form of a resist film, which is one layer of film in a film assembly. If there is reflection from below the resist layer, standing wave nodes and anti-nodes will be formed within the resist layer. At low oblique angles, there is little distinction between TE and TM polarizations. At high oblique angles, the electric vector of the incident wave with TM polarization is rotated 2θ upon reflection at the interface. This rotation makes the interferometric light distribution within the resist layer well beyond just nodes and anti-nodes, while it is just nodes and antinodes for TE polarization. The phenomena are well described by Equations [2-31, [2-32] and [2-38] introduced in Chapter 2.

$$F_S = \left[\frac{\tau_I}{\tau_{III}}\right]_S \left(e^{i\frac{2\pi N_2}{\lambda}(d_2 - z)\cos\theta_2} + \left[r_{III}\right]_S e^{-i\frac{2\pi N_2}{\lambda}(d_2 - z)\cos\theta_2} \right) \qquad [2\text{-}31]$$

$$F_{xP} = \left[\frac{\tau_I}{\tau_{III}}\right]_{xP} \left(e^{i\frac{2\pi N_2}{\lambda}(d_2-z)\cos\theta_2} + [r_{III}]_{xP}\, e^{-i\frac{2\pi N_2}{\lambda}(d_2-z)\cos\theta_2} \right) \qquad [2\text{-}32]$$

$$F_{zP} = \frac{N_0 \cos\theta_0}{N_2 \cos\theta_2}\left[\frac{\tau_I}{\tau_{III}}\right]_{xP} \left(e^{i\frac{2\pi N_2}{\lambda}(d_2-z)\cos\theta_2} - [r_{III}]_{xP}\, e^{-i\frac{2\pi N_2}{\lambda}(d_2-z)\cos\theta_2} \right) \qquad [2\text{-}38]$$

Equation [2-31] describes the standing wave effects with TE polarization. The first term of the equations is the downward propagating component, the second term the upward propagating component. The reflection coefficient $[\mathbf{r}_{III}]_S$ determines the magnitude of the standing wave. The standing wave effects for the TM polarization are much more complex due to the wave electrical vector rotation upon reflection. To apply vector calculations, the wave field is decomposed into x and z components. The standing wave effects of the x and z components are governed by Equation [2-32] and Equation [2-38] respectively. It is noted that the x component behaves in the same fashion as TE polarization but the z component is π out of phase with the x component. Recall that the interference fringe of the z component is π out of phase with that of the x component. As a result, a bright area of z component tends to appear in the center of four neighboring bright areas of x component. This endows TM imaging with special characteristics, which will be exhibited in the following simulations examples.

Figures 3.2 through 3.7 are the simulation results of light intensity distribution within the resist layer for two-beam interference at various NA values. The intensity contours are plotted versus resist film thickness Z and lateral position X. The film assembly parameters are listed in Table 3.1. Figure 3.2 shows the results of 0.5 NA imaging with TE and TM polarizations. It is noted that the contours for TE polarizations

have elliptical shapes while the contours for TM polarizations have rounded rectangular shapes. This is a result of the contribution from the z component of the TM polarization. The bright areas of z component, appearing in the centre of four neighboring bright areas of x component, stretch out the four corners of an ellipse to form a rounded rectangular shape. The effect is more pronounced at 0.8NA since there are more contributions from the z component. At 1.0NA and 1.2NA, the contribution from z component becomes more noticeable, forming rounded rectangular contour shapes in between the rectangular contour lattice of x component. At higher NA values (1.4NA, 1.6NA), the contribution from x component instead gets less noticeable, as is shown in Figure 3.6 and Figure 3.7. Also, it is noted that the number of nodes gets fewer at higher NA values. This is because that the wave propagation phase through the resist film is a function of oblique angle, as shown in Equation [2-19]

$$\delta_j = \frac{2\pi d_j N_j \cos\theta_j}{\lambda} . \qquad [2\text{-}19]$$

At higher oblique angles, the propagation phase gets smaller, so we see less number of standing wave nodes.

Table 3.1 Optical constants and film thickness for resist assembly used for simulation in Section 3.2.1

Immersion Fluid, N_0=1.437
Top coat, N_1=1.414, d_1=40nm
Resist, N_2=1.71-0.039i, d_2=300 nm
Substrate N_{sub}=0.87-2.76i

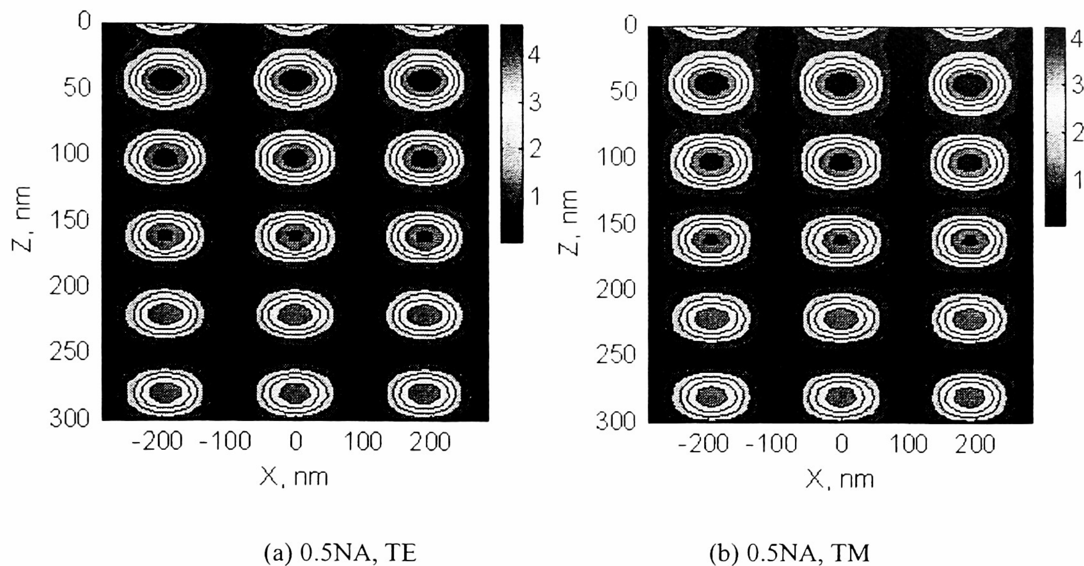

(a) 0.5NA, TE (b) 0.5NA, TM

Figure 3.2 Intensity contours versus resist film thickness Z and lateral position X for 0.5NA two-beam interference. The film assembly parameters are listed in Table 3.1.

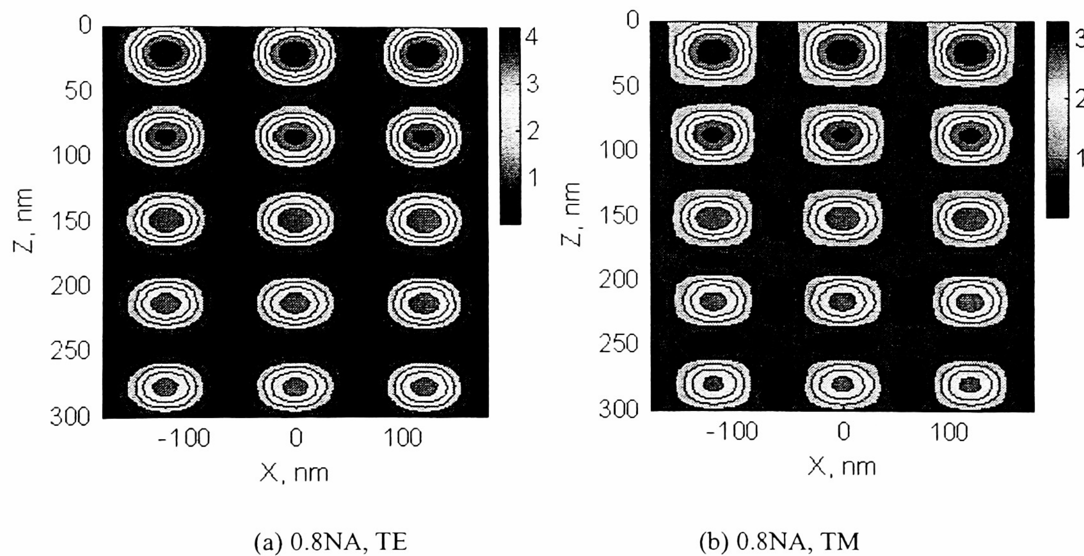

(a) 0.8NA, TE (b) 0.8NA, TM

Figure 3.3 Intensity contours versus resist film thickness Z and lateral position X for 0.8NA two-beam interference. The film assembly parameters are listed in Table 3.1.

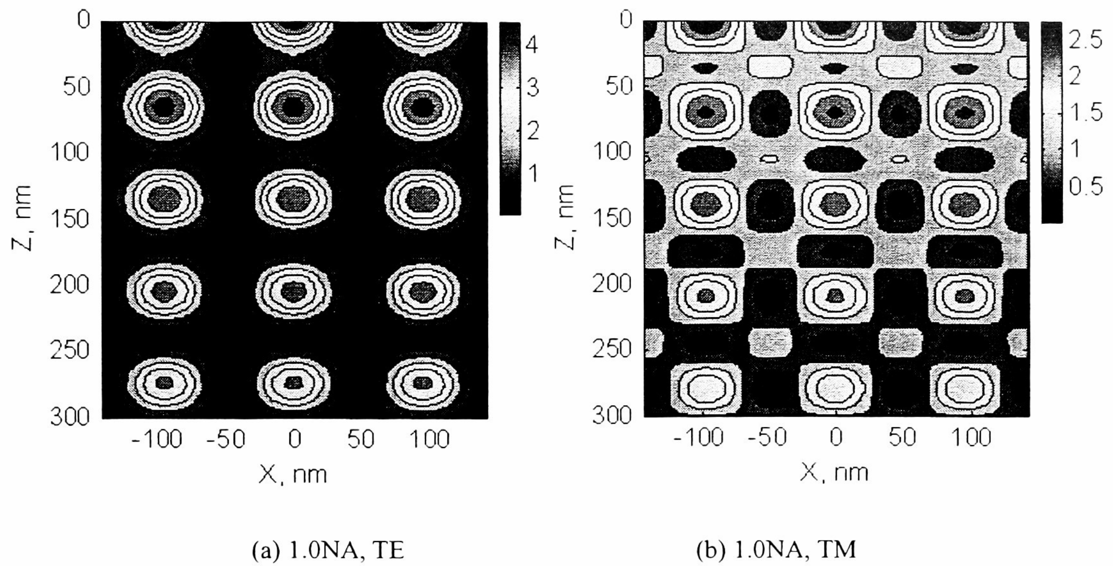

(a) 1.0NA, TE (b) 1.0NA, TM

Figure 3.4 Intensity contours versus resist film thickness Z and lateral position X for 1.0NA two-beam interference. The film assembly parameters are listed in Table 3.1.

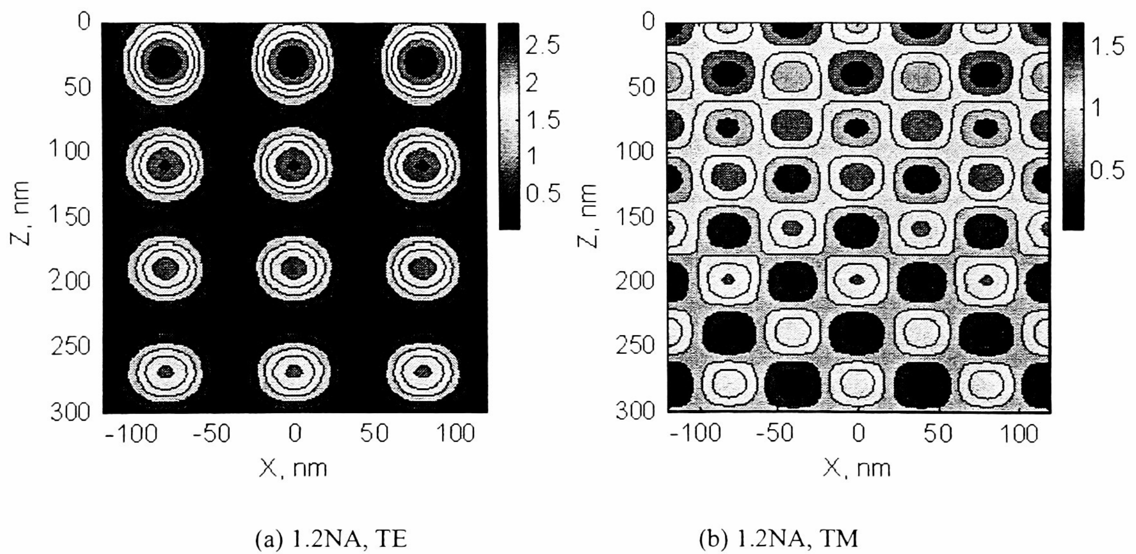

(a) 1.2NA, TE (b) 1.2NA, TM

Figure 3.5 Intensity contours versus resist film thickness Z and lateral position X for 1.2NA two-beam interference. The film assembly parameters are listed in Table 3.1.

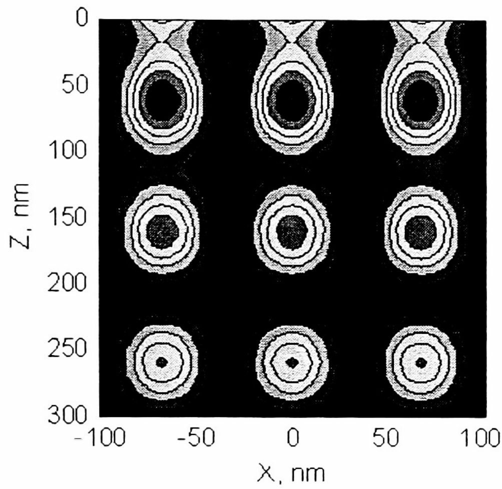

(a) 1.4NA, TE

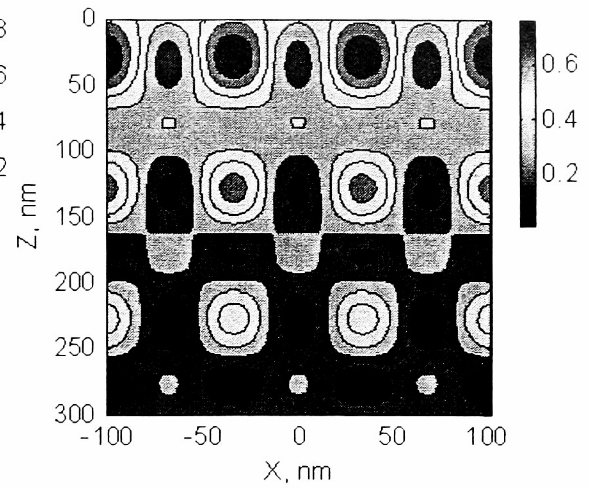

(b) 1.4NA, TM

Figure 3.6 Intensity contours versus resist film thickness Z and lateral position X for 1.4NA two-beam interference. The film assembly parameters are listed in Table 3.1.

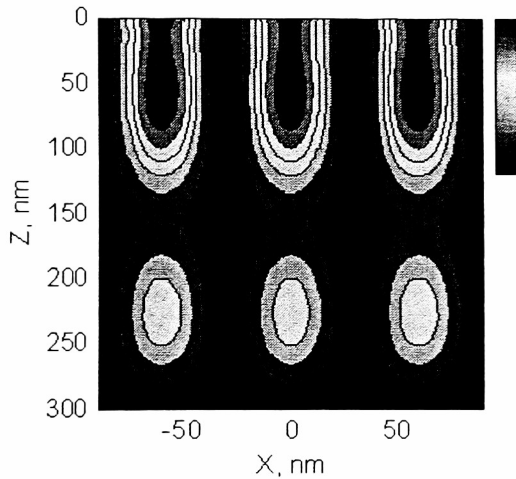

(a) 1.6NA, TE

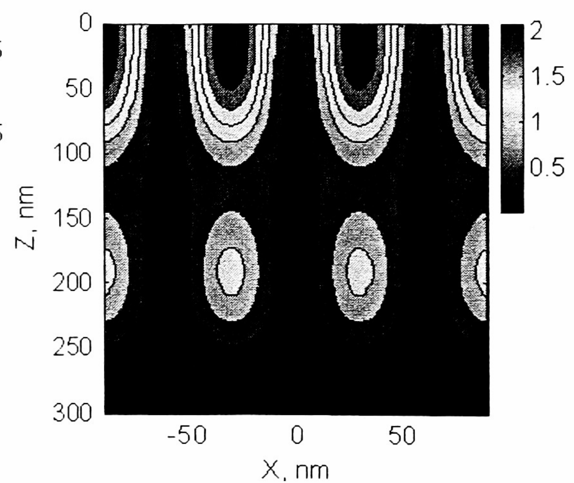

(b) 1.6NA, TM

Figure 3.7 Intensity contours versus resist film thickness Z and lateral position X for 1.6NA two-beam interference. The film assembly parameters are listed in Table 3.1.

3.3 Bottom AR coatings for Hyper-NA Imaging

The simulation results in the previous section have shown that the reflection from the substrate could form standing waves within the resist film in the vertical direction. Standing waves usually causes fluctuations in line width, even causes resist pattern collapses at extreme cases. At hyper-NA imaging, this issue becomes more serious since the substrate reflects more incident light with high oblique angles. To address those issues, bottom antireflective coatings (BARCs) are used extensively in lithographic practice to eliminate standing waves. As indicated by Equation [2-28], the amplitude of the standing wave is determined by r_{III}, the effective reflection coefficient at the bottom interface of the resist film. In accordance with equation [2-21], r_{III} can be expressed as

$$r_{III} = \frac{B\eta_2 - C}{B\eta_2 + C} \quad [3\text{-}6]$$

where η_2 is the oblique optical admittance of the resist layer, $\begin{bmatrix} B \\ C \end{bmatrix}$ is the characteristic matrix for the sub film assembly below the resist layer. Assume there is only one BARC layer with oblique optical admittance of η_3 thickness of d_3 above the substrate, then

$$r_{III} = \left(\eta_2 - \frac{\eta_{sub}\cos\delta + i\eta_3 \sin\delta}{\cos\delta + i(\eta_{sub}/\eta_3)\sin\delta} \right) \Big/ \left(\eta_2 + \frac{\eta_{sub}\cos\delta + i\eta_3 \sin\delta}{\cos\delta + i(\eta_{sub}/\eta_3)\sin\delta} \right). \quad [3\text{-}7]$$

That is

$$r_{III} = \frac{(\eta_2 - \eta_{sub})\cos\delta + i(\eta_2\eta_{sub}/\eta_3 - \eta_3)\sin\delta}{(\eta_2 + \eta_{sub})\cos\delta + i(\eta_2\eta_{sub}/\eta_3 + \eta_3)\sin\delta}. \quad [3\text{-}8]$$

There are many solutions leading to $r_{III} = 0$. One obvious one solutions is that,

$$\eta_2 = \eta_3 = \eta_{sub} \quad [3\text{-}9]$$

But that means it is a uniform system which is a special case. If all the refractive indices are real (transparent materials), there is another solution that is

$$\begin{cases} \cos\delta = 0 \\ \eta_2\eta_{sub}/\eta_3 - \eta_3 = 0 \end{cases} . \quad [3\text{-}10]$$

Then we have

$$\delta = \frac{2\pi d_3 n_3 \cos\theta_3}{\lambda} = \left(\frac{1}{2} + k\right)\pi \quad [3\text{-}11]$$

$$\eta_3 = \sqrt{\eta_2\eta_{sub}} \quad [3\text{-}12]$$

where k is a non-negative integer.

The BARC layer refractive index n_3 can be found from Equation [3-12] for cases of TE polarization and TM polarization respectively

$$n_3 = \frac{\sqrt{n_2 \cos\theta_2 n_{sub} \cos\theta_{sub}}}{\cos\theta_3} \qquad \text{TE polarization} \quad [3\text{-}13]$$

$$n_3 = \cos\theta_3 \sqrt{\frac{n_2 n_{sub}}{\cos\theta_2 \cos\theta_{sub}}} \qquad \text{TM polarization} \quad [3\text{-}14]$$

where θ_3 and θ_{sub} can found using Snell's law ($n_2 \sin\theta_2 = n_3 \sin\theta_3 = n_{sub} \sin\theta_{sub}$).

For normal incidence, the above equations are reduced to the familiar equation

$$n_3 = \sqrt{n_2 n_{sub}} \qquad \text{Normal incidence.} \quad [3\text{-}15]$$

The BARC layer thickness d_3 can be found from Equation [3-11]

$$d_3 = \left(\frac{1}{4} + \frac{k}{2}\right)\frac{\lambda}{n_3 \cos\theta_3} . \quad [3\text{-}16]$$

Equation [3-13] and Equation [3-14] indicate that we will never have a solution that works for both TE and TM for oblique incidence. In other words, an ideal single layer BARC does not exist for unpolarized oblique incidence.

In deriving the above solutions, we have assumed that the resist layer and the substrate are transparent. However, the substrates in lithographic practice are often non-transparent, where the above solutions are not particularly useful. In the case of non-transparent substrates, their optical constants are complex numbers. Then the solution to Equation [3-8] is not straightforward since all the oblique optical admittances and phase factors are complex numbers. Instead, a numerical resort is necessary. A solution to Equation [3-8] requires that the real part and imaginary part of the equation vanish. Since there are three unknowns (n, k and thickness of the BARC layer) and two equations, a family of solutions is expected. An example of BARC parameter calculation for 1.4NA imaging is given in Figure 3.8. In the figure, the reflectance from the BARC-resist interface is plotted versus BARC thickness. The refractive index of the resist is 1.71-0.039i and the refractive index of the silicon substrate is 0.87-2.78i. The minimum reflectance thickness is a function of complex refractive index of the BARC material, n and k. The complex refractive index can be varied so that the first or the second reflectance minimum reaches zero. The corresponding n, k and thickness are the parameters for an ideal BARC. A larger k value for the first minimum reflectance thickness is needed than that for the second minimum reflectance thickness since the reflected light from the substrate undergoes longer path for the second minimum thickness. It is also noted that the corresponding minimum thickness is thinner for materials with larger n values. The existence of multiple solutions to an optimized bottom

anti-reflective coating seems messy in the aspect of mathematics but they do offer more options for BARC materials.

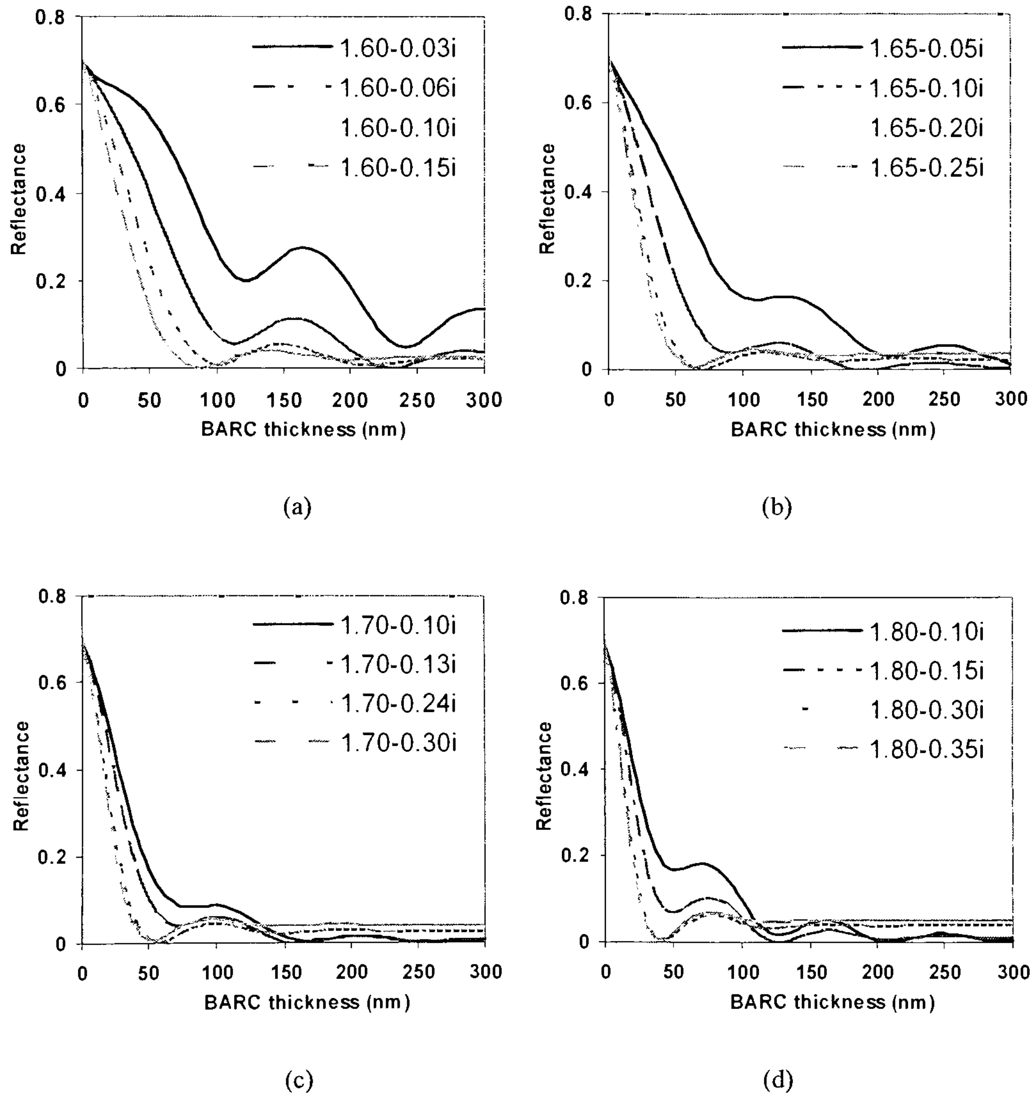

Figure 3.8 Reflectance at the BARC-resist interface versus BARC thickness at various refractive indices of BARC materials for 1.40 NA imaging. (a) n=1.60, k=0.03, 0.06, 0.10, 0.15; (b) n=1.65, k=0.05, 0.10, 0.20, 0.25; (c) n=1.70, k=0.10, 0.13, 0.24, 0.30; (d) n=1.80, k=0.10, 0.15, 0.30, 0.35;

The preceding analysis on BARC parameters have been focused on two-beam interference with which there is only one angle of incidence is involved. However, when a large range of incident angles are involved, as is the case for a projection system with random geometrical features on the mask, things becomes more complicated to come up with an ideal BARC. In theory, a gradient BARC layer is needed to reduce the reflectance to zero over the whole angle range. In practice, a multi-layer BARC system would be sufficient to reduce the reflectance to a tolerable extent over a desired range of angle of incidence.

3.4 Resists for Hyper-NA Imaging

Obviously, lots of issues need to be addressed for resists used for hyper-NA imaging, including chemical properties and physical properties. This section discusses the optical properties that are related to hyper-NA imaging. One aspect that distinguishes hyper-NA imaging from traditional low-NA imaging is that the oblique beam travels much longer in the resist layer than the resist film thickness itself. The situation is depicted in Figure 3.9. Assume d is the thickness of the resist, and n-ik is the complex index of the resist, then the beam path length d′ in the resist is expressed in Equation [3-17]

$$d' = \frac{d}{\sqrt{1 - \sin^2\theta}} \qquad [3\text{-}17]$$

where θ is the oblique angle of plane wave in the resist film. At hyper-NA imaging, the difference between d and d′ are not negligible any more. That means that the oblique plane wave experiences more absorption by the resist material than the normal incident beam. In lithographic practice, it is required that the resist be transparent to certain extent

so that the resist line size is uniform across the depth of the resist film. Suppose that we need the optical transmittance of the resist film to be T (here the absorption related transmission is considered, and the reflection at the interfaces any scattering are not considered), the imaginary part of the complex refractive index of the resist, k, can be expressed in Equation [3-18] and in Equation [3-19], respectively for normal incidence and hyper-NA incidence

$$k = \frac{-\lambda \ln(T)}{4\pi d}, \qquad [3\text{-}18]$$

$$k = \frac{-\lambda \ln(T)}{4\pi d}\sqrt{1-\sin^2\theta}\,. \qquad [3\text{-}19]$$

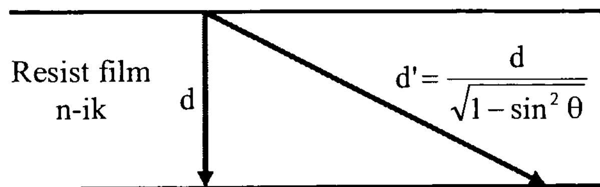

Figure 3.9 Illustration for the oblique beam which experiences a longer path in the resist film than the film thickness. At hyper-NA imaging, the difference is not negligible any more.

To compare the resist absorption effect at hyper-NA imaging, some two-beam interference simulation results are shown in Figure 3.10. In the simulation, the substrate is index match with the resist. The intensity contours are plotted versus resist film thickness Z and lateral position X. The resist complex refractive index is 1.71-0.039i for Figure 3.10 (a) and (b). At 1.05NA, there is negligible intensity attenuation through the depth of the resist film. Actually, the index is of a commercial resist designed for 1.05NA imaging. However, at 1.66NA, the intensity is attenuated to 50% at the bottom of the

resist film. In accordance with Equation [3-19], reducing k to 0.0094 will make the attenuation effect negligible at 1.66NA, as shown in Figure 3.10 (c) and (d).

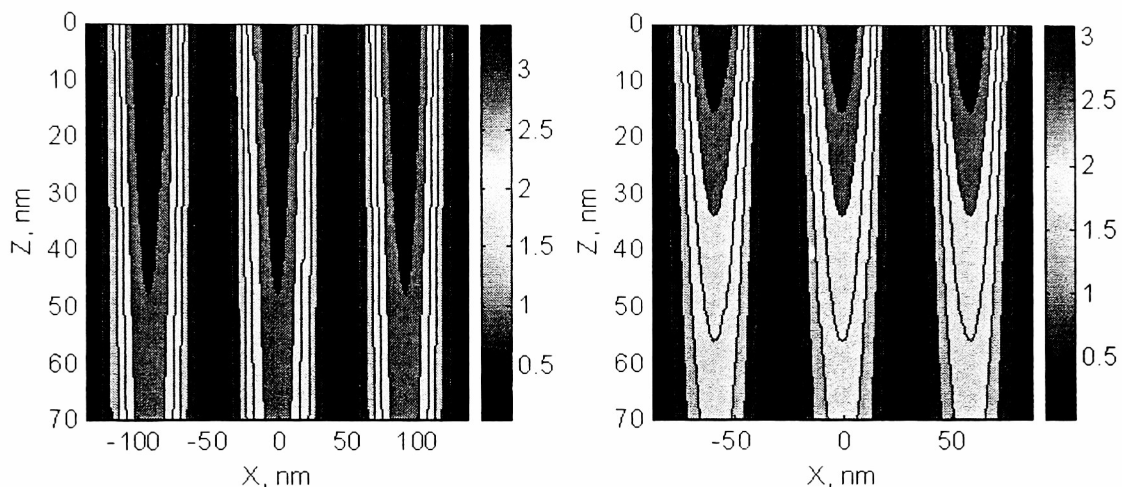

(a) 1.05NA, 1.71-0.039i;

(b) 1.66NA, 1.71-0.039i;

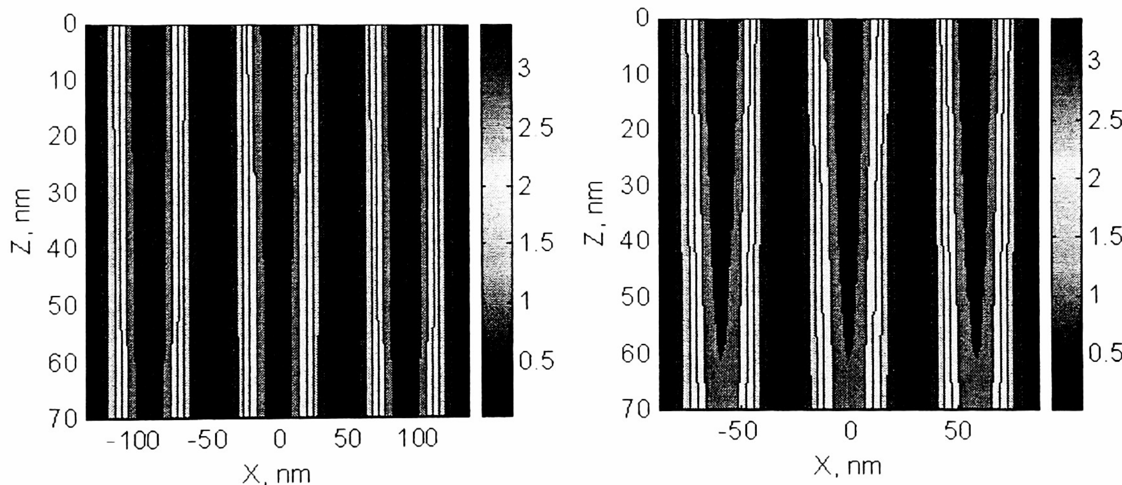

(c) 1.05NA, 1.71-0.0094i;

(d) 1.66NA, 1.71-0.0094i;

Figure 3.10 Simulation results of light intensity distribution within the resist layer for two-beam interference. The substrate is index match with the resist. The intensity contours are plotted versus resist film thickness Z and lateral position X. The absorption effects at 1.05NA and 1.66NA are compared with two different resist indices.

3.5 Summary

In this chapter, simulation examples of hyper-NA interferometric imaging were discussed with regard to some special phenomena associated with hyper-NA imaging. Polarization effects were discussed in section 3.2. Interference fringe contrast from TE polarization illumination is independent of interference angle unlike interference fringe contrast from TM polarization which is a function of interference angle, *i.e.*, cos(2θ). The contrast of TM polarization interference fringe decreases as the interference angle is increased, reducing to zero at an angle of $\frac{\pi}{4}$ and becoming negative (reversed image) beyond that. In the presence of a reflective substrate, the standing wave effects depend on the polarization states. This is a result that the z component of the reflection coefficient of TM polarization is π out of phase relative to the x component of the reflection coefficient of TM polarization. At hyper-NA imaging, the optimal parameters of a BARC layer is a function of NA. If the substrate is transparent, an analytical solution can be found for the BARC layer. For the usual case of a non-transparent substrate, numerical solutions are often used for the optimal BARC parameters. Due to the fact that the oblique beams travel much longer than the thickness of resist film itself, resists for hyper-NA imaging demands a much lower value of k, the imaginary part of the complex refractive index of the resist.

CHAPTER 4

EXPERIMENTAL APPROACHES

4.1 Introduction

The vector interference theory and the numerical simulation results were discussed in Chapter 2 and Chapter 3. This chapter is intended to describe the experimental approaches to predict theoretical predictions. A two beam interference setup is first introduced. Immersion interferometric imaging is performed using a half ball, half cylinder or prism.

4.2 Setup for 2-Beam Interferometric Immersion Lithography

A schematic of the two-beam interferometric system to be employed for immersion lithography is shown in Figure 4.1. A photograph of the experimental setup is shown Figure 4.2. The laser beam, after expansion, polarization and spatial filtering, is split by a phase-shifting grating into a series of diffraction orders. With the residual zero order and other higher orders being blocked, the first orders are directed at oblique angles toward the center of a half cylinder interfaced with a wafer coated with resist. The interference fringe pitch is determined by the source wavelength λ, the refractive index of the half cylinder n and the oblique angle θ

$$p = \frac{\lambda}{2n\sin\theta}. \quad [4\text{-}1]$$

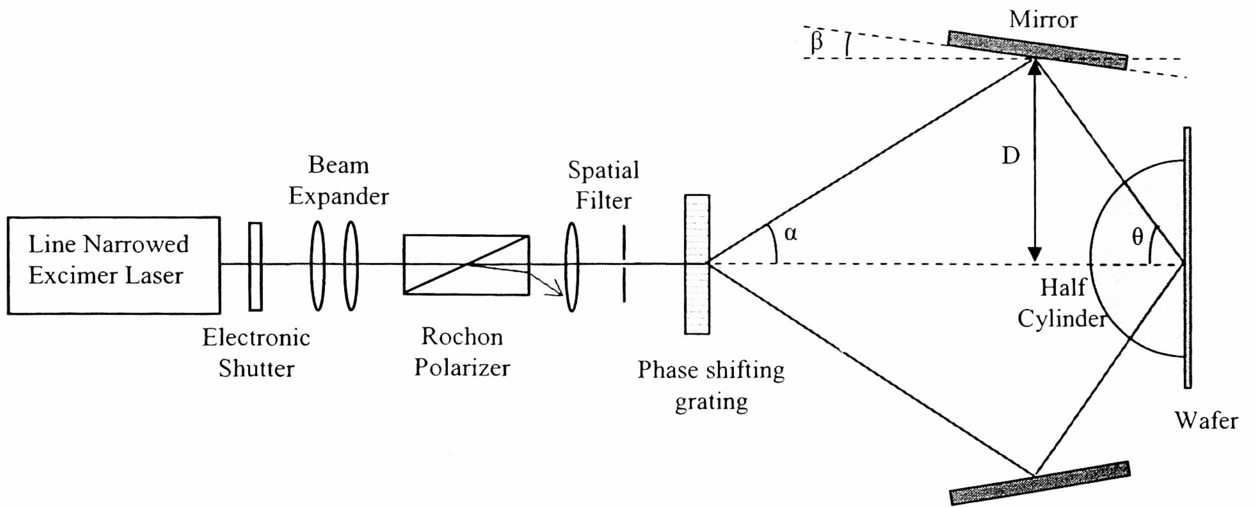

Figure 4.1 Schematic of interferometric immersion lithography setup.

Figure 4.2 Photography of the interferometric immersion lithography setup.

4.3 Half Cylinders, Half Balls and Prisms

In the experimental set-up shown in Figure 4.1, two beams are directed at an oblique angle toward the center of a half cylinder interfaced with a wafer coated with resist. Since the beam is perpendicular to the half cylinder surface, the incident angle does change. Therefore, the maximum NA is determined by the refractive index of the half cylinder or half ball. For fused silica, the maximum obtainable NA is 1.56 at the wavelength of 193 nm. A half ball can function in the same way. To pursue higher NA values, aluminum oxide with a refractive index of 1.92 at the wavelength of 193 nm can be used. Since aluminum oxide is a birefringent material, correct optical axis alignment in the set up is needed so that the birefringence can be avoided. As shown in Figure 4.3, the optical axis of an aluminum oxide is set normal to the flat surface of the half cylinder. Then, the incident TE polarized beams behave as an ordinary ray. Or, the optical axis is set parallel to the axis of the cylinder, then the TE polarized beam behaves as an extraordinary ray.

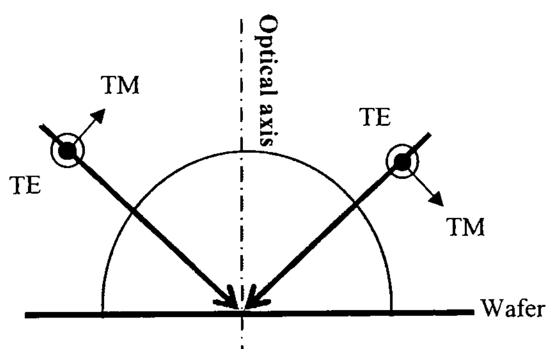

Figure 4.3 Aluminum oxide half cylinder used for high NA coupling. The optical axis of the uniaxial crystal is aligned normal to the flat surface of the half cylinder or parallel to the axis of the cylinder. Incident TE polarized light behaves as ordinary ray or extraordinary ray.

Alternatively, an equilateral triangle aluminum oxide prism can be used for high NA coupling, as shown in Figure 4.4. the optical axis of an aluminum oxide is set normal to the surface interfaced with wafer. Then, the incident TE polarized beams behave as an ordinary ray. Or, the optical axis is set parallel to the axis of the triangle prism, then the TE polarized beam behaves as an extraordinary ray. If the incident beam is normal to the triangle side surface, then the incident angle θ in the prism is 60°. If it is not normal to the triangle side surface, the incident angle θ in the prism can be calculated using Equation [4-2].

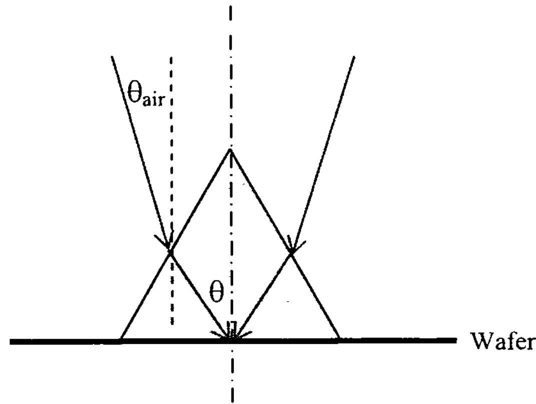

Figure 4.4 Equilateral triangle aluminum oxide prism used for high NA coupling. The optical axis of the uniaxial crystal is aligned normal to the surface interfaced with the wafer or aligned perpendicular the triangle surface. Incident TE polarized light behaves as ordinary ray or extraordinary ray.

$$\theta = \frac{\pi}{3} - \arcsin\left[\frac{\sin(\pi/3 - \theta_{air})}{n}\right] \qquad [4\text{-}2]$$

where n is the refractive index of the equilateral triangle prim, θ_{air} is the incident angle in the air, as is illustrated in Figure 4.4. The angle θ_{air} ranges from 0° to 90°. The

correspondent θ ranges from 33.2° to 90°. For aluminum oxide (n=1.92), the NA ranging from 1.05 to 1.93 is obtainable with this equilateral triangle prism.

4.4 Illumination Source

As discussed in the precious sections, 193-nm ArF excimer lasers are the workhorse in the current technology and apparently will be the light source for 193-nm immersion lithography. Due to the lack of a well-defined ground state of excimers for the energy level transition that defines the laser wavelength, the free-run excimer laser's spectral line width is about 0.5nm, which is much wider than most lasers. In addition to low temporal coherence, excimer lasers have a very low degree of special coherence in that a large number of transverse modes are operated in the laser cavity. Low coherence is desirable in order to eliminate interference patterns within the aerial image. However, a high degree of coherence is indispensable in interferometric imaging. Modifications of conventional excimer lasers are needed to afford a degree of coherence workable for interferometric imaging. High degree of spatial coherence is achieved using the unstable resonators, where the basic transverse mode is easier to be separated from higher order modes for basic single mode output. To narrow spectral line width, wavelength disperse optical elements such as diffraction gratings, prism and/or etalons have been introduced in the resonator. A compact OpTexPro TROM ArF excimer laser from Lambda Physik in our laboratory utilizes a combination of prism and diffraction grating to produce a spectral line width of 2 pm, with the correspondent temporal coherence length of 18 mm.

4.5 Polarization Control

The output beam from the laser is linearly polarized to some extend but a high extinction polarization state is necessary for the interferometric imaging study. A Magnesium Fluoride Rochon polarizer will be used for this purpose. As illustrated in Figure 4.5, the Rochon polarizer is made of two optically contacted right angle prisms with their optical axis orthogonal to each other. Because of the birefringent nature of the MgF_2 at the wavelength of 193 nm, the output is split into two orthogonally polarized beams. The ordinary beam passes through the prism without deviation while the extraordinary beam is deflected at a deviation angle. At the wavelength of 193 nm, the deviation angle is 5.5°. The ordinary beam will be used for interferometric imaging. The Rochon polarizer is orientated to a direction such that the major polarization component passes through the polarizer as the ordinary beam, making best use of the laser power. The high extinction linearly polarized ordinary beam will be used for TE and TM imaging studies. If the polarization direction has an angle of $\frac{\pi}{4}$ with respect to TE and TM, it will be decomposed into TE and TM equally, which effectively emulates unpolarized or circularly polarized imaging.

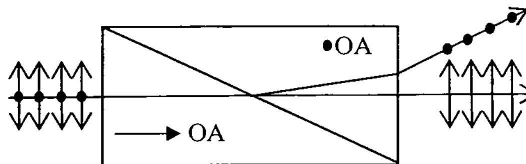

Figure 4.5 A schematic of Rochon polarizer. The optical axes of the two prisms are orthogonal to each other. The output is split into to orthogonally polarized beams. The ordinary beam passes without deviation while the extraordinary beam is deflected.

4.6 Summary

The experimental approaches to predict theoretical predictions were described in detail in this chapter. A two beam interference setup along with a half ball, half cylinder or prism is used for interferometric immersion lithographic studies. The polarization state is controlled by a combination of a Rochon polarizer and a half wave plate. The optical characteristics of the setup will be analyzed in the next chapter.

CHAPTER 5

ANALYSIS OF THE EXPERIMENTAL SETUP CONFIGURATION

5.1 Introduction

This chapter is focused on discussing the special optical characteristics of the interferometric lithography setup described in Chapter 4. One of the interesting characteristics is the setup's response to laser beam direction fluctuations due to laser pointing instability,[65] mechanical resonant vibration, environmental vibration, etc. To analyze the response, a simple geometrical ray tracing and basic interference theory are applied to relate beam tilt angle with interference fringe displacement, which induces fringe contrast loss. The relationship will provide a good understanding of how the interference fringe is blurred by beam tilting. In addition, the setup's dependence on the source's temporal coherence and spatial coherence will be analyzed, aware of which the source coherence requirements could be eased with a properly configured setup.

5.2 Effects of Beam Pointing Instability on Imaging

In a research or a fabrication environment, there are many factors which can contribute to laser beam direction fluctuation, such as laser pointing instability, mechanical resonant vibration, environmental vibration, etc. Therefore, it is necessary to analyze their effects on interferometric lithography. For example, a typical laser with a

beam pointing stability of 20 μrad could cause a beam shift of 2μm after propagating a distance of 10 cm. Considering that we are printing sub-50 nm lines, 2μm is potentially disastrous. However, it should be noted that not every mode of beam direction fluctuation necessarily blurs interference fringe. Only beam tilt that causes fringe displacement (i.e. the change of the phase of the sinusoidal wave) will cause blurring, as is illustrated in Figure 5.1. In our experimental setup, a beam tilt in the direction perpendicular to the grating could cause fringe shift. In the following section, the phase shift of the fringe sinusoidal wave will be analyzed as a function of beam tilt angle, as well as a function of the setup configuration parameters.

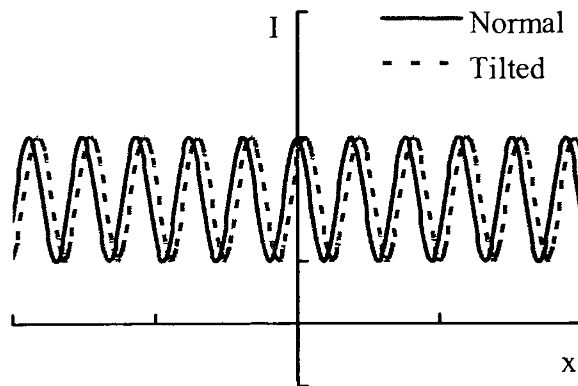

Figure 5.1 Shift of interference fringe from tilted beam relative to that from normal beam, causing imaging blurring.

A schematic illustrating laser beam tilt in the experimental setup used in this dissertation is shown in Figure 5.2. A normal incident beam is split by the phase grating into various diffraction orders, the first orders of which are redirected to interference at the wafer plane. The diffraction angle of the first orders is defined by

$$\sin\alpha = \pm\frac{\lambda}{p}. \qquad [5\text{-}1]$$

To achieve an interference angle θ at the wafer plane, a mirror tilt angle of β is required,

$$\beta = \frac{\theta - \alpha}{2}. \qquad [5\text{-}2]$$

D is defined as the normal distance to the setup central axis from the point where the center of the beam hits the mirror. For a given grating pitch p, an interference angle θ, the mirror separation (2D) describes the size of the setup.

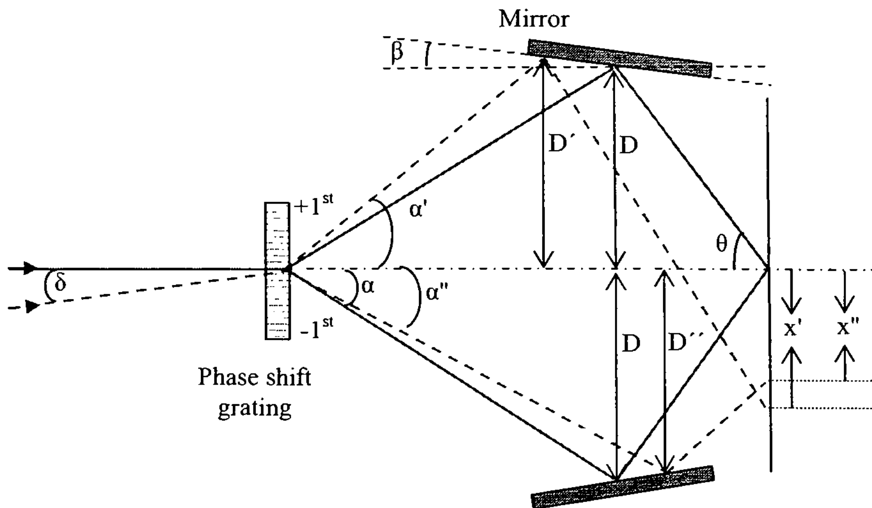

Figure 5.2 A schematic showing laser beam tilt. The solid beam is normal and the dashed beam is tilted by an angle of δ. The parameters used in the calculation are labeled in the figure.

Assume that the beam incident on the grating is tilted by an angle δ relative to normal due to vibration or laser point instability, then the diffraction angles of the first orders can be expressed by grating equation as

$$\sin\alpha' = \frac{\lambda}{p} + \sin\delta$$
$$\sin\alpha'' = \frac{\lambda}{p} - \sin\delta \qquad [5\text{-}3]$$

where α' and α'' are the +1 and -1 order diffraction angles respectively. For the +1 order, the center of the beam hits the mirror at a different point, from which the normal distance to the central axis, D' is related to D in the following equation

$$D\cot(\alpha) = D'\cot(\alpha') + (D'-D)\cot(\beta)\,. \qquad [5\text{-}5]$$

Rearrangement of the above equation gives

$$D' = \frac{D\cot(\alpha) + D\cot(\beta)}{\cot(\alpha') + \cot(\beta)} \qquad [5\text{-}6]$$

The distance L', from the grating, reflected by the mirror to the wafer plane can be derived as

$$L' = \frac{D'}{\sin(\alpha')} + \frac{D[\cot(\alpha) + \cot(\theta)] - D'\cot(\alpha')}{\cos(\theta')} \qquad [5\text{-}7]$$

where θ' is the incident angle to wafer normal, $\theta' = \alpha' + 2\beta$ The titled beam intersects with the wafer plane at a location which is x' from the central axis

$$x' = \frac{D[\cot(\alpha) + \cot(\theta)] - D'\cot(\alpha')}{\cot(\theta')} - D'\,. \qquad [5\text{-}8]$$

Similarly, the following relationships can be derived for the minus first order beam:

$$D\cot(\alpha) = D''\cot(\alpha'') - (D - D'')\cot(\beta) \qquad [5\text{-}9]$$

$$D''=\frac{D\cot(\alpha)+D\cot(\beta)}{\cot(\alpha'')+\cot(\beta)} \qquad [5\text{-}10]$$

$$L''=\frac{D''}{\sin(\alpha'')}+\frac{D[\cot(\alpha)+\cot(\theta)]-D''\cot(\alpha'')}{\cos(\theta'')} \qquad [5\text{-}11]$$

$$x''=D''-\frac{D[\cot(\alpha)+\cot(\theta)]-D''\cot(\alpha'')}{\cot(\theta'')} \qquad [5\text{-}12]$$

where $\theta''=\alpha''+2\beta$.

Therefore, the optical path distance between the plus and minus first orders on the wafer plane at the central axis is

$$OPD=n[(L'-x'\sin(\theta'))-(L''+x''\sin(\theta''))] \qquad [5\text{-}13]$$

where n is the refractive index of the media. The corresponding phase difference is

$$\begin{aligned}\phi&=\frac{2\pi}{\lambda}OPD\\&=\frac{2\pi n}{\lambda}[(L'-x'\sin(\theta'))-(L''+x''\sin(\theta''))].\end{aligned} \qquad [5\text{-}14]$$

Equation [5-14] is the basic equation that relate beam tilt angle with the phase shift of the resultant interference fringe. From this equation, the corresponding displacement of the fringe can be found, and subsequently the contrast loss. In section 3, the phase shift is analyzed as a function of various configuration parameters. In section 4, the effect of beam tilt with a statistical distribution is analyzed.

The phase shift due to beam tilt versus beam tilt angle is plotted in Figure 5.3. A grating pitch of $p=600\,\text{nm}$, mirror separation (2D) = 2cm, interference angle of $\theta=45°$, and source wavelength of $\lambda=193\,\text{nm}$ are used in the calculation. It is shown that a beam

tilt of 1° will cause a phase shift of π, which is the worst case causing imaging blurring. As the tilt angle goes higher, the phase shift oscillates between 0 and 2π, with an increasing oscillating frequency. Let's set up an arbitrary criterion that 0.01π (which approximately causes $\frac{\lambda}{100}$ fringe displacement) is the maximum phase shift that will not cause any noticeable image contrast loss. For the case shown in this plot, the maximum tolerable beam tilt angle is 0.15°.

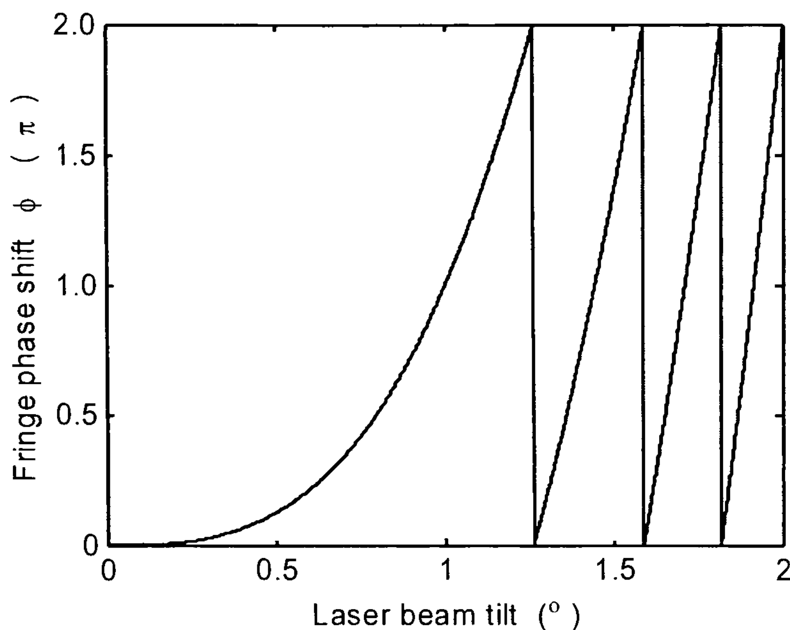

Figure 5.3 Fringe phase shift ϕ versus laser beam tilt angle. Grating pitch p = 600 nm, setup size D = 10 cm, wavelength λ = 193 nm, $\sin\theta$ = 0.707.

Setup size D is an important factor determining the phase shift ϕ. In Figure 5.4, the phase shift due to beam tilt is plotted versus tilt angle at various values of D. It shows that the phase shift due to beam tilt increases as the magnitude of D increases in a directly proportional relationship, as is indicated in the derivation of Equation [5-14].

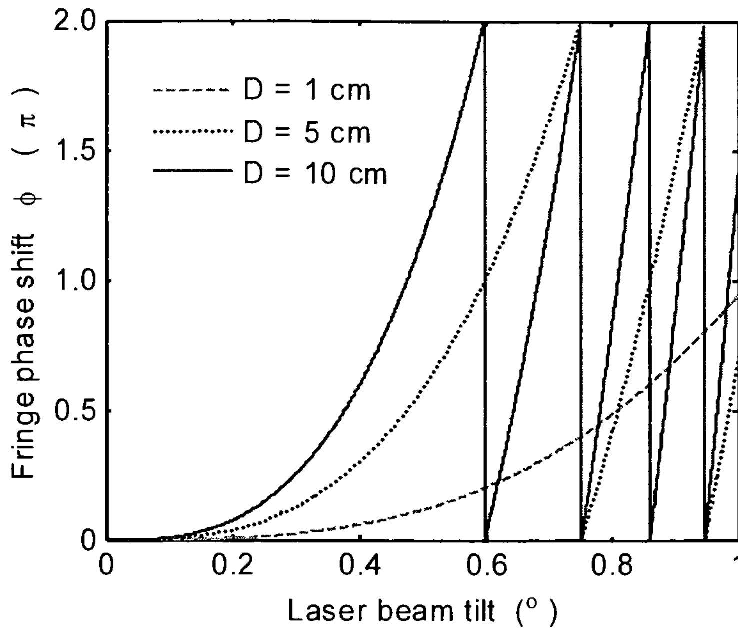

Figure 5.4 Fringe phase shift ϕ versus laser beam tilt angle for setup size D= 1 cm, 5 cm, 10 cm respectively. Grating pitch p = 600 nm, wavelength λ = 193 nm, sinθ = 0.707.

In Figure 5.5, the phase shift due to beam tilt is plotted versus tilt angle at various values of interference angle θ. It shows that the phase shift due to beam tilt is relatively non-sensitive to interference angle θ, especially at low tilt angles. This is an important property of the setup. If a certain degree of beam tilt (for example, due to some resonant vibration) does not wash out the fringe patterns at low θ values (i.e., low NA, loose pitches), it is not going to wash out the fringe patterns at high θ values either (i.e., low NA, tight pitches). This property makes it much easier to lay out the vibrations criteria for the interferometric system which is intended to work at various NA values.

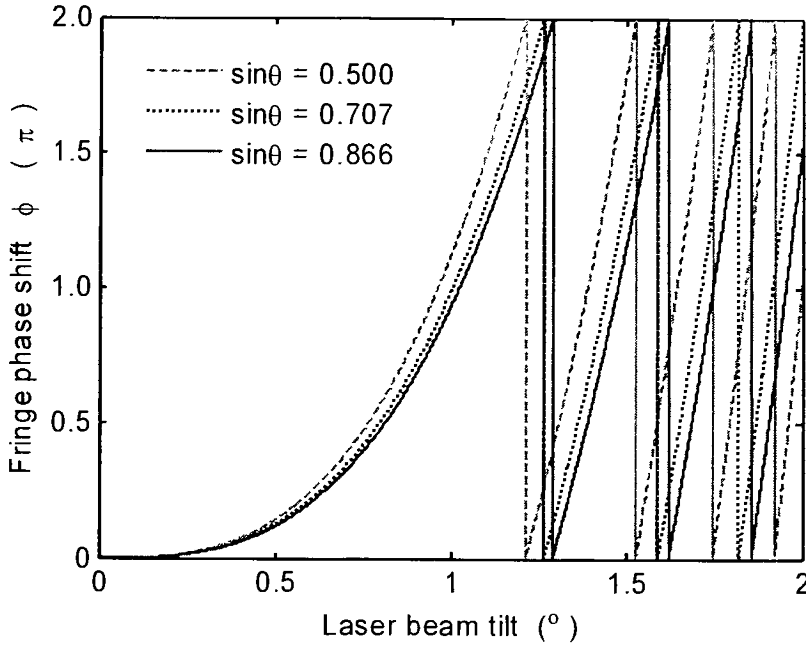

Figure 5.5 Fringe phase shift ϕ versus laser beam tilt angle δ for $\sin\theta=0.500$, $\sin\theta = 0.707$ and $\sin\theta = 0866$ respectively. Grating pitch p = 600 nm, wavelength λ = 193 nm.

In addition to the interference fringe shift (phase shift), laser pointing tilt also could result in change in the pitch of the fringe since the incident angles of the two beams on the wafer plane is a function of the laser tilt angle δ. The change in incident angles in turn induces interference fringe pitch change. As discussed in the proceeding, the incident of angle of the plus first order is θ' and the incident angle of the minus first order is θ'', then the electrical field at the wafer plane can be expressed as

$$\begin{aligned} \mathbf{E}_1 &= |\mathbf{E}_1| e^{-i(kx\sin\theta'+\phi)} \\ \mathbf{E}_2 &= |\mathbf{E}_2| e^{-i(-kx\sin\theta'')} \end{aligned} \qquad [5\text{-}15]$$

Following the same method described in chapter 2, the total field at the wafer plane in the case of TE polarization can be expressed as

$$\begin{aligned}\mathbf{E} = \mathbf{E}_1 + \mathbf{E}_2 &= |\mathbf{E}_1| e^{-i(kx\sin\theta' + \phi)} + |\mathbf{E}_2| e^{-i(-kx\sin\theta'')} \\ &= \left[|\mathbf{E}_1|\cos(kx\sin\theta' + \phi) + |\mathbf{E}_2|\cos(kx\sin\theta'')\right] \\ &\quad - i\left[|\mathbf{E}_1|\sin(kx\sin\theta' + \phi) - |\mathbf{E}_2|\sin(kx\sin\theta'')\right].\end{aligned} \qquad [5\text{-}16]$$

The intensity can be derived as

$$\begin{aligned}I \propto |\mathbf{E}|^2 &= |\mathbf{E}_1 + \mathbf{E}_2|^2 \\ &= |\mathbf{E}_1|^2 + |\mathbf{E}_2|^2 + 2|\mathbf{E}_1||\mathbf{E}_2|\cos(kx\sin\theta' + kx\sin\theta'' + \phi).\end{aligned} \qquad [5\text{-}17]$$

Therefore, the corresponding pitch is

$$p_{tilt} = \frac{2\pi}{k\sin\theta' + k\sin\theta''} = \frac{\lambda}{n(\sin\theta' + \sin\theta'')}. \qquad [5\text{-}18]$$

For a laser pointing tilt angle δ, θ' tends to be larger than θ, but θ'' tends to be smaller than θ. For a small tilt angle δ, intuitively, we may think that $\sin\theta' + \sin\theta'' \approx 2\sin\theta$, hence a very small pitch change is expected. To describe the phenomenon quantitatively, let's define a length L over which the pitch number difference between the tilted case and non-tilted case is 1. L can be expressed as

$$L = \left(\frac{1}{p} - \frac{1}{p_{tilt}}\right)^{-1} = \frac{\lambda}{n(2\sin\theta - \sin\theta' - \sin\theta'')}. \qquad [5\text{-}19]$$

As illustrated in Figure 5.6, the fringe pattern from tilted beam is out of phase with that from the normal beam at the two ends of length L, where the resulted fringe contrast is the worst. If the laser energy is equally distributed between the normal direction and δ-tilt direction, the fringe contrast is zero at those locations. In reality, the contrast will depend on the laser pointing direction statistics. If the length of the desired image area is much smaller than L, the contrast loss due to laser pointing instability can be ignored. Therefore, L is characteristic of the useful image size that could be obtained in the case of laser pointing instability. Here, it is termed as Tilt Coherence Length.

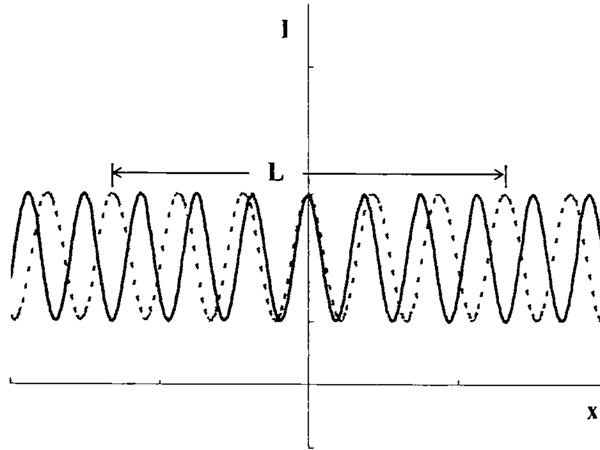

Figure 5.6 Illustration for interference fringe contrast loss due to fringe pitch change from tilted beam. The solid sinusoidal curve is from normal beam interference and the dashed sinusoidal curve is from tilted beam. Over a length of L, the solid curve has one more number of pitches than that of the dashed curve. At both ends of the length *L*, the contrast is the worst.

The tilt coherence length versus laser beam tilt angle is plotted in Figure 5.7. A grating pitch of $p = 600\,\text{nm}$, setup size of $D = 1\,\text{cm}$ and source wavelength of $\lambda = 193\,\text{nm}$ are used in the calculation. The plots show that the tilt coherence length decreases as the interference angle θ is increased to higher values. It indicates that beam tilt is more sensitive at higher θ values, which lies in our scope of interest. The degree of beam tilt which can be tolerated in our interferometric systems can be derived from the plots if it is the only factor that contributes to fringe contrast loss. In the context that the effective beam size in our setup is around 2~3 mm, a tilt coherence of 200 mm would yield negligible contrast loss. The corresponding tilt angle from the plot is 0.05° in the case of $\theta = 60°$ (dotted curve). This would allow us to establish minimum requirements for factors which contribute to beam tilt, such as laser pointing stability, mechanical setup vibration, environmental vibration, etc.

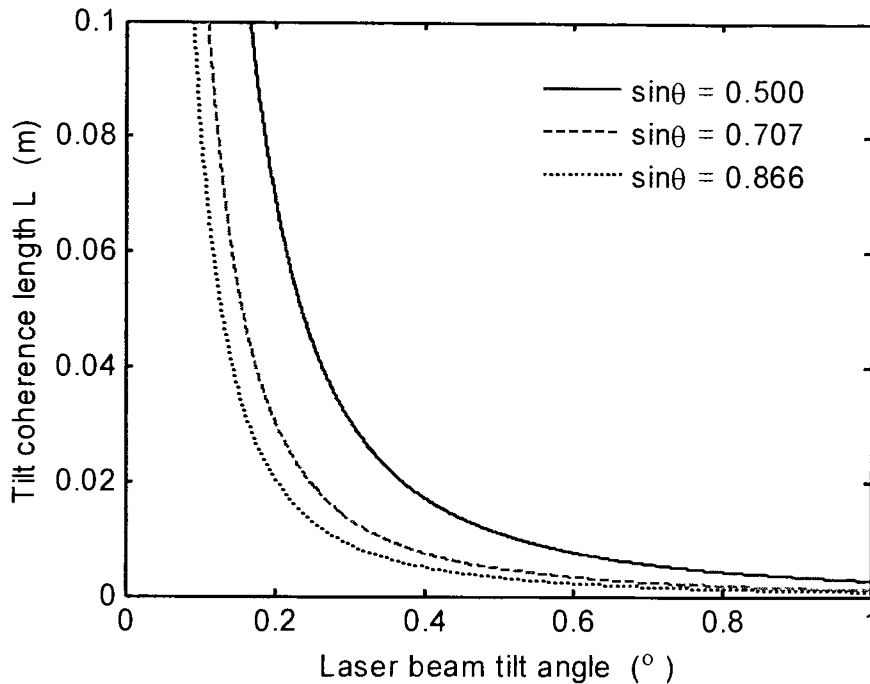

Figure 5.7 Tilt coherence length versus laser beam tilt angle. Grating pitch p = 600 nm, setup size D = 1 cm, wavelength λ = 193 nm. $\sin\theta$ =0.500 (solid curve); $\sin\theta$ = 0.707 (dashed curve); $\sin\theta$ = 0.866 (dotted curve).

The preceding analysis has been focused on one certain laser beam tilt angle. In practice, the laser beam tilt angle has a normal distribution, $P(\delta)$, where P is the normal distribution function. The previous has shown that ϕ is directly related to δ, so the distribution of ϕ can be expressed as $P(\delta(\phi))$. Equation [5-17] states that the interference fringe intensity is a function of location x, and tilt angle σ, $I(x, \phi)$. The resultant interference fringe is an average over the values ϕ, that is

$$I(x) = \int_{-\infty}^{+\infty} I(x,\phi)P(\delta(\phi))d\phi. \quad [5\text{-}20]$$

Substitution of Equation [5-17] gives

$$I(x) = \int_{-\infty}^{+\infty} \left[|\mathbf{E}_1|^2 + |\mathbf{E}_2|^2 + 2|\mathbf{E}_1||\mathbf{E}_2| \cos(kx \sin\theta' + kx \sin\theta'' + \phi) \right] P(\delta(\phi)) d\phi . \quad [5\text{-}21]$$

Assume that σ is very small, then

$$kx \sin\theta' + kx \sin\theta'' = 2kx \sin\theta . \quad [5\text{-}22]$$

Equation [5-21] can be rewritten as

$$I(x) = \int_{-\infty}^{+\infty} \left[|\mathbf{E}_1|^2 + |\mathbf{E}_2|^2 + 2|\mathbf{E}_1||\mathbf{E}_2| \cos(2kx \sin\theta + \phi) \right] P(\delta(\phi)) d\phi . \quad [5\text{-}23]$$

Since $P(\delta(\phi))$ is an even function, the above integral is a convolution, which can be simplified as

$$I(x) = \left\{ |\mathbf{E}_1|^2 + |\mathbf{E}_2|^2 + 2|\mathbf{E}_1||\mathbf{E}_2| \cos(u) \right\} \otimes P(\delta(u)) \quad [5\text{-}24]$$

where $u = 2kx \sin\theta$. Evaluation of the above convolution yields,

$$I(x) = |\mathbf{E}_1|^2 + |\mathbf{E}_2|^2 + 2\Im\{P(\delta(u))\}\Big|_{\frac{1}{2\pi}} |\mathbf{E}_1||\mathbf{E}_2| \cos(u) \quad [5\text{-}25]$$

where $\Im\{P(\delta(u))\}\Big|_{\frac{1}{2\pi}}$ is the Fourier transform of $P(\delta(u))$ evaluated at $\frac{1}{2\pi}$. The contrast of the fringe can be expressed as

$$\text{Contrast} = 2\Im\{P(\delta(u))\}\Big|_{\frac{1}{2\pi}} \frac{|\mathbf{E}_1||\mathbf{E}_2|}{|\mathbf{E}_1| + |\mathbf{E}_2|} . \quad [5\text{-}26]$$

If the two beams are equal in intensity, the contrast can be reduced as

$$\text{Contrast} = \Im\{P(\delta(u))\}\Big|_{\frac{1}{2\pi}} \quad [5\text{-}27]$$

If the standard deviation σ of beam direction fluctuation is known, that is, P(δ) is known, it allows us to numerically evaluate the fringe contrast in the absence of laser beam direction fluctuation. An example is shown in Figure 5.8.

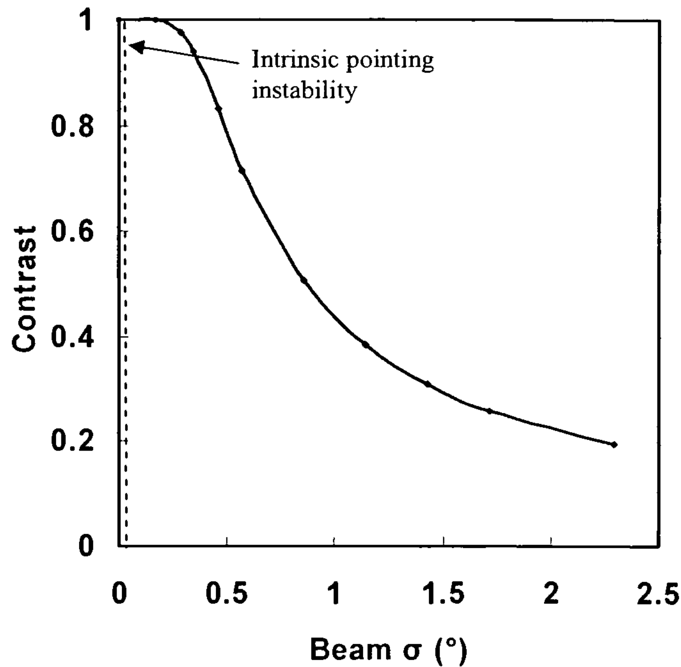

Figure 5.8 Interference fringe contrast versus the standard deviation σ of beam direction fluctuation. D=0.01m, θ=45°, λ=193nm, grating pitch=600nm, TE polarization.

In this figure, the fringe contrast is plotted versus the standard deviation σ of beam direction fluctuation. Configuration size D=0.01m, interference angle θ=45°, wavelength λ=193nm and grating pitch=600nm are used in the calculation. The simulation results show that the contrast drops rapidly at σ=0.5°. The excimer laser used for this research has an intrinsic σ of about 20μ radians, the effect of which on interference fringe contrast can be ignored, as shown in Figure 5.8. In addition to intrinsic laser pointing instability, other factors such mechanical resonant vibration, environmental vibration, etc. might bring the standard deviation σ of the beam direction fluctuation to a higher value. Under

those circumstances, the contrast loss of the interference fringe is well described by the curve in Figure 5-8.

5.3 Temporal Coherence Considerations

Due to the lack of a well-defined ground state of excimers for the energy level transition that defines the laser wavelength, the free-run excimer laser's spectral line width is about 0.5nm, which means only a few square nanometers of image with high contrast can be obtained. To be used for interferometric lithography, some wavelength dispersive optical elements such as diffraction gratings, prisms and/or etalons are often introduced in the resonator to narrow the spectral line width. Even so, the obtainable temporal coherence length is still just a few millimeters. However, a correctly configured setup could ease the requirements on temporal coherence length. The following analysis help explains how the setup configuration is related to the "beating frequency", assuming there are two monochromic wavelengths which generates beats in the interference fringe, on the wafer plane. A lower beating frequency means larger useful image area.

The interference fringe pitch is determined by the source wavelength λ, the refractive index of the media n and the oblique angle θ

$$p = \frac{\lambda}{2n\sin\theta}. \qquad [5\text{-}28]$$

The oblique angle θ is related to the first order diffraction angle α and mirror tilt angle β (as shown in Figure 4.1) as

$$\theta = \alpha + 2\beta. \qquad [5\text{-}29]$$

The sin of the first order diffraction angle α is

$$\sin\alpha = \frac{\lambda}{p_g}. \qquad [5\text{-}30]$$

where p_g is the pitch of the phase grating. Therefore, the fringe pitch can be expressed via simple mathematic manipulation as

$$\begin{aligned} p &= \frac{\lambda}{2n\sin(\alpha+2\beta)} \\ &= \frac{\lambda}{2n[\sin\alpha\cos(2\beta)+\cos\alpha\sin(2\beta)]} \end{aligned} \qquad [5\text{-}31]$$

$$p = \left\{2n\left[\cos(2\beta)\frac{1}{p_g} + \sin(2\beta)\sqrt{\frac{1}{\lambda^2} - \frac{1}{{p_g}^2}}\right]\right\}^{-1}. \qquad [5\text{-}32]$$

The above equation indicates that the system is achromatic (wavelength dependence is suppressed) when the mirror tilt angle β is zero, *i.e.* $\alpha = \theta$. Albeit the ideal achromatic configuration can alleviate source line-width requirement, it sacrifices the set-up's flexibility of implementing multiple oblique angles with a single phase shifting grating, a cost-effective and time-saving practice. For non-ideal configurations, the source line-width dependence as a function of tilt angle β can be analyzed. Suppose there are two wavelengths in the source equal in strength, $\lambda_1 \approx \lambda_2$, which produce cosinusoidal interference fringes , respectively as (assuming TE polarization)

$$I_1(x) = 1 + \cos\left(\frac{2\pi x}{p_1}\right) \qquad [5\text{-}33]$$

$$I_2(x) = 1 + \cos\left(\frac{2\pi x}{p_2}\right) \qquad [5\text{-}34]$$

where p_1 and p_2 are the corresponding pitches. The summation is

$$\begin{aligned} I(x) &= I_1(x) + I_2(x) \\ &= 2 + 2\cos\left[\pi x\left(\frac{1}{p_1} - \frac{1}{p_2}\right)\right]\cos\left[\pi x\left(\frac{1}{p_1} + \frac{1}{p_2}\right)\right]. \end{aligned} \qquad [5\text{-}35]$$

The first cosinusoidal term describes the beating behavior. The beat period L can be expressed as

$$L = \left(\frac{1}{p_1} - \frac{1}{p_2}\right)^{-1} \qquad [5\text{-}36]$$

Substitution of the pitch Equation [5-32] will give

$$\begin{aligned} L &= \left\{2n\sin(2\beta)\left[\sqrt{\frac{1}{\lambda_1^{\,2}} - \frac{1}{p_g^{\,2}}} - \sqrt{\frac{1}{\lambda_2^{\,2}} - \frac{1}{p_g^{\,2}}}\right]\right\}^{-1} \\ &= \left\{2n\sin(2\beta)\left[\frac{1}{\lambda_1}\sqrt{1 - \frac{\lambda_1^{\,2}}{p_g^{\,2}}} - \frac{1}{\lambda_2}\sqrt{1 - \frac{\lambda_2^{\,2}}{p_g^{\,2}}}\right]\right\}^{-1}. \end{aligned} \qquad [5\text{-}37]$$

Since, $\lambda_1 \approx \lambda_2$, the above expression can be simplified as

$$\begin{aligned} L &\approx \left\{2n\sin(2\beta)\sqrt{1 - \frac{\lambda_1^{\,2}}{p_g^{\,2}}}\left[\frac{1}{\lambda_1} - \frac{1}{\lambda_2}\right]\right\}^{-1} \\ &\approx \left[2n\sin(2\beta)\cos\alpha\right]^{-1}\frac{\lambda^2}{\Delta\lambda} \end{aligned}$$

$$L = \left[2n\sin(2\beta)\cos\alpha\right]^{-1} l_c. \qquad [5\text{-}38]$$

where $l_c = \dfrac{\lambda^2}{\Delta\lambda}$ is the temporal coherence length. Subsequently, the temporal coherence length is related to beat period (L) as

$$l_c = (L)[2n\sin(2\beta)\cos\alpha]. \qquad [5\text{-}39]$$

In Figure 5.9, the normalized beating frequency (*1/L*) is plotted versus α and θ. Along the $\alpha = \theta$ diagonal, there is a beating frequency valley. Set-up configured close to the valley will suffer no (when $\alpha = \theta$) or less chromatic effects, alleviating source line-width requirement. Current generation of line-narrowed excimer lasers usually carry a temporal coherence l_c of 2-15 millimeters. A set-up configured close to being achromatic is very necessary to enhance fringe contrast and ease problems of unmatched beam arms if the temporal coherence length is not long enough.

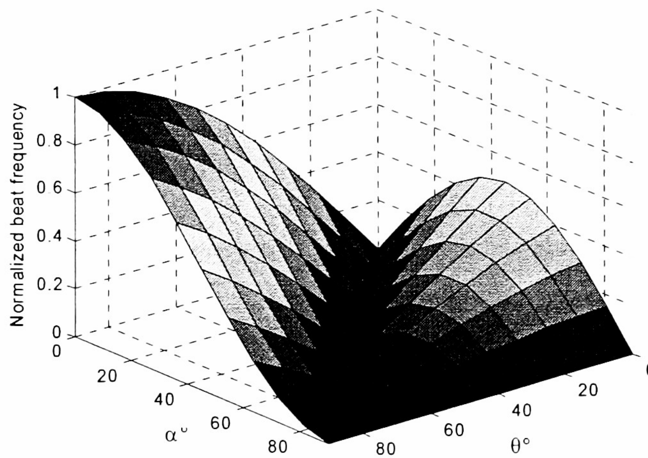

Figure 5.9 Beat frequency (1/L) normalized to $2n/\Delta l_c$ versus the first diffraction angle α and oblique angle θ. Along the $\alpha = \theta$ diagonal is the low beat frequency valley.

From Equation [5-35], it is noticed that the contrast of the interference fringe is

$$\text{Contrast} = \left|\cos\left[\pi x\left(\frac{1}{p_1} - \frac{1}{p_2}\right)\right]\right| = \left|\cos\left(\frac{\pi x}{L}\right)\right|. \qquad [5\text{-}40]$$

Equation [5-40] indicates that the interference fringe contrast is a function of location. The contrast is highest in the center (x=0) and decreases away from center. If the setup is not properly configured, the useful image area (area where the fringe contrast meets a certain requirement) could be very small

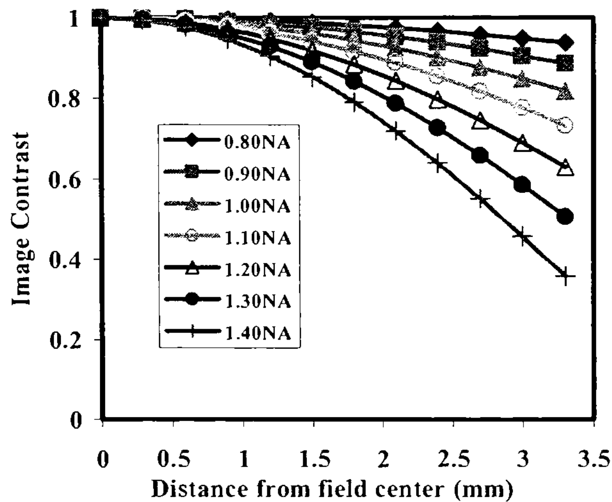

Figure 5.10 Interference contrast versus the distance from field center at various NA values. The source has a wavelength of 193nm and a temporal coherence length of 18 mm. The grating pitch is 600 nm.

In our setup, the source has a wavelength of 193 nm and a temporal coherence length of 18 mm. The grating pitch is 600 nm, and the imaging media is fused silica. In Figure 5.10, the interference fringe contrast (assuming TE polarization) is plotted versus the distance from image field center at various NA values. As NA value increases, the

contrast decreases at a certain location. The plots allow us to estimate the size of the useful imaging area at a certain contrast requirement. For example, at NA=1.40, the contrast within an imaging area with radius of 1 mm is higher than 90%.

5.4 Spatial Coherence Considerations

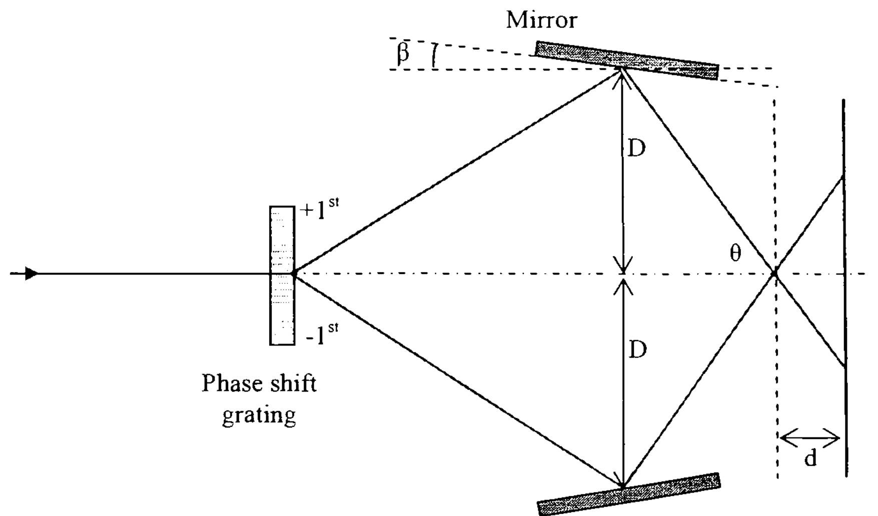

Figure 5.11 Illustration of a wafer with a displacement of d from the "focal plane" The two beams are displaced by 2dsinθ in the transverse direction of the beam.

If the wafer plane is placed where the centers of the beams meet, then the two beams overlap completely with each other. Since the two beams originate from the same laser beam, and they experience the same set of optical components (i.e., the diffraction grating and the turning mirror), theoretically, an infinitesimal spatial coherence length is required to afford a high contrast fringe. However, if the wafer is displaced by a distance d relative to this position, the two beams are displaced by $2d\sin\theta$ in the transverse direction of the beam (Figure 5.10). Now, a spatial coherence length much longer than $2d\sin\theta$ is necessary to afford a high contrast interference fringe. Spatial coherence length

of current generation line-narrowed excimer lasers is less than 2 millimeters. Beam expansion of 5-10 times brings the effective spatial coherence length at interferometric plane to about 10 mm. As a result, two-beam overlapping errors within a fraction of a millimeter are tolerable.

5.5 Summary

This chapter discussed the special optical characteristics of the interferometric lithography setup employed for interferometric immersion lithography.

Using geometrical ray tracing technique and basic interference theory, the effects of beam pointing instability on the contrast of interference fringe were analyzed for a two-beam interferometric lithography setup described in this dissertation. The established relationship between beam tilt angle and interference fringe displacement allows the evaluation of the fringe contrast if the beam pointing direction is not stable during the exposure. The analysis shows that a setup configuration with smaller size is more tolerant with beam pointing instability. It also shows that the system is more tolerant with beam pointing instability at higher interference angles. For a beam pointing instability with random distribution, it has been shown that, the resulted fringe contrast is directly proportional to the Fourier transform of the beam pointing direction distribution evaluated at $\frac{1}{2\pi}$. A numerical simulation example was given for a beam pointing direction with normal distribution. The example shows that a beam pointing direction of Gaussian distribution with standard deviation less than 0.25 degree does not noticeably affect the contrast of the resulted interference fringe. The analysis introduced in this chapter may be applied to evaluate any factors contributing to beam direction fluctuation, such as

intrinsic laser pointing instability, mechanical resonant vibration, environmental vibration, etc.

Moreover, the setup's dependence on the source's temporal coherence and spatial coherence were analyzed. It has been shown that a properly configured setup could ease the stringent temporal and spatial coherence requirements on the source.

CHAPTER 6

EXPERIMENTAL INVESTIGATION OF HYPER-NA EFFECTS IN PHOTORESIST

6.1 Introduction

This chapter describes the experiments used to verify the hyper-NA effects which have been numerically analyzed in Chapter 3. The two-beam interferometric setup represented in Chapter 4 is employed to perform the experimental verification. As described previously, the state of illumination polarization starts to play an important role in two-beam interference at high NA values. That is, TE polarization tends to have a high contrast interferometric fringe while TM polarization tends to have a degraded fringe contrast. In addition, they behave very differently in substrate reflection, which results in distinct profiles of light distribution within the resist film. In order to study those effects, TE and TM illumination are used to explore the dependence of light distribution within the resist film on polarization at various hyper-NA values. The experiments concentrate on NA values higher than 1.0 since immersion imaging techniques enable this, and polarization effects are well pronounced at these NA values. A side-develop technique is used to record the light intensity contours within the resist film. At hyper-NA's, the optimal BARC parameters are a function of NA. In theory, a single layer BARC is only optimized for a single NA. To accommodate a broad NA range, multilayer BARC's are necessary. As part of the work of this chapter, the performance of single layer BARC and

dual layer BARC are evaluated for various NA values. The experimental results are compared with the numerical predictions.

6.2 Experimental Methods

The objective of the experiments is to observe the light density distribution within the resist film so that the experimental results can be compared with the numerical predictions, with the emphasis on the imaging behavior difference between TE and TM illumination. Assume that the simple threshold model (in which the resist regions where the exposure exceeds a threshold are removed during development) is valid, the developed resist profile is a natural representation of one contour of the light intensity distribution within the resist film. Therefore, SEM cross-sectioning technique will allow us to obverse the image distribution contours. In order for us to observe at least a few standing wave nodes of substrate reflection, the thickness of the resist film should be a few times larger than the pitch of the interference fringe. However, some resist structures can not be preserved during the development process due to pattern collapse. The situation becomes worse when the image detail structures are within a dimensional regime of a few nanometers. To prevent the developed resist pattern from collapsing or being distorted during the development process, an experimental technique from Flagello et al's work[57] is adopted. In this technique, the resist is coated with a non-developable topcoat. The resist is developed from the cleft cross-section. The technique is illustrated in Figure 6.1. A wafer coated with BARC, resist and a non-developable top coat layer is first exposed with two interfering beams at a desired NA. The wafer is cleaved in half across the exposed area perpendicular to the line pattern direction, and then it is

developed from the cross-section. Examination of the cross-section by SEM is followed. A thin layer of gold film (2 nm in thickness) is sputtered on the sample for SEM inspection. The SEM inspection is performed on an ARAMY 1830 SEM. The observed resist profile is one contour of the light intensity distribution within the resist film.

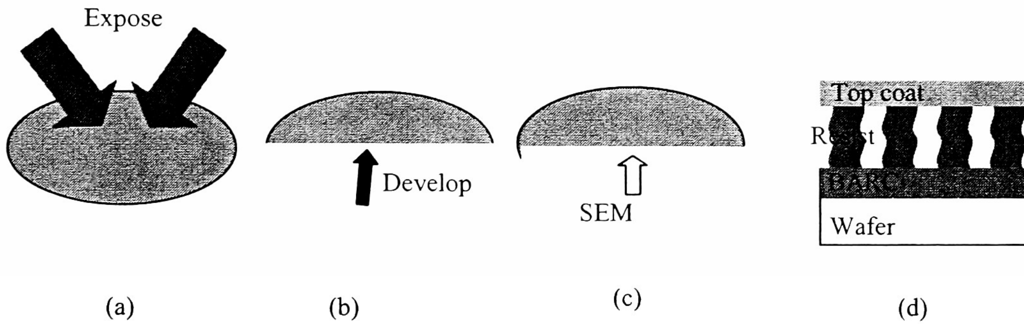

(a) (b) (c) (d)

Figure 6.1 Characterization of resist line cross-sections. (a) A wafer coated with BARC, resist and a non-developable top coat layer is exposed with two interfering beams at a desired NA; (b) The wafer is cleaved in half across the exposed area perpendicular to the fringe lines, then it is developed from the cross-section; (c) Examination of the cross-section by SEM; (d) Schematic illustration of the resist cross-sections with standing-waves.

Bare silicon wafers with (1, 0, 0) crystal orientation are used as substrates since that they can be cleaved easily in orthogonal directions. At a wavelength of 193 nm, the refractive index of the silicon substrate is 0.87-2.76i. A Brewer Science coater is used to spin coat the films. Baking is performed on a Brewer Science hot plate. The exposed wafer is developed manually in a Shipley CD 26 Developer. A typical example of process parameters is listed in Table 6.1. Changes to those parameters will be noted where appropriate. The optical constants and thickness of the resist, top coat, BARC are characterized using a Woollam VASE Ellipsometer.[66,67] The tool measures the change in polarization state of light reflected from the surface of a sample. Based on the Fresnel equations along with an assumed model, regression analysis is used to extract the desired

optical constants as well as film thickness. The optical constants of some materials are listed in Table 6.2.

Table 6.1 A set of resist processing parameters

Process parameters	Process Conditions
BARC AR29A-8, post apply bake (PAB)	200°C, 90 seconds
Resist ILP012, post apply bake (PAB)	95°C, 90 seconds
Top coat TSP3A, post apply bake (PAB)	90°C, 60 seconds
Resist ILP012, post exposure bake (PEB)	115°C, 60 seconds
Shipley CD-26, Develop	60 seconds
DI water, rinse	60 seconds

Table 6.2 Refractive indices of some materials at 193-nm

Materials	Refractive index
AR29A-8 (BARC)	1.82-0.34i
AZ-KrF17-100 (BARC)	1.70-0.10i
AR46 (BARC)	1.76-0.64i
ILP012 (resist)	1.71-0.039i
XP1020 (resist)	1.69-0.025i
TSP3A (top coat)	1.41

6.3 Experimental Results and Discussion

The side develop technique described in the previous section is an effective way to preserve the detailed resist structures formed from development. A comparison between this technique and the normal develop technique, as shown in Figure 6.2, is very convincible. The SEM photography on the left does not have a non-developable top coat during development. Due to pattern collapse, the distortion of the resist structures makes it impossible to represent the image distribution with the resist profile. The one on the right has a non-developable top coat on the resist. After it is cleaved, it is developed in the developer. The developer attacks the resist from the cross-section. Since both interfaces of the resist film are anchored, and the depth of development is also limited, the resist profile can be preserved very well, as is evident from the SEM photography on the right in Figure 6.2.

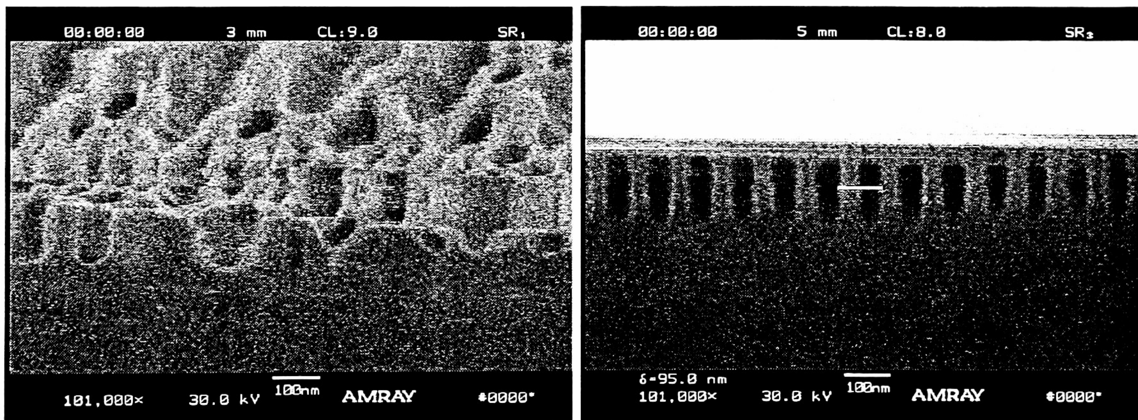

Figure 6.2 Illustration for the effectiveness of side develop technique. The SEM photography on the left did not have a non-developable top coat during development. The one on the right had a non-developable top coat during development.

6.3.1 Polarization Effects in Photoresist at Hyper-NA

The theoretical simulations analyzed in Chapter 3 have shown that the polarization effects on imaging in the photoresist are well pronounced in the presence of substrate reflection. To explore the imaging behavior distinction between TE and TM polarized illumination experimentally, a resist assembly listed in Table 6.3 is used. The resist is coated on a bare silicon substrate directly with a thickness of 170 nm. A 40 nm non-developable topcoat is coated on the top of the resist film. Two-beam interference at 1.05NA with TE and TM polarization is used to expose the resist. With a resist thickness of 170nm, two and a half reflection standing wave nodes could be observed. The resultant SEM cross-sectional photographs for TE polarization at various exposure times are shown in Figure 6.3. The expose time is increased from photography (a) to (c). The simulated light intensity distribution within the resist layer for 1.05NA using TE polarization is shown in Figure 6.3 (d). The iso-exposure contours in the figure agree well with the SEM cross-sectional photographs. The contour features are elliptical in shape. The measured pitch is 92 nm, which corresponds to 1.05NA. At high exposure times, the "linkages" connecting the features are eroded away, and the patterns start collapsing.

Table 6.3 Resist Film stack for polarization study

Layer
Top coat, N_1=1.414, d_1=40 nm
Resist, N_2=1.71-0.039i, d_2=170 nm
Substrate N_{sub}=0.87-2.76i

Processing: resist, 115°C/60s; Top coat, 90°C/60s; PEB, 115°C/60s; Develop, 30s in CD26 (1:10).

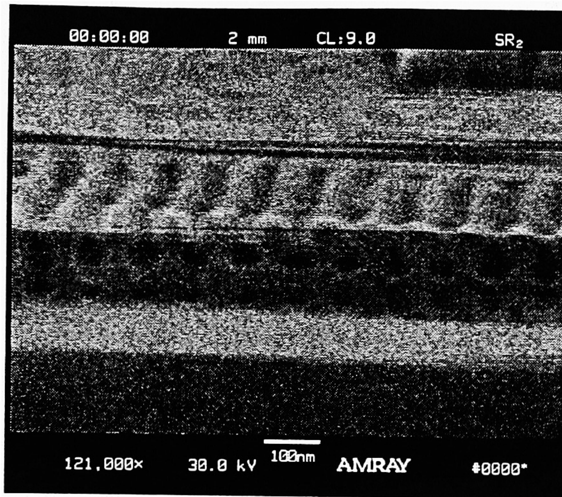

(a)

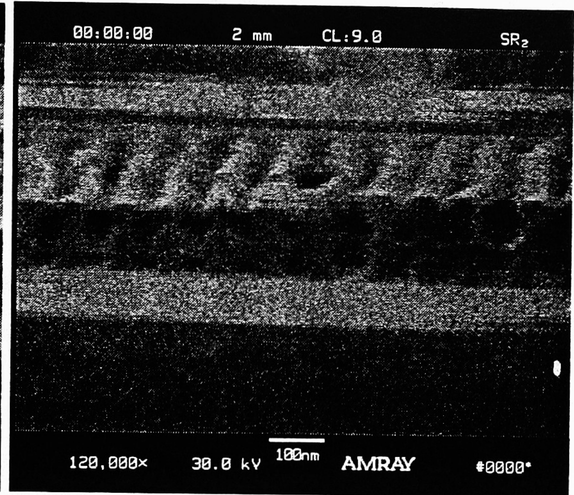

(b)

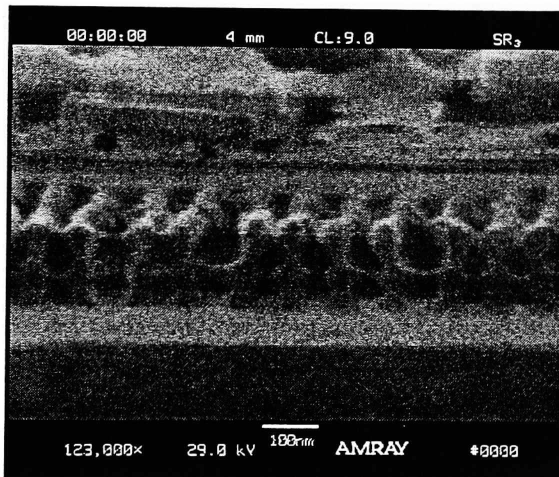

(c)

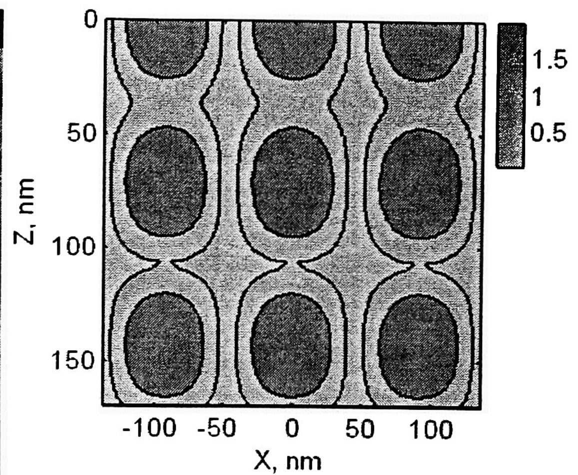

(d)

Figure 6.3 SEM photographs and simulation results for 1.05NA, TE polarization using resist assembly in Table 6.3. (a)-(c), SEM cross sections with increasing dose from (a) to (c); (d), Simulated light intensity distribution within the resist layer for 1.05NA using TE polarization.

The SEM cross-sectional photographs for TM polarization at various exposure times are shown in Figure 6.4. The expose time is increased from photograph (a) to (c). The simulated light intensity distribution within the resist layer for 1.05NA using TM polarization is shown in Figure 6.4 (d). The measured pitch is 92 nm, which corresponds to 1.05NA. Assume that the simple threshold model is valid, then the SEM cross-sectional view should look like the contour features shown in Figure 6.4 (d). However, experimental result is much more complex. In Figure 6.4 (a), there appears only one row of holes at the bottom of the resist film. It corresponds to the bottom row of standing wave node in Figure 6.4 (d). As the exposure time is increased, a second row of holes appear in the middle of the resist film, corresponding to the standing wave node at thickness around 75 nm in Figure 6.4 (d). When the exposure time is increased further, the top part of the resist starts being eroded away, without showing the simulated fine resist structures. Apparently, the simple threshold model failed to explain these observations. Many factors might have contributed to this. Careful examination of the simulation results can lead to a reasonable explanation. It is noticed in Chapter 3 that, for TM polarization, the interference fringe contrast varies through the depth of the resist. Using the simulation results in Figure 6.4 (d), the fringe contrast is plotted versus resist thickness Z, as shown in Figure 6.5. A negative value is given to the contrast as the intensity in the anti-nodal position exceeds that of the nodal position. The contrast has the highest value at Z=150 nm, followed by Z=75 nm, Z= 10 nm. This is the same order at which the rows of holes appear in the SEM photography. Evidently, it can be argued that the resist speed point (the minimum exposure that starts to develop the resist) is lower at higher interference fringe contrast.

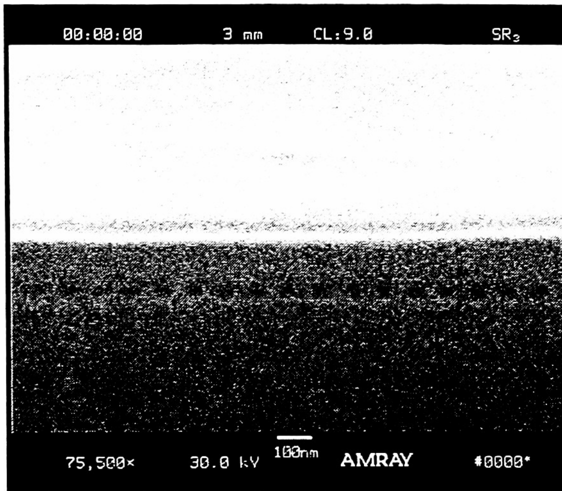

(a)

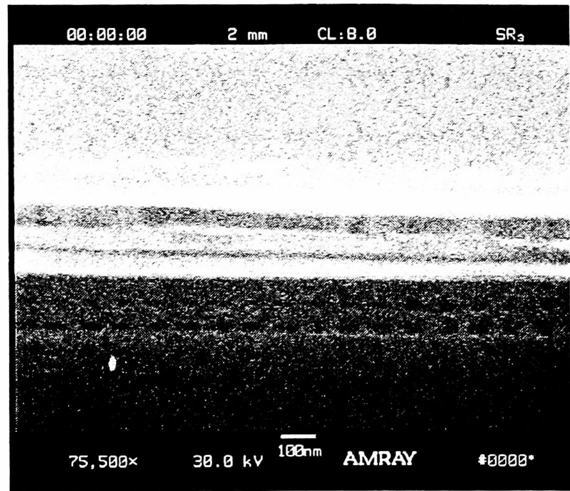

(b)

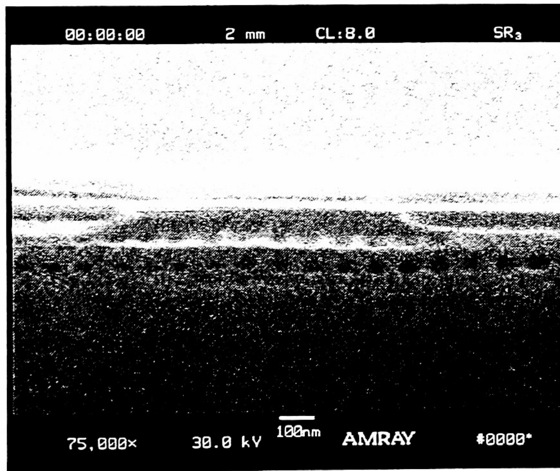

(c)

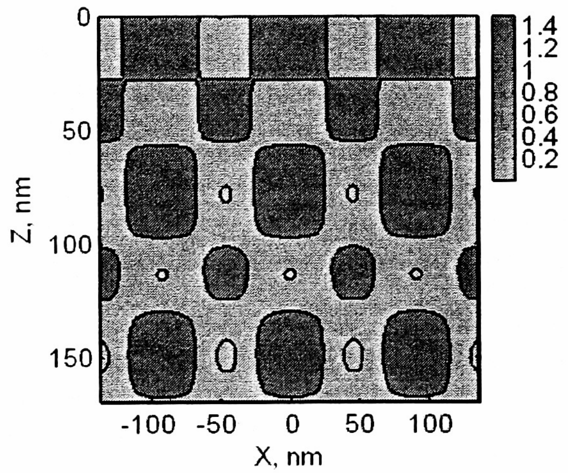

(d)

Figure 6.4 SEM photographs and simulation results for 1.05NA, TM polarization using resist assembly in Table 6.3. (a)-(c), SEM cross sections with increasing dose from (a) to (c). (d) Simulated light intensity distribution within the resist layer for 1.05NA using TM polarization.

The standing wave node features at Z=10 nm did not show up in the SEM photographs since it is highly likely that no available linkages exist to support the resist structures at that speed point. The standing wave node features due to the z component of the TM field appears at Z=40nm, 100nm. They did not appear in the SEM photograph either simply because that they are too small to be resolved by the resist.

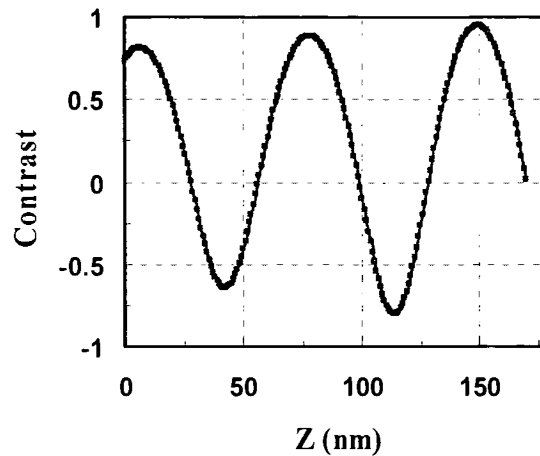

Figure 6.5 Fringe contrast versus resist thickness for the simulation results shown in Figure 6.4 (d).

6.3.2 BARC Optimization for Hyper-NA Imaging

The previous section has shown that the reflection from the substrate could form standing waves within the resist film. Those standing waves cause fluctuations in line width, exposure dose etc. It needs to be suppressed. To do so, a commonly employed technique is to coat on the substrate a layer of thin film (called bottom anti-reflection coating, BARC), which reduces reflection from the substrate partially by absorbing the

incident light, partially by the destructive interference of the light reflected from the top interface of the BARC and the light reflected from the substrate. The underlying optics has been reviewed in Chapter 3. It has been shown that the BARC can only be optimized for a certain incident angle and requires a stringent thickness control. In practice, the utilization of BARC is limited by the presence of multiple incident angles. For low NA imaging, usually a single layer BARC will be able to reduce the reflection to below 1% at all angles due to the relative narrow band of incident angles. However, it will not be sufficient to use a single layer BARC in the context of hyper numerical aperture imaging, where a broad range of incident angles is expected. In this case, a multi-layer BARC is necessary to suppress reflection from all incident angles. Figure 6.6 shows the simulated reflectance of TE polarization for two single-layer BARC's at different thickness and a bi-layer BARC. The substrate has refractive index of 0.87-2.76i, and the resist has a refractive index of 1.71-0.039i. The simulation was carried out using the ILsim simulator. The single layer BARC at 77 nm thickness can reduce the reflection at low NA values but the reflection increases significantly above NA=1.0. The thickness can be tuned to 39nm so that the reflection minimum is at about 1.3 NA but then the reflectance at low NA values increases. Instead, the bi-layer can suppress the reflection up to NA=1.50 while the reflectance at lower NA values are still relatively low. Bi-layer BARC is the simplest form of multi-layer BARC's. BARC's with more layers will do a better job. In theory, an index gradient BARC (infinite number of layers) is able to suppress the reflectance to zero for all incident angles ranging from 0 to 90°. In practice, however, we would like to use as few layers as possible in order to reduce processing cost.

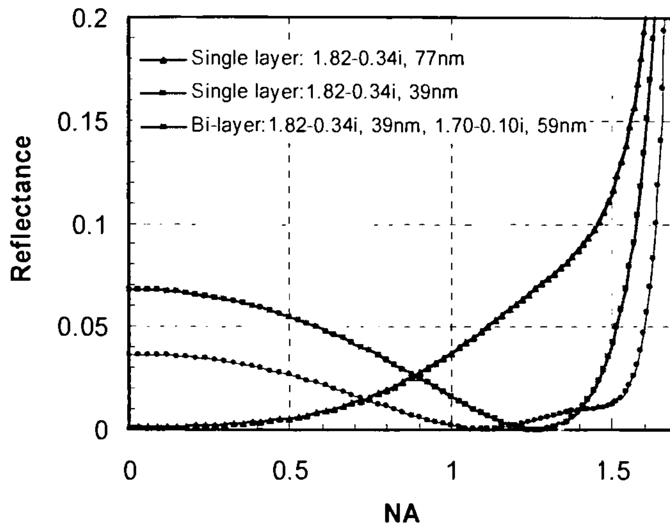

Figure 6.6 Reflection as a function of incident angle of TE polarization for two single layer BARC's and a bi-layer BARC. Substrate, 0.87-2.76i; resist 1.71-0.039i.

The bi-layer BARC from Figure 6.6 was used for two-beam interferometric lithography at 1.05NA and 1.30NA with TE polarization. The film assembly is listed in Table 6.4, together with the processing conditions. The top-coat is non-developable so that the side develop technique can be used to inspect the standing wave effects in the resist line patterns. The resultant SEM cross-sectional photograph is shown in Figure 6.7. The photograph shows that the resist lines start collapsing at 1.05NA due to a high aspect ratio of 3.8. At 1.30NA, the aspect ratio is 4.6 and there are much more collapse. However, no noticeable standing waves effects have been observed. It was experimentally proven that the bi-layer BARC worked for both 1.05NA and 1.30NA. From the simulation results in Figure 6.6, it is reasonable to deduce that the bi-layer BARC will work a wide range of NA values.

Table 6.4 Resist film stack for 1.05NA and 1.30NA

Top coat, N_l=1.414, d_l=40 nm
Resist, N_2=1.71-0.039i, d_2=170 nm
BARC1, N=1.70-0.10i, 59 nm
BARC2, N=1.82-0.34i, 39 nm
Substrate N_{sub}=0.87-2.76i

Processing: BARC, 200°C/90s; resist, 95°C/90s; Top coat, 90°C/60s; PEB, 115°C/90s; Develop, 60s in CD26 (1:10).

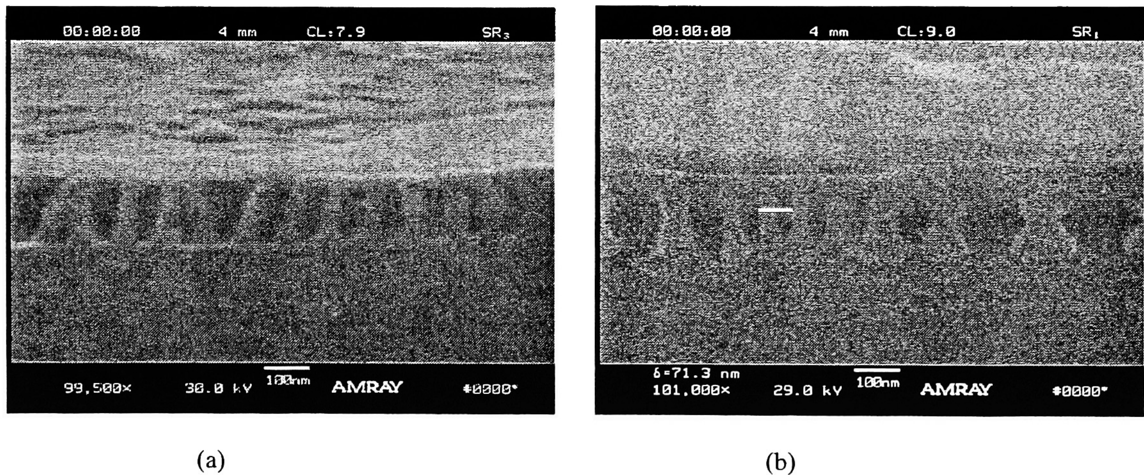

(a) (b)

Figure 6.7 SEM photographs of two-beam interferometric lithography with TE polarization using the resist film assembly in Table 6.6. (a) 1.05NA; (b) 1.30NA.

6.3.3 Immersion Interferometric Lithography Examples

The studies on polarization effects and BARC optimization have provided us with a good understanding of the optics of hyper-NA lithography. The knowledge helps us with printing small features using immersion technique. A list of immersion interferometric lithography examples for 2-beam interferometric lithography at various NA is shown in Figures 6.8 through 6.13.

The optical parameters for the resist assembly used for 0.7-1.05NA are listed in Table 6.5, along with the processing conditions. The substrate is (1 0 0) bare silicon wafer. The BARC material is AR29A-8 from Brewer Science. The photoresist material is XP1020B from Rohm & Haas and the top coat is TSP3A from TOK. The top coat layer is used to isolate acid contaminations from the environment. The thickness of the photoresist film is chosen so that the resultant aspect ratio of resist pattern is about 2:1. The BARC layer of 95 nm thickness is able to reduce substrate reflection to below 1.5% for 0.7NA through 1.05NA.

Table 6.5 Resist film stack used for 0.7-1.05NA

Layer
Top coat, N_1=1.414, d_1=40 nm
Resist, N_2=1.69-0.025i, d_2=80-150 nm
BARC, N_3=1.82-0.34i, 95 nm
Substrate N_{sub}=0.87-2.76i

Processing: BARC, 200°C/90s; resist, 120°C/90s; Top coat, 90°C/60s; PEB, 120°C/60s; Develop, 60s in CD26.

Figure 6.8 (a) shows the simulation result for light intensity distribution within the photo resist film at 0.70NA (69 nm half pitch) with TE polarization. The corresponding SEM cross-sectional photograph of the experimental result is shown in Figure 6.8 (b). The simulation result show that there are some residual standing wave effects due to reflection from the substrate but resist pattern with straight profile side walls is possible if the threshold of the photoresist is set to the intensity contours with relatively straight lines. This has been confirmed by the cross-sectional photography in figure 6.8(b), where resist pattern with straight side walls were observed.

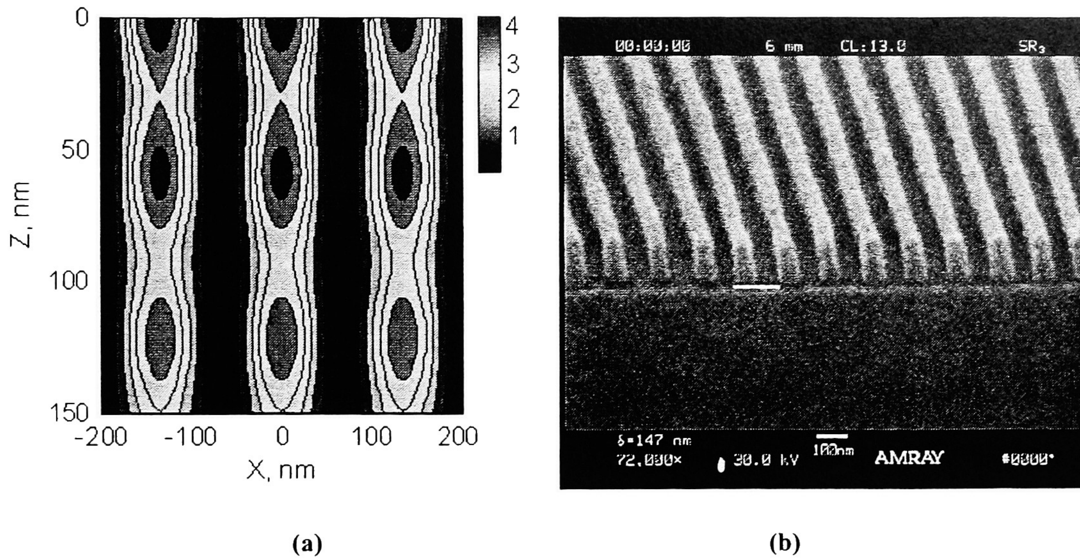

(a) **(b)**

Figure 6.8 Numerical calculation and SEM cross-sectional photograph of two-beam interferometric lithography with TE polarization at 0.7NA, 69 nm half pitch. (a) Numerical Calculation; (b) SEM cross-sectional photograph.

Figure 6.9 (a) shows the simulation result for light intensity distribution within the resist film at 0.80NA (60 nm half pitch) with TE polarization. The corresponding SEM cross-sectional photograph of the experimental result is shown in Figure 6.9 (b). The results are similar to the case of 0.70NA.

The 0.90NA (53 nm half pitch) results are show in Figure 6.10. In the SEM cross-sectional photograph, the presence of noticeable resist line edge roughness is readily seen. The origin of the observed line edge roughness is not from the standing wave effects since the simulation shows that the standing wave effects are less severe than those of 0.70NA and 0.80NA. It should be mentioned that a flat fused silica plate is used for immersion setup for NA<1.0. Therefore, at 0.9NA, the incident angle is 65°, which makes the alignment difficult. The poor alignment might have contributed to the degrading of image quality.

A fused silica half ball it used to investigate imaging at NA's higher than 1.0. HPLC water (n=1.437 at a wavelength of 193 nm) is used as the immersion fluid. The 1.05NA (45 nm half pitch) simulation and experimental results are shown in Figure 6.11. Imaging above 1.0NA is the purpose of immersion technique to increase resolution. The

decent SEM cross-sectional photograph indicates that the concept of "immersion imaging" is feasible.

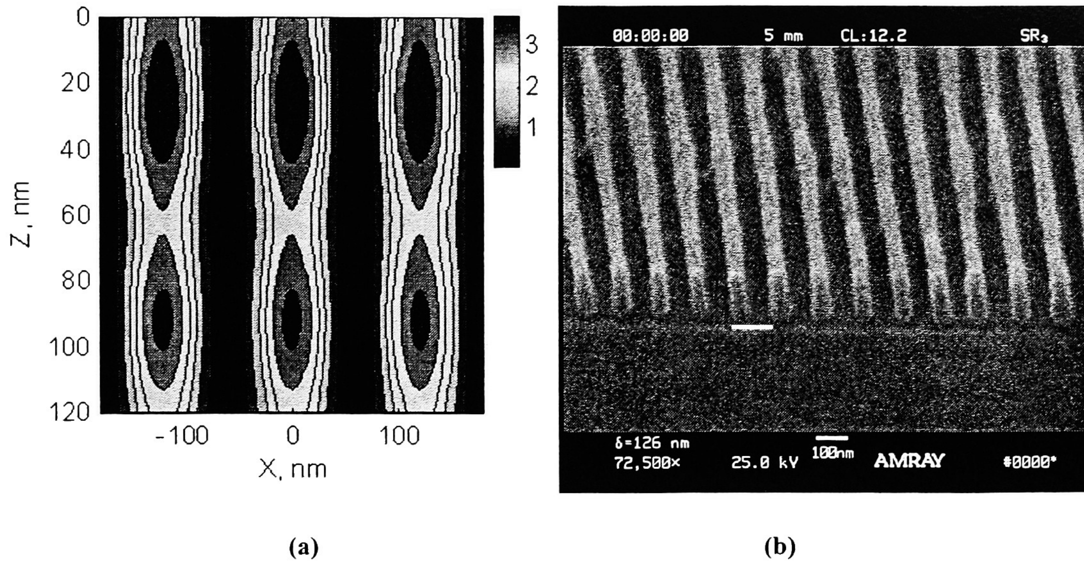

(a) (b)

Figure 6.9 Numerical calculation and SEM cross-sectional photograph of two-beam interferometric lithography with TE polarization at 0.8NA, 60 nm half pitch. (a) Numerical Calculation; (b) SEM cross-sectional photograph.

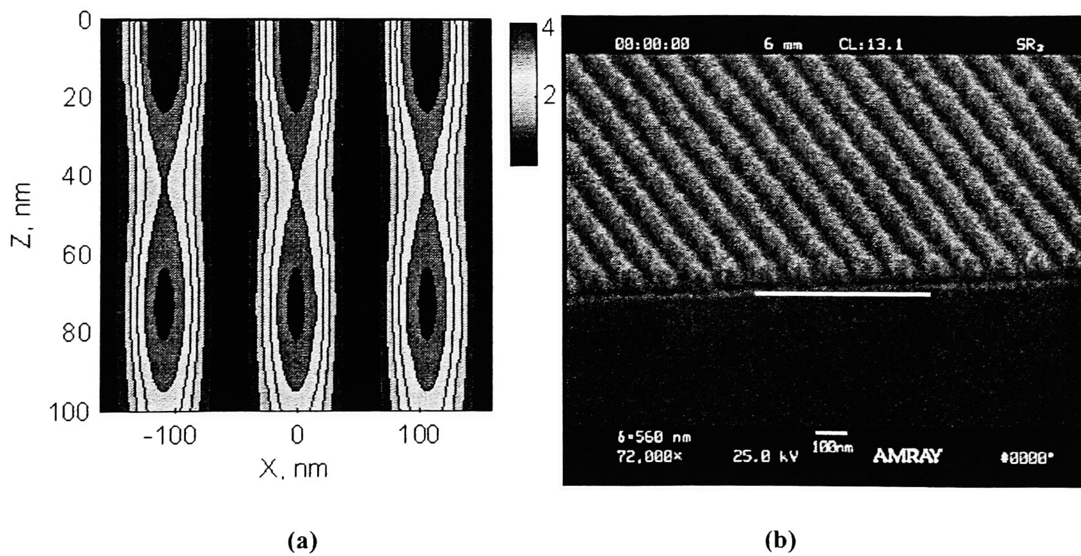

(a) (b)

Figure 6.10 Numerical calculation and SEM cross-sectional photograph of two-beam interferometric lithography with TE polarization at 0.9NA, 53nm half pitch. (a) Numerical Calculation; (b) SEM cross-sectional photograph.

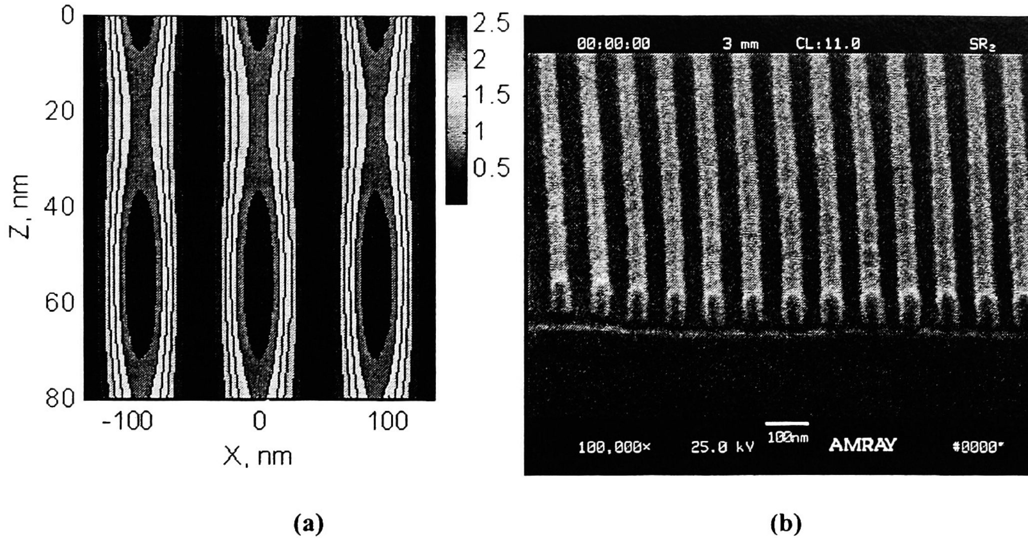

(a) **(b)**

Figure 6.11 Numerical calculation and SEM cross-sectional photograph of two-beam interferometric lithography with TE polarization at 1.05NA, 45 nm half pitch. (a) Numerical Calculation; (b) SEM cross-sectional photograph.

The resist film stack in Table 6.5 works very well for 0.7-1.05NA. For higher NA values imaging, we need to modify the film assembly. At higher NA's, the optimized BARC parameters are very sensitive to NA values, as has been discussed in Chapter 3. The parameters of the resist film stack, as well as the processing conditions, for 1.35NA and 1.50NA are listed in Table 6.6. The BARC (39nm) is optimized for 1.35NA, reducing reflectance to 0.0004%, but has a 2% reflectance at 1.5NA. The photoresist material is ILP012 from TOK.

Table 6.6 Resist film stack used for 1.35NA and 1.5NA

Layer
Top coat, N_1=1.414, d_1=40 nm
Resist, N_2=1.71-0.039i, d_2=78 nm
BARC, N_3=1.82-0.34i, 39 nm
Substrate N_{sub}=0.87-2.76i

Processing: BARC, 200°C/90s; resist, 95°C/90s; Top coat, 90°C/60s; PEB, 115°C/90s; Develop, 60s in CD26.

Figure 6.12 (a) shows the simulation result for light intensity distribution within the resist film at 1.35NA (35 nm half pitch) with TE polarization. The substrate reflection is reduced to 0.004% so none standing wave effects are observed in the simulation plot. The corresponding SEM cross-sectional photograph of the experimental result is shown in Figure 6.12 (b). Resist patterns with squared profiles were observed.

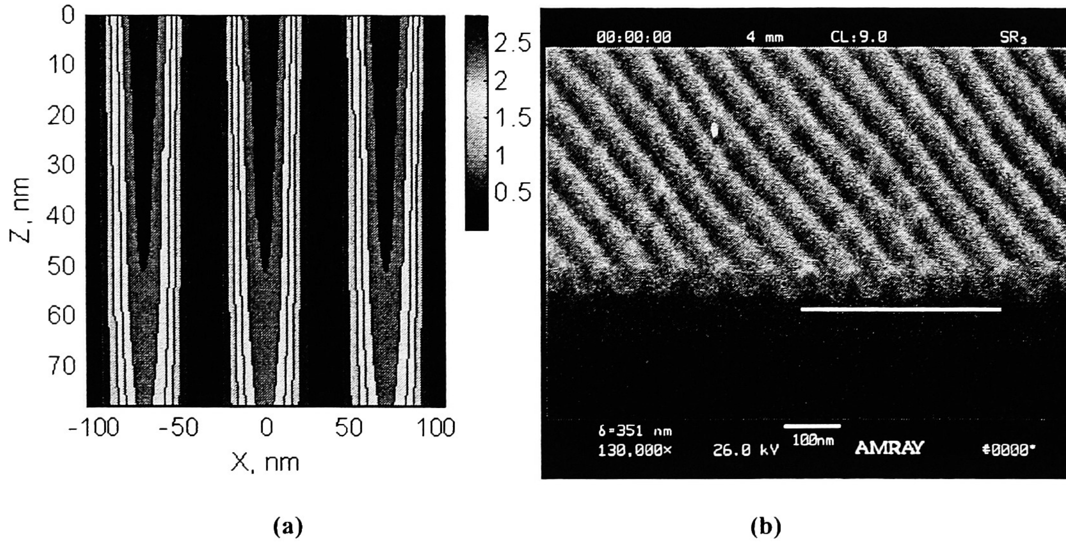

Figure 6.12 Numerical calculation and SEM cross-sectional photograph of two-beam interferometric lithography with TE polarization at 1.35NA, 35nm half pitch. (a) Numerical Calculation; (b) SEM cross-sectional photograph.

To image at 1.50NA, a phosphoric acid with a refractive index of 1.53 is employed as the immersion fluid. Figure 6.13 (a) shows the simulation result for light intensity distribution within the resist film at 1.50NA (32 nm half pitch) with TE polarization. The corresponding SEM cross-sectional photograph of the experimental result is shown in Figure 6.13 (b). A resist fringe with 32 nm half pitch is clearly seen but the resist profile is not very squared. The 2% BARC reflection might have contributed the image degrading. A BARC material with proper optical constants is necessary to improve imaging. Also, the photoresist material, designed to image 65 nm resolutions, needs to be engineered to afford a better image at 30 nm resolution regime. The 2-beam interferometric lithography examples shown in this section have proved the feasibility of immersion imaging.

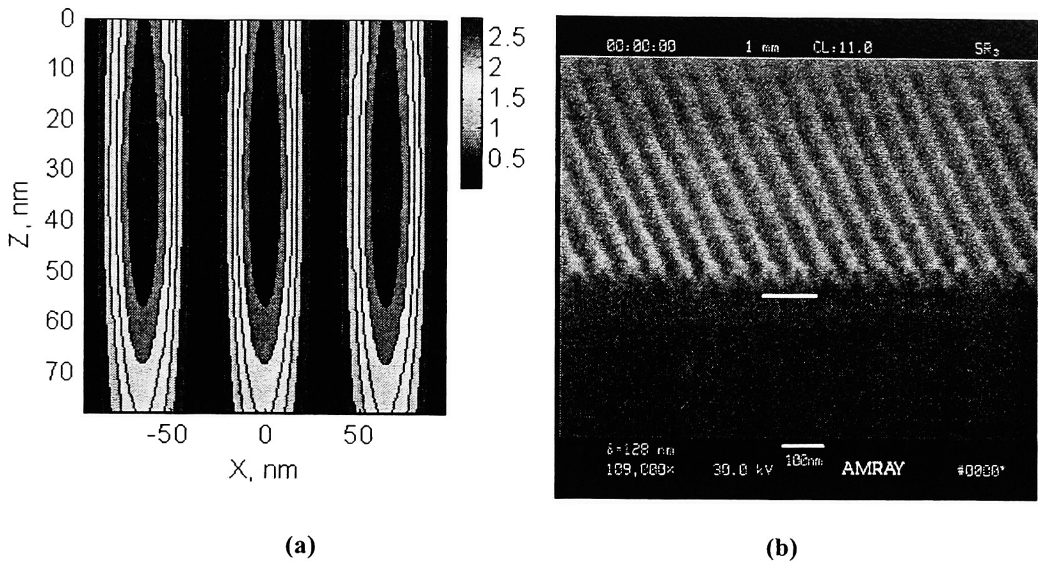

(a) (b)

Figure 6.13 Numerical calculation and SEM cross-sectional photograph of two-beam interferometric lithography with TE polarization at 1.50NA, 32nm half pitch. (a) Numerical Calculation; (b) SEM cross-sectional photograph.

6.4 Summary

In this chapter, the theoretical predictions about hyper-NA effects described in Chapter 3 were verified experimentally with two-beam interferometric lithography. The verification relied on the examination of SEM cross-sectional view of the resist film. The polarization effects were experimentally studied at 1.05NA, where the imaging behavior of TE and TM polarization is in great contrast. In the experiment, no BARC layer was used so that the standing wave effects were pronounced. In the case of TE polarization, the experimental results agree with simulation results. Elliptical resist features were observed. In the case of TM polarization, the features are rectangular in shape but the bottom row features appeared first and the top row appeared last but the intensity at the

bottom row is not the highest. However the simple threshold model would predict that the area with highest intensity starts developing first. Analysis showed that the fringe contrast varies with resist film depth and the contrast at the bottom row features was the highest. It is concluded that the speed point of a resist depends on the image contrast when the feature sizes are very small (sub-50 nm, in our study).

This chapter also explored experimentally the optimization of BARC at hyper-NA's. A bi-layer BARC was designed to suppress reflection for both 1.05NA and 1.30NA. Two-beam lithography with this BARC at 1.05NA and 1.30NA has produced resist line features without any standing wave effects. The experimental results agree with the numerical predictions.

CHAPTER 7

EXPERIMENTAL INVESTIGATION OF SOLID IMMERSION

7.1 Introduction

As described in previous chapters, the resolution of an optical projection system may be enhanced by immersion techniques. Governed by Snell's law, the maximum obtainable NA is determined by the refractive index of the photoresist, the media, or the final lens element (when the final lens surface is flat), whichever is smaller. In air, the maximum obtainable NA is 1.0. With liquid immersion, the maximum obtainable NA is the refractive index of the liquid. The refractive index of water, a candidate fluid for 193-nm immersion lithography, is 1.437. Considerable efforts are being put into seeking fluids with high refractive indices. As an example, an aqueous solution of phosphoric acid (H_3PO_4) is found to possess a refractive index of 1.54.[53] At the same, it is well known that some solids may have very high values of refractive index. For example, the refractive index of fused silica is 1.56, BaF_2 1.58, LaF_3 1.64, Al_2O_3 sapphire 1.92 at the wavelength of 193 nm.[55] While fluids with refractive indices rivaling those of solids may not be immediately available, it is worthwhile to investigate the feasibility of solid immersion imaging, where a high refractive index solid is utilized as the final optical element above the photoresist coated wafer.

Solid immersion imaging techniques could provide opportunities to probe high NA imaging behaviors at values that are not currently available in liquid immersion

imaging. Using crystalline sapphire (n=1.92 @193nm), solid immersion imaging allows NA values up to 1.92. This is able to bring the NA value well above 1.70, the typical refractive index value of a 193-nm wavelength photoresist. Therefore, it is possible to bring the imaging angle in the photoresist close to 90°, providing the capability to study polarization effects in the resist at full range of oblique angles. Moreover, it is generally believed that the physical resolution limit of a photoresist at a certain source wavelength is determined by the refractive index of the resist. Therefore, the ultimate optical resolution limit depends on the refractive index of the resist if we might have to keep using the same wavelength. In the industry, it is actively pursued to increase the refractive index of resists. On the other hand, this solid technique allows NA above 1.7, the refractive index of a 193-nm resist, making it possible to expose the resist with evanescent waves, which could break the physical resolution limit of a photoresist.

This chapter is intended to address the issues associated with solid immersion technique. In addition, the feasibility of using evanescent wave to break the physical resolution of a photoresist will be explored.

7.2 Theoretical Considerations

In contrast to liquid immersion technique, solid immersion uses a solid as the imaging media. The solid surface is supposed to be as close to the resist surface as possible ideally in contact with one another. However, the inevitable presence of surface topography makes the optical contact difficult. The situation can be approximated with a thin gap between the solid surface and the resist, as illustrated in Figure 7.1. Incident light from the solid media has to tunnel through the gap since NA is larger than the refractive

index of the gap (it would not be called solid immersion if NA was smaller than the refractive index of the gap material). The gap thickness should be controlled to be much smaller than the incident wavelength to guarantee light can penetrate through the gap. Employing the thin film theory introduced in Chapter 2, the transmission of the gap can be analyzed as a function of NA, gap thickness and gap refractive index.

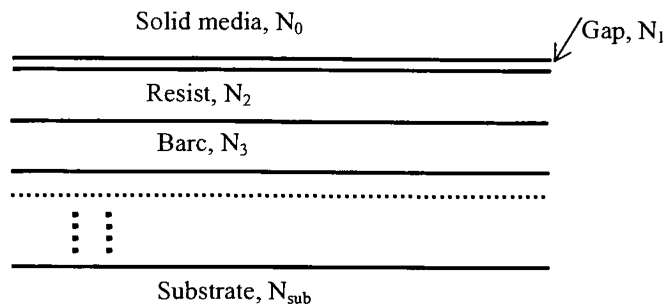

Figure 7.1 Illustration of a gap between the solid material and the resist film due to surface topography. NA is larger than the refractive index of the gap. Light has to tunnel through gap to expose the resist.

The optical constants of the film assembly used for the analysis are listed in Table 7.1. The analysis results are listed in Figure 7.2 In the figure, the transmittance of the gap is plotted versus gap thickness at various NA values for the situations of air gap and water gap. For air gap at NA=1.55, the transmittance for both TE and TM polarization dies off exponentially, virtually vanishing beyond 100 nm. As NA is increased, the transmittance drops off more quickly. At NA=1.66, it virtually vanishes beyond 60 nm. At 1.85NA, it virtually vanishes beyond 40 nm. The results also show that filling the gap with fluid, for example water, will greatly alleviate the gap thickness requirements. At NA=1.55 and

NA=1.66, there are still significant amounts of transmitted beyond 100 nm gap thickness. At NA=1.85, the vanishing point is 60 nm. Therefore, filling the gap with fluid is very beneficial. The above analysis shows it is very critical to control the gap thickness in solid immersion lithography. A tolerable gap thickness depends on the NA value, the film assembly, as well as the refractive index of the gap materials.

In Figure 7.2, the distinction between TE and TM polarization behaviors is very noticeable. At close to 0 nm gap thickness, more TM than TF energy is coupled into the photoresist film layer. As the gap thickness is increased, there is a cross point where TE and TM energy is equally coupled. Beyond this point, more TE and TM energy is coupled. At some points, the coupling difference is considerable. For example, at 1.55NA with 20 nm air gap (Figure 7.2 (a)), the coupling difference is more than 50%. If the gap can be precisely controlled, this behavior may be utilized for imaging polarization control. The sensitivity of the gap transmittance to gap thickness is also worth of attention. Low gap thickness sensitivity is expected for better exposure dose control. It is possible to find a gap configuration which has minimal sensitivity. For example, at 1.55NA with 18 nm water gap (Figure 7.2(d)), the sensitivity is minimal.

The above analysis has shown that water gap is preferred over air gap in terms of gap dimension and gap thickness sensitivity control. To investigate the gap index effect more carefully, gap thickness for 50% energy coupling loss is plotted versus gap index at 1.66NA in Figure 7.3. 50% is an arbitrarily set tolerance value. The curve shows that tolerable gap thickness increases exponentially as the index is increased close to the NA value, 1.66. High index gap materials are always desirable.

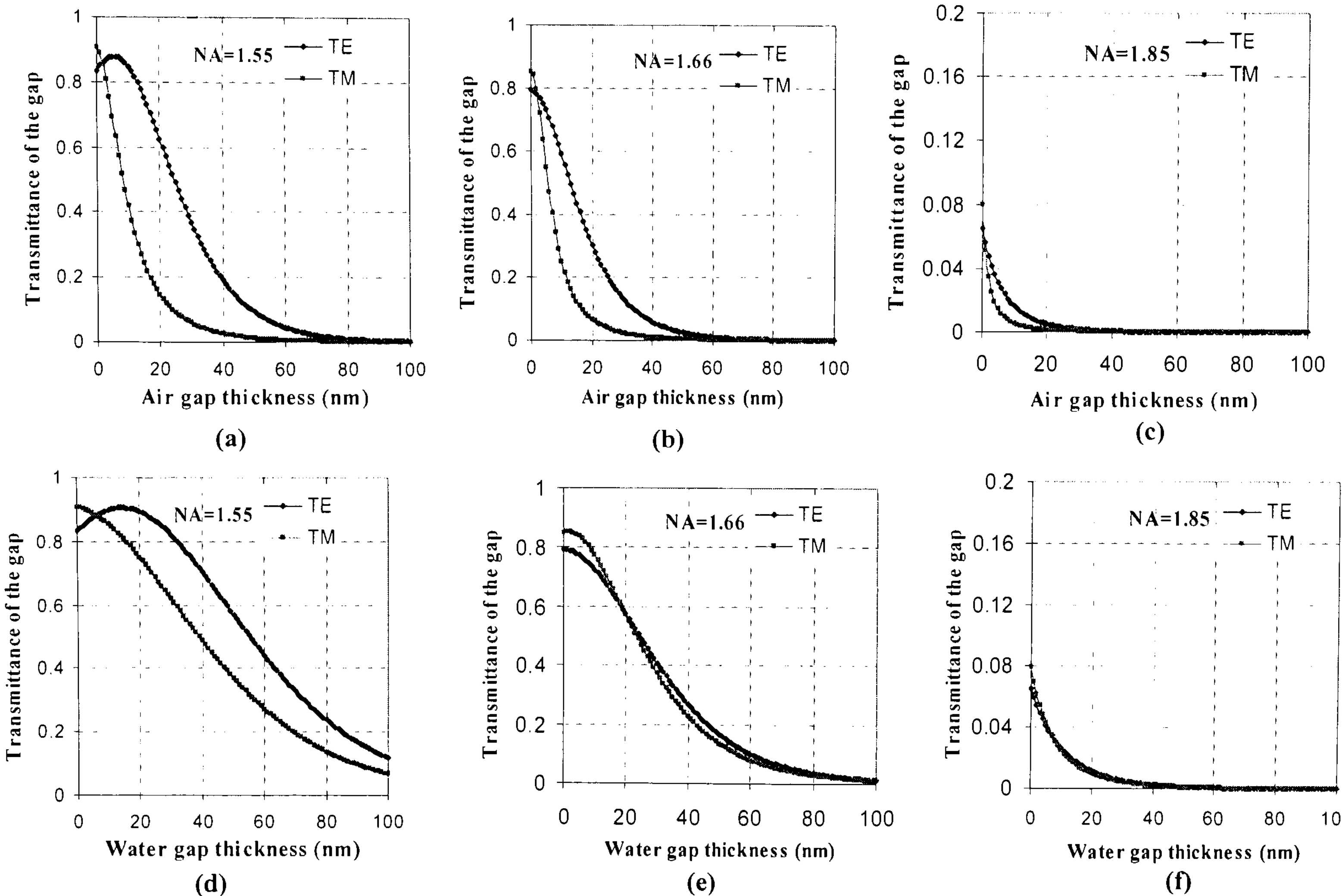

Figure 7.2 Analysis of gap transmittance for solid immersion at wavelength of 193nm for various NA values. The gap is filled with air or water.

Table 7.1 Optical constants and film thickness for resist assembly used for analysis in Figure 7.2

Immersion solid sapphire, N_0=1.92
Air (N_1=1.00) or water (N_2=1.00) , d_1=0~100 nm
Resist, N_2=1.71-0.009i, d_2=70 nm
BARC, N_3=1.70-0.05i, 148 nm
Substrate N_{sub}=0.87-2.76i

Table 7.2 Optical constants and film thickness for resist assembly used for analysis in Figure 7.3

Immersion solid (sapphire), N_0=1.92
Gap index =1~1.65
Resist, N_2=1.71-0.009i, d_2=70 nm
BARC, N_3=1.70-0.05i, 148 nm
Substrate N_{sub}=0.87-2.76i

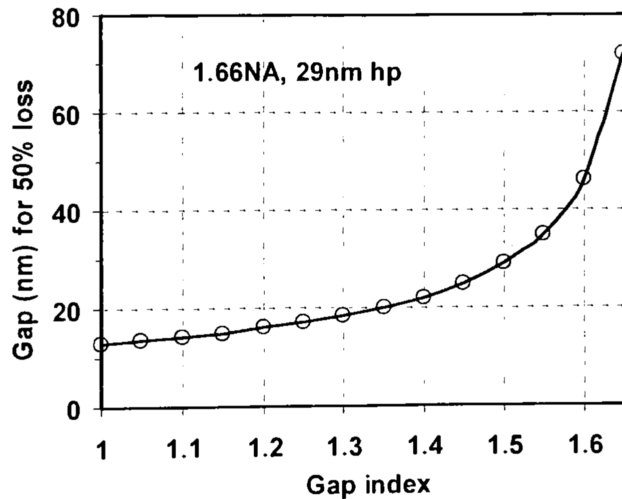

Figure 7.3 Gap thickness of 50% light loss at NA=1.66 versus gap index. The

7.3 Experimental Methods

As mentioned in Chapter 1 and Chapter 4, sapphire is a suitable material for solid immersion since it is transparent and has a refractive index of 1.92 at the wavelength of 193 nm. The previous analysis indicates that it is critical to bring the gap between the resist film and the solid surface as close to optical contact as possible. The roughness of the surface of a bare silicon wafer is usually within a few nanometers but it is much harder to polish the surface of sapphire materials. Fortunately, the crystalline structure of sapphire is a hexagonal system.[68] This makes it possible to cut out an equilateral triangle prism along the natural cleavage planes concomitant with almost perfect flat surfaces. The sapphire equilateral triangle prism obtained in this way is suitable for solid immersion lithography application. Two light beams incident on two sides of the prism interfere on the third side of the prism, as shown in Figure 7.4. A mechanical structure is used to hold a resist coated wafer against one lateral of the prism so that the exposing light can be coupled into the resist film through the prism. Two pairs of screws are used to tighten up the fixture. On the lower part of the fixture, there is a small plateau which helps to apply pressure on the center of the water. The area of the plateau is about 5mm×5mm, which is approximately the area of the exposure area. A photograph of the mechanical fixture is shown in Figure 7.5.

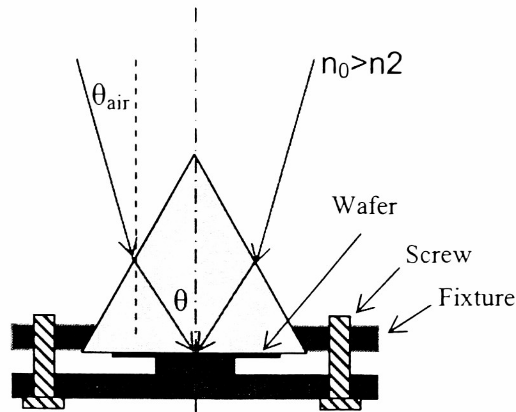

Figure 7.4 Mechanical fixture used to hold the resist coated wafer against one lateral of the equilateral triangle prism.

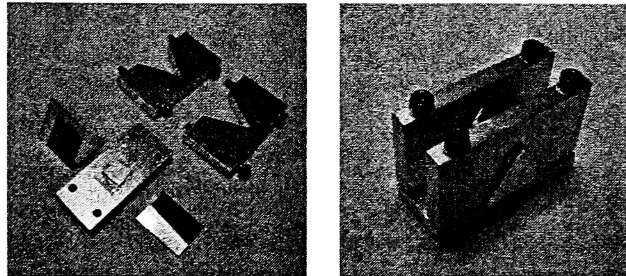

(a) Before assembly; (b) After assembly.

Figure 7.5 Photograph of the mechanical fixture for solid immersion.

The incident angle θ in the prism is related to the incident angle θ_{air} in the air through Equation [4-2]

$$\theta = \frac{\pi}{3} - \arcsin\left[\frac{\sin(\pi/3 - \theta_{air})}{n}\right]. \qquad [4\text{-}2]$$

The angle θ_{air} ranges from 0° to 90°. The correspondent θ ranges from 33.2° to 90°. For aluminum oxide (n=1.92), the NA ranging from 1.05 to 1.92 is obtainable with this equilateral triangle prism.

The actual percentage of light that could be coupled into the resist film can be measured in a simple way illustrated in Figure 7.6. In Figure 7.6(a), the total reflection from the prism is measured in the absence of a resist wafer. The intensity read on the photo meter is used as a baseline for the following measurement. Then, a resist wafer is coupled to the prism using the designed fixture. The reflected light is measured again, as shown in Figure 7.6 (b). In comparison with the base line, the percentage of light coupled into the resist film can be calculated. The baseline measurement insures that the light losses at the interfaces, in the air, as well as in the prism itself are compensated.

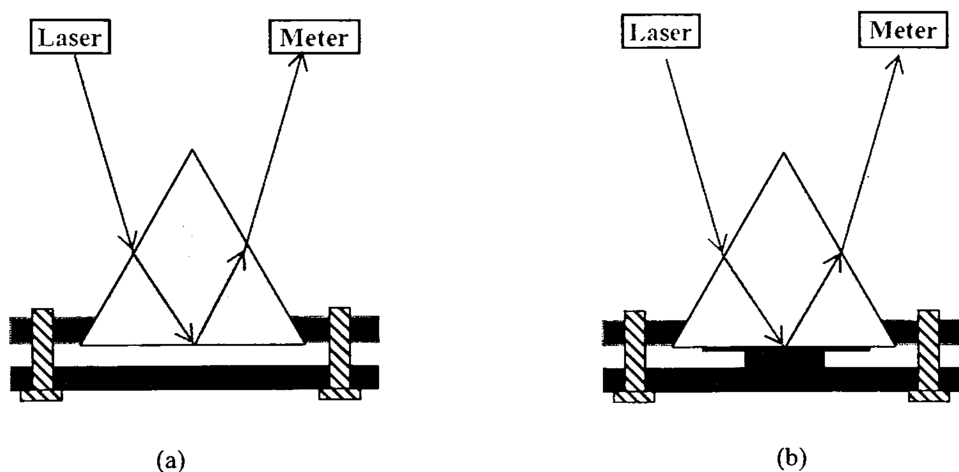

Figure 7.6 Illustration for measuring light that is coupled into the resist. (a) Total reflection as base line; (b); Measuring reflection with wafer coupled to the prism.

7.4 Results and Discussion

7.4.1 Light Coupling Analysis

To expose the resist, light has to be coupled into the resist film through the gap between the resist film and the sapphire prism. The mechanical fixture described in Figure 7.5 is used to minimize the gap. Before the pressure is applied, the interface looks

like a mirror due to total reflection. After the pressure is applied, a small area with dark color like the shape of the little plateau on the lower part of the fixture (Figure 7.4) can be visibly seen. The dark color is the resist film color, indicating that the gap thickness is much smaller than a visible wavelength. Since the exposing wavelength (193 nm) is much shorter than the visible wavelengths, it is still necessary to evaluate the gap thickness experimentally. The visible dark color shape can be used to guide the application of even pressure over the four screws.

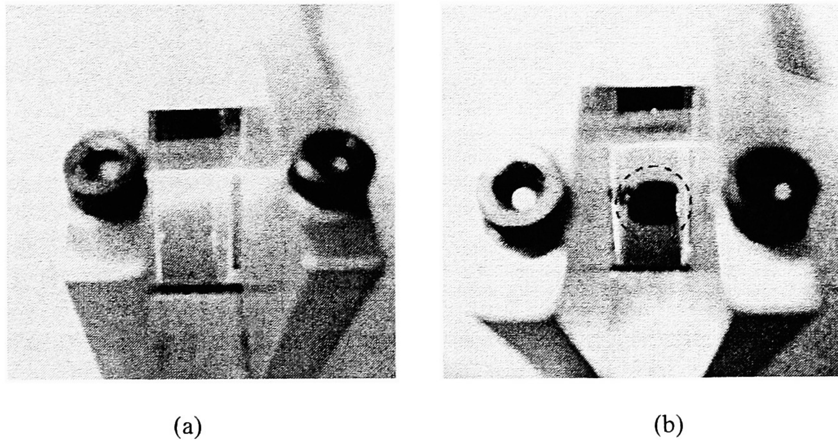

(a) (b)

Figure 7.7 Visible appearance of the interface before and after pressure application. (a) Before the pressure is applied, the interface looks like a mirror due to total reflection; (b) After the pressure is applied, a small area with dark color is visible.

The percentage of light which is coupled into the resist film can be characterized using the approaches illustrated in Figure 6.5. For a resist film assembly in Table 7.3, the measurement shows that 49.5% light is coupled into the resist film at NA=1.66. The measurement in turn can be used to estimate the air gap thickness. In Figure 7.8, the reflectance at the resist-sapphire interface is plotted versus air gap thickness using

parameters in Table 7.3. The air gap thickness corresponding to 50.5% reflectance is found to be 12nm.

Table 7.3 Film stack used for measuring gap thickness.

Immersion solid (sapphire), N_0=1.92
Air gap, N_1=1.00, d_1=0~50 nm
Resist, N_2=1.71-0.399i, d_2=78 nm
BARC, N_3=1.70-0.1i, 92 nm
Substrate N_{sub}=0.87-2.76i

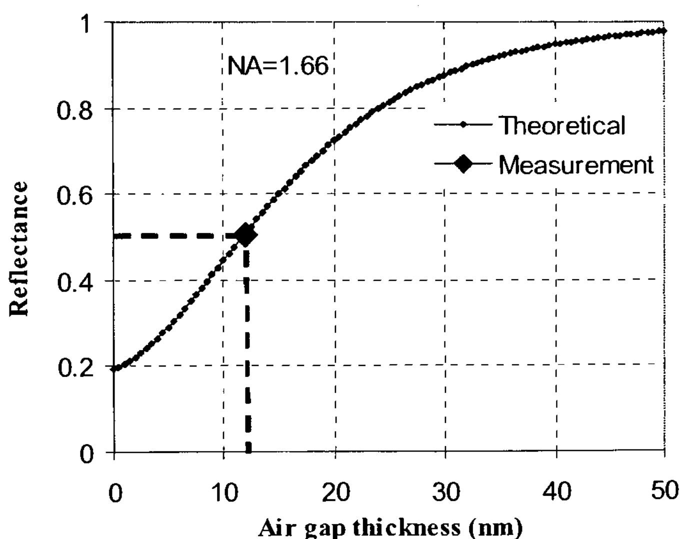

Figure 7.8 Reflectance at the resist-sapphire interface versus air gap thickness using parameters in Table 7.3. From the measured reflectance, the approximated air gap thickness can be found from the curve.

7.4.2 Solid Immersion Interferometric Imaging

With the fixture shown in Figure 7.4, interferometric lithography at 193-nm with TE polarization at various NA's has been successfully evaluated. Since no immersion fluids are involved, it is considered as solid immersion. The parameters of a resist film assembly for 1.42 NA interferometric lithography is listed in Table 7.4, along with the processing conditions. The BARC thickness is the first reflection minima (0.47%

reflectance at 40nm.), as shown in Figure 7.9. A SEM photograph of the resulted resist pattern is shown in Figure 7.10. The measured half pitch is 34 nm, which corresponds to an NA value of 1.42. It is noted that the resist pattern is not developed down to the BARC layer. A comparison with the simulation result will elucidate what caused that. The simulated light intensity contours within the resist layer are shown Figure 7.11. The light is much weaker at the bottom of the resist due to resist absorption so the bottom of the resist patters is less developed. As the NA is pushed to higher values, the absorption effect will become more obvious in that the resist film becomes much optically thicker, as has been observed at higher NA values and will be discussed in more details in the following discussion.

Table 7.4 Resist film stack used for 1.42NA

Layer
Top coat, N_1=1.414, d_1=40 nm
Resist, N_2=1.71-0.039i, d_2=78 nm
BARC, N_3=1.82-0.34i, 40 nm
Substrate N_{sub}=0.87-2.76i

Processing: BARC, 200°C/90s; resist, 95°C/90s; Top coat, 90°C/60s; PEB, 115°C/90s; Develop, 60s in CD26.

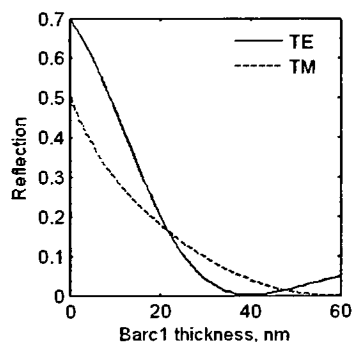

Figure 7.9 BARC thickness calculation for resist stack in Table 7.4.

It is also observed that noticeable resist pattern roughness is present. This is a result of the fact that the chemical resolution of the resist has been reached. A resist capable of resolving 20-40 nm features needs to be developed.

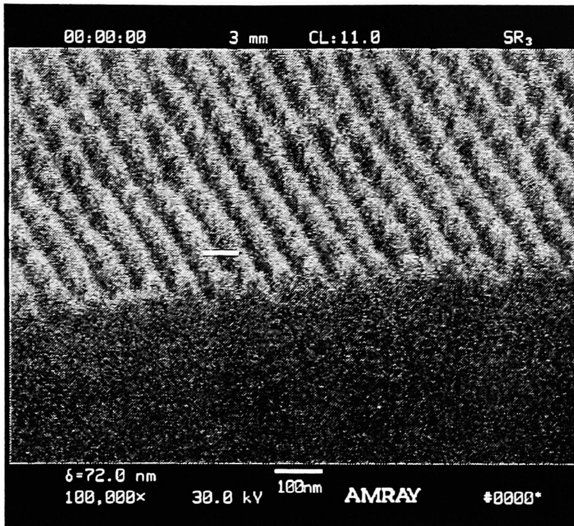

Figure 7.10 SEM for 1.42 NA, 34nm half/pitch, TE polarization using film stack in Table 7.4.

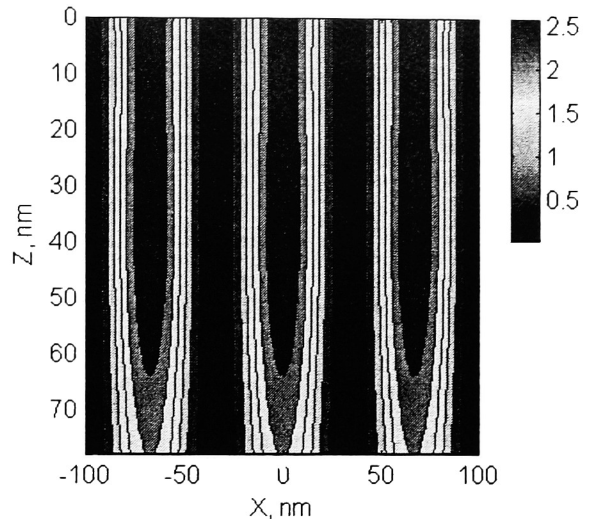

Figure 7.11 Light intensity distribution within the resist layer for 1.42NA using TE polarization.

The parameters as well as the processing conditions of a resist film assembly for 1.60NA interferometric lithography is listed in Table 7.5. At this NA, the BARC in the 1.42NA case does not work any more in that the reflection from the bottom surface of the BARC layer is too weak to cancel the reflection at the surface of the BARC with destructive interference. Instead, a more transparent BARC with refractive index of 1.70-0.10i is used. Actually, it is a BARC material used for 248-nm lithography but with the right optical constant for this case. At the first reflection minima (100 nm), the reflectance is as low as 0.02%, as shown in Figure 7.12. A SEM photograph of the resulted resist pattern is shown in Figure 7.13. The measured half pitch is 30 nm, which corresponds to an NA value of 1.60.

Table 7.5 Resist Film stack used for 1.60NA

Top coat, N_1=1.414, d_1=40 nm
Resist, N_2=1.71-0.039i, d_2=78 nm
BARC, N_3=1.70-0.10i, 100 nm
Substrate N_{sub}=0.87-2.76i

Processing: BARC, 200°C/90s; resist, 95°C/90s; Top coat, 90°C/60s; PEB, 115°C/90s; Develop, 60s in CD26.

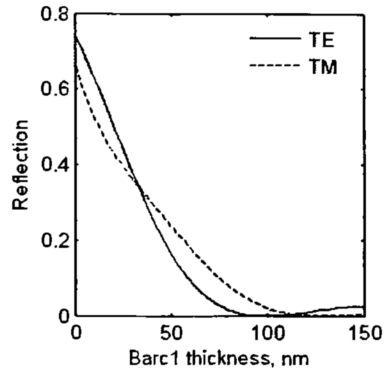

Figure 7.12 BARC thickness calculation for resist stack in Table 7.5.

The SEM photograph in Figure 7.13 also shows that the depth of the resist pattern is very shallow, 20~30 nm but the resist film has a thickness of 78 nm. A comparison with the simulation results helps to explain what caused that. The simulated light intensity distribution contours within the resist layer are shown Figure 7.14. The peak intensity at the top of the resist film is about 2 times stronger than that at the bottom of the resist layer due to resist absorption so the resist pattern is limited to a depth of 20-30nm. In compassion with the case of 1.42NA, the absorption effect for the same resist at 1.60NA has increased in that the resist film becomes optically thicker at higher NA values due to the obliqueness of the light beam. Using equation 3-17, it can be calculated that, the optical thickness of the resist film at 1.60NA is 2.83 times thicker than the physical film thickness. It is required that the resist be more transparent to result in a larger resist pattern depth. In this experiment, the resist apparently is not engineered for hyper-NA imaging. This is an important aspect that should be addressed when hyper-NA resists are developed in the future.

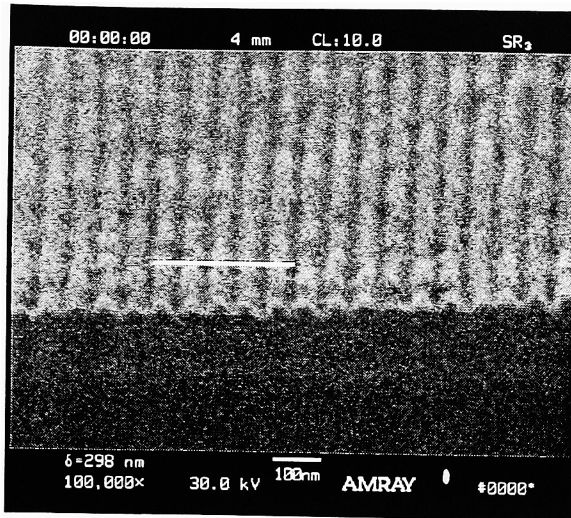

Figure 7.13 SEM for 1.60NA, 30 nm half/pitch, TE polarization using film stack in Table 7.5

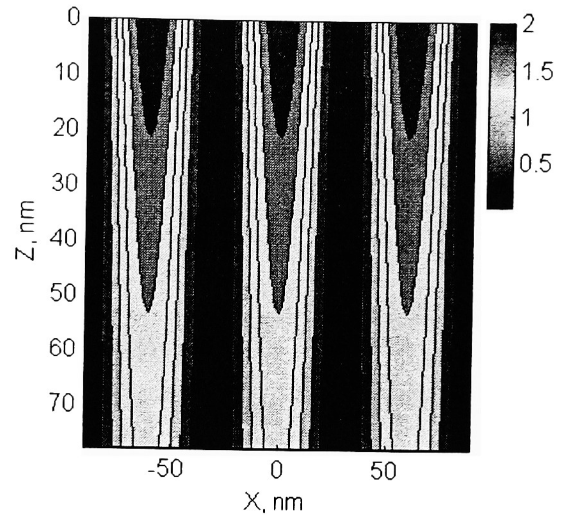

Figure 7.14 Light intensity distribution within the resist layer for 1.60NA using TE polarization.

The resist assembly in Table 7.5 was also used for 1.66NA interferometric lithography. At this NA, the BARC reflection is 0.52% at a thickness of 100nm. ASEM photograph of the resulted resist pattern is shown in Figure 7.13. The measured half pitch is 29 nm, which corresponds to an NA value of 1.66. Using equation 3-17, it can be calculated that, the optical thickness of the resist film at 1.66NA is 4.2 times thicker than the physical film thickness. Therefore, the resist pattern depth is a little shallower than that for the case of 1.60NA. This is consistent with the simulations results shown in Figure 7.17.

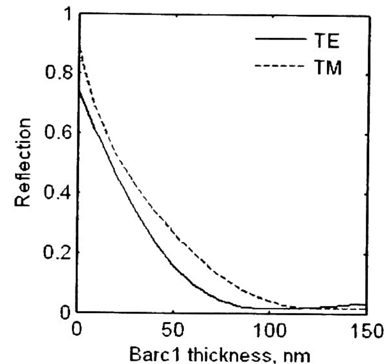

Figure 7.15 BARC thickness calculation for resist stack in Table 7.5 but for 1.66NA.

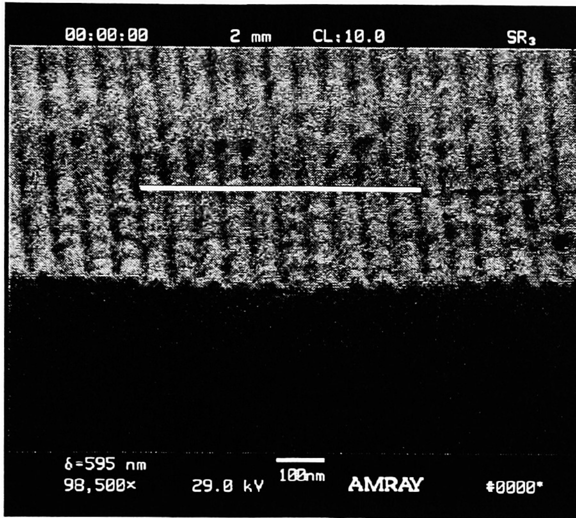

Figure 7.16 SEM for 1.66NA, 29 nm half/pitch, TE polarization using film stack in Table 7.5

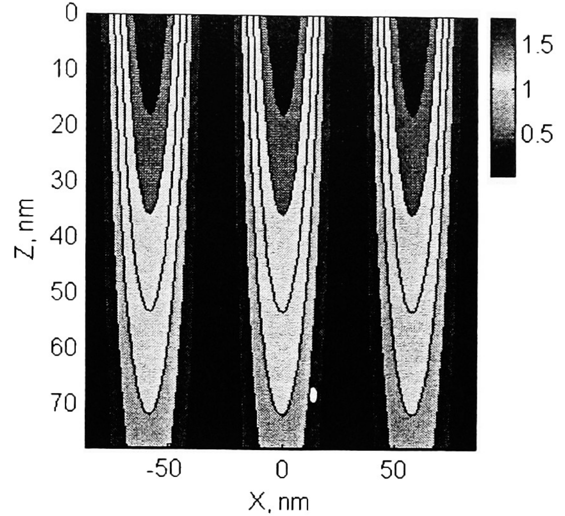

Figure 7.17 Light intensity distribution within the resist layer for 1.66NA using TE polarization.

7.4.3 "Evanescent Wave" Imaging

The refractive index of sapphire is 1.92 so it is possible to push NA above the real part of the refractive index of the resist. This will be a situation very similar to a phenomenon called total internal reflection. To analyze this situation, let's use the convention adopted in Chapter Two. The refractive index of the media is n_0 and the incident angle in the media is θ_0. The corresponding NA=$n_0 \sin\theta_0$. n_2-ik_2 is the refractive index of the resist material and θ_2 is the incident angle in the resist film. Using Snell's law, we have

$$\sin\theta_2 = \frac{n_0 \sin\theta_0}{n_2 - ik_2} = \frac{n_2 + ik_2}{n_2^2 + k_2^2} n_0 \sin\theta_0 . \qquad [7\text{-}1]$$

For $k_2 \ll n_2$,

$$\cos\theta_2 = \pm\sqrt{1-\sin\theta_2{}^2} = \pm\sqrt{1-\left(\frac{n_0\sin\theta_0}{n_2}\right)^2}\ . \qquad [7\text{-}2]$$

Since we are concerned with the case where $NA = n_0\sin\theta_0 > n_2$,

$$\cos\theta_2 = \pm\sqrt{1-\sin\theta_2{}^2} = \pm i\sqrt{\left(\frac{n_0\sin\theta_0}{n_2}\right)^2 - 1}\ . \qquad [7\text{-}3]$$

The wave function in the resist layer can be expressed as

$$E_2 = E_{02}e^{-i\frac{2\pi}{\lambda}(n_2 - ik_2)(x\sin\theta_2 + z\cos\theta_2)} \qquad [7\text{-}4]$$

where E_2 presents the electrical field in the resist film and E_{02} is the amplitude. Substitution of Equation [7-1] and [7-3] into Equation [7-4] will give

$$E_2 = E_{02}e^{-z\frac{2\pi}{\lambda}\sqrt{(n_0\sin\theta_0)^2 - n_2{}^2}}\, e^{-x\frac{2\pi k_2}{\lambda\ n_2}n_0\sin\theta_0}\, e^{-i\frac{2\pi}{\lambda}\left(xNA + zk_2\frac{\sqrt{(n_0\sin\theta_0)^2 - n_2{}^2}}{n_2}\right)}\ . \qquad [7\text{-}5]$$

When $NA = n_0\sin\theta_0 > n_2$, the first exponential term in Equation [7-5] implies that the electrical field in the resist film attenuates in the z direction exponentially. The exponential power is proportional to $\sqrt{(n_0\sin\theta_0)^2 - n_2{}^2}$ The second exponential term indicates the absorption effects of the resist. The second exponential term is the propagation phase term. Since k_2 is considerably small in comparison to n_2, the propagation phase term indicates that the wave propagates in parallel to the film boundary. In optics, it is referred to as an "*Evanescent wave*". [69] The situation is illustrated in Figure 7.18. The critical angle is $\sin\theta_c = \frac{n_2}{n_0}$. Below the critical angle, the incident wave is coupled into the photoresist film as a homogeneous propagation wave. Above the critical angle, incident wave is coupled into the photoresist film as an evanescent wave. Can evanescent wave cause chemical reactions? It is noted that

evanescent wave have been utilized for photo-polymerization.[70-74] The penetration depth limit of the evanescent wave was taken advantage of so that the photo-polymerization occurs in the shallow surface on the chemical solution. In our situation, the penetration depth limit is unfavorable to us but the resultant pitch is definitely favorable.

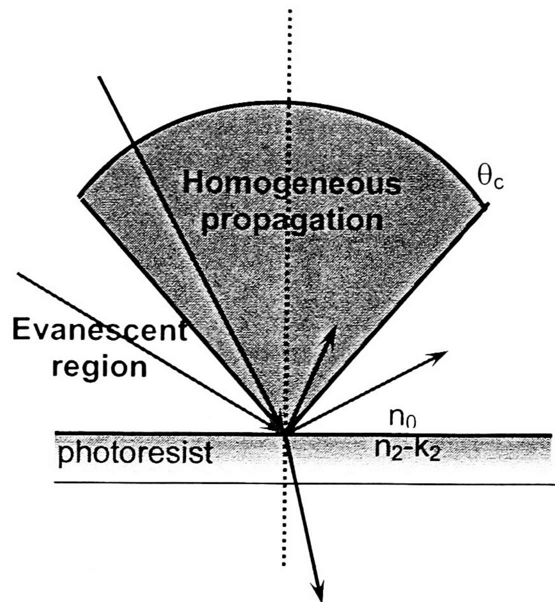

Figure 7.18 Illustration for homogeneous propagation region and evanescent wave region.

The energy percentage of evanescent wave coupled into the resist drops off exponentially as the NA is increased. In Figure 7.19, the energy percentage coupled into the photoresist is plotted versus NA. The refractive index of the photoresist is 1.71-0.039i and the above media is aluminum oxide (n=1.92). The curve is almost flat for NA<1.6. Then it drops off slowly due to high angle reflection at the interface. Above NA=1.71, it becomes evanescent wave and drops off exponentially, reaching 0 at NA=1.92. If we label the x axis as spatial frequency, it will present the frequency response property of the system. Imaging with evanescent wave allows us to capture spatial information beyond

the traditional cut-off frequency but its optical response is much weaker than homogeneous propagation wave.

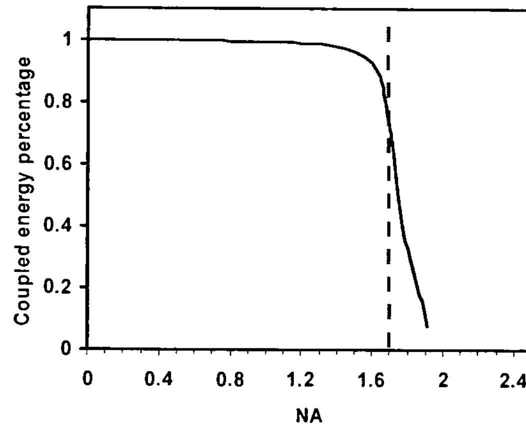

Figure 7.19 Energy percentage Coupled into photoresist versus NA in an aluminum oxide final lens element system. Assume that there is no air gap. The refractive index of the photoresist is 1.71-0.039i.

Let's go back to the two-beam interference. When NA>n2, essentially, there are two evanescent waves traveling in opposite direction, thus forming interferometric fringe patterns. However, in the film thickness direction (z direction), the intensity attenuates exponentially. As a result, only a very shallow depth of resist film could be exposed. The simulation results for 1.85NA using resist assembly in Table 7.6 are shown in Figure 7.20, indicating that only less than 10 nm thickness of resist film could be developed. A SEM photograph of the resulted resist pattern is shown in Figure 7.21. The fringe pattern is very clear but with a depth of a few nanometers. The measured half pitch is 26 nm, which corresponds to an NA value of 1.85. Those are consistent with the simulation results.

Although imaging with evanescent waves only allows developing a few nanometer thickness of resist, it does enhance resolution without restriction on the refractive index of the resist. With a suitable etching technique, it is possible to transfer the pattern to the subsequent layers. Thus, it could be a competitive technique for sub-30 nanometer lithography.

Table 7.6 Resist Film stack used for 1.85NA

Resist, N_2=1.71-0.039i, d_2=78 nm
BARC, N_3=1.70-0.10i, 100 nm
Substrate N_{sub}=0.87-2.76i

Processing: BARC, 200°C/90s; resist, 95°C/90s; Top coat, 90°C/60s; PEB, 115°C/90s; Develop, 60s in CD26.

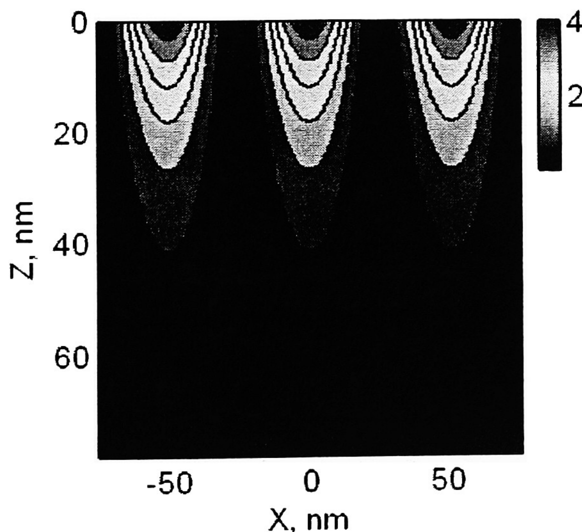

Figure 7.20 Light intensity distribution within the resist layer for 1.85NA using TE polarization.

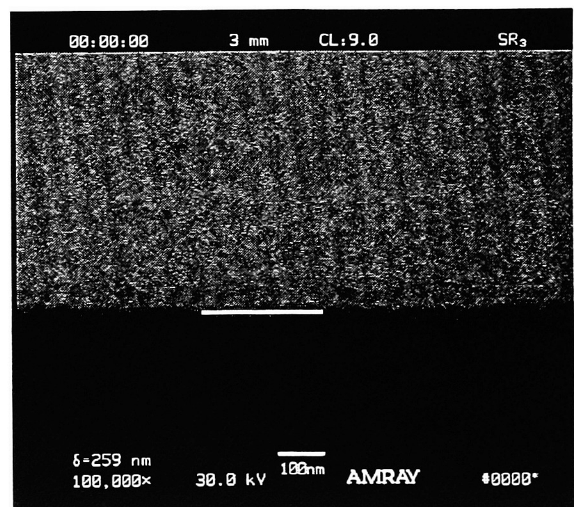

Figure 7.21 SEM for 1.85NA, 26 nm half/pitch, TE polarization using film stack in Table 7.6

7.5 Summary

In this chapter, the concept of solid immersion lithography was investigated experimentally. Theoretical analysis showed that the gap between the solid surface and the resist surface is required to be less than 2-30 nm depending on NA, to allow significant coupling of light into the resist film. An equilateral triangle prim of sapphire material was used to couple light into the resist film. The natural cleavage planes of sapphire crystal were used to build an equilateral triangle prim to yield almost perfect flat surfaces which are essential to couple light from the prism to the resist film at hyper-NA values. With the designed mechanical fixture, a series of experiments at various NA values were performed successfully. The experimental results agreed with simulation results. It has been noted that the resist absorption effect increases with NA values due to the fact that light beams traveling at higher oblique angles in the resist film experience longer optical path. More interesting, it has been found that the NA values can be pushed higher than the real part of the refractive index of the resist, i.e., exposing resist with "evanescent waves". Imaging with evanescent waves can result in very tight pitches but the resist pattern is limited to a thickness of only a few nanometers. Nevertheless, with suitable etching techniques, it is possible to transfer the resist into the subsequent layers. The experimental results in this chapter have shown that solid immersion imaging is a potential technique for sub-30 nanometer lithography and is a valuable tool for hyper-NA imaging research.

CHAPTER 8

AIR BUBBLE INDUCED LIGHT SCATTERING EFFECTS ON IMAGE QUALITY IN 193 nm IMMERSION LITHOGRAPHY

8.1 Introduction

Driven by the demands in the microelectronic industry to produce smaller device geometries, conventional optical lithography has extended critical dimensions down to 65 nm using a 193 nm ArF (Argon Fluoride) excimer laser, along with the employment of resolution enhancement techniques such as phase-shift masking, off-axis illumination, optical proximity correction, pupil filtering, etc. It seems that the solution for the 45-65 nm technology node is to resort to a shorter wavelength illumination source, as was true in the past lithography generations. Unfortunately, at 157 nm, which is the next wavelength of laser poised for semiconductor manufacturing, the inherent properties of DUV (deep ultraviolet) light has generated virtually insurmountable barriers to lithographic practice, especially in the aspects of imaging and masking materials.[10-13] In the past few years, the difficulties in tackling these barriers have turned attentions to another alternative: immersion imaging at 193 nm.

Enhancement of optical resolution in immersion media with respect to air is described by Rayleigh's criteria, $R = k_1\lambda/(n\sin\theta) = k_1\lambda/NA$. It states that the minimum resolvable pitch is inversely proportional to numerical aperture of the objective lens.

Imaging in a liquid media effects the numerical aperture larger than 1.0, which is the upper limit for imaging in air. Equivalently, it can be argued that the light has a shorter wavelength in liquid. In addition to resolution enhancement, immersion lithography also results in a larger depth of focus, $DOF = \pm k_2 n\lambda / NA^2$.A numerical aperture larger than 1.0 can be achieved by immersing the whole wafer in an immersion media. However, the high volume nature of microelectronics manufacturing and its stringent environment requirements makes the idea of total immersion too awkward to be put into a production line. Alternatively, an introduction of a thin immersion liquid between the wafer and the final lens can create an equivalent enhancement of numerical aperture. This is the most practical and widely adopted optics configuration. Among the candidates for immersion liquids, water appears to be an excellent choice due to its high transmittance at a wavelength of 193 nm, as well as immediate availability and low processing cost. However, air bubbles are often generated in the process of introducing a water fluid layer between the resist and lens surfaces due to the high surface tension of water. The presence of air bubbles not only causes scattering of exposure light but also poses risks of forming defects that are the images of the bubbles themselves if they are close or attached to the surface of the wafer, *i.e.* the imaging plane. In Owa's[49] work, the formation, prevention and elimination of bubbles was discussed. According to this paper, bubble formation occurs when the gas-saturated water is shifted to a state of over-saturation due to changes in external conditions, *i.e.*, pressure, temperature. The mechanism suggests that degassing is an efficient way to prevent bubble formation. In spite of the plausibility of preventing bubble formation via degassing, it is still essential to understand the effects the presence of air bubbles has on image quality since complete suppression of air

bubbles seems unrealistic. Gau *et al*[75] analyzed the impact of the bubble size and bubble density on the optical performance of immersion lithography using Mie scattering theory. However, experimental observations are very essential in real lives. In this work, artificial beads are employed to mimic air bubbles. To our best knowledge, none work using our experimental approach has been reported, prior to the present paper. The work in this chapter has been published in Applied Optics.[76]

8.2 Geometrical Optics Model of Bubble Scattering

Scattering of air bubbles in water can be approximately described using a geometrical optics model.[77] An air bubble assumes a spherical shape in water when the hydraulic pressure due to gravity is ignored. The assumption is reasonable in lieu of immersion lithography where a thin layer of water with thickness of about 0.5 mm is applied. The reflection/refraction at the spherical interface causes the light stray into various directions, i.e. scattering. The relevant reflection/transmission coefficients can be approximated by flat surface Fresnel coefficients. However, the air bubble in water is a special case, where the refractive index of the bubble is less than that of the surrounding media, resulting in a contribution of total reflection to scattered irradiance at certain scattering angles. The situation is described in Figure 8.1 For an arbitrary ray incident on a bubble, the angle of incidence is $\mathrm{i} = \arcsin(\mathrm{s}/\mathrm{a})$, where *a* is the radius of the bubble, *s* is the deviation from the center. The critical incident angle is

$$\mathrm{i}_c = \arcsin(\mathrm{n}_i / \mathrm{n}_w) \qquad [8\text{-}1]$$

where n_i is the refractive index of the air, n_w is the refractive index of water. The corresponding critical scattering angle is

$$\theta_c = 180° - 2i_c. \quad [8\text{-}2]$$

At a wavelength of 193 nm, the refractive index of water is n_w=1.437. Therefore, the critical incident angle and critical scattering angle are

$$i_c = \arcsin\left(\frac{1}{1.437}\right) = 44°$$

$$\theta_c = 180° - 2i_c = 92°.$$

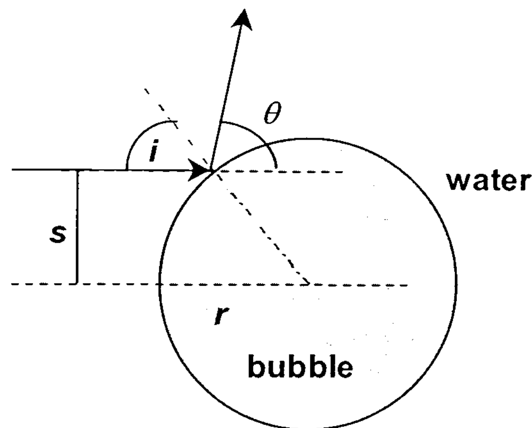

Figure 8.1 Reflection of a ray from a spherical bubble in water. Total reflection occurs when the incident angle i is larger than the critical angle, $sin^{-1}(n_i / n_w)$.

The presence of total reflection greatly enhances the light scattered into the region subtended by $0 \le \theta \le \theta_c$. In this case, the region covers all the forward directions. Hence, air bubbles in water cause strong scattering in all the forward directions. However, a complete understanding of scattering will require taking into account the effects of interference of the reflected light with other transmitted light. The rigorous

solution of the scattering pattern can be numerically evaluated by partial wave (Mie) theory. The Mie calculations are discussed in the following section.

8.3 Exact Computation of Scatter

In Mie scattering theory,[78] the incident, scattered, and internal fields are expanded in a series of vector spherical harmonics. The coefficients of these expansion functions are chosen so that the tangential components of the electric and magnetic fields are continuous across the surface of the sphere. Two calculation parameters are needed to specify a scattering case, the relative refractive index $m = n_i / n_w$ (where n_i and n_w are the refractive indices of air and water respectively) and the size parameter $ka = 2\pi n_w a /(n_i \lambda_i)$ (where a is the radius of the bubble, λ_i is the wavelength in air, k is the propagation vector. The scattering irradiance can be calculated from Equation [8-3] and [8-4],

$$i_j = i_{inc} I_j a^2 / 4R^2 \qquad [8\text{-}3]$$

$$I_j = |S_j|^2 (2/ka)^2 \qquad [8\text{-}4]$$

where subscript j denotes the polarization orientation ($j=1$, perpendicular to scattering plane; $j=2$, parallel to scattering plane). The term i_j is the scattered irradiance, i_{inc} is the incident irradiance, I_j is the normalized scattered irradiance, R is the distance from the bubble to the far-field observation point, and S_j is the complex scattering amplitudes. S_j can be evaluated from the Mie series. The number of modes used in the computations depends on size parameter X. The series are terminated after N terms, where N is the integer closest to $X + \frac{4}{X^3} + 2$. The criterion is based on reference[25].

At the wavelength of 193 nm, the scattering of an air bubble 2 μm in diameter was calculated according to Mie theory and plotted in Figure 8.2. The refractive index of water at this wavelength is 1.437. The logarithm of relative scattered irradiance was plotted against lateral distance instead of the usual angular direction in the Mie calculation, because this is the situation where the resist film is exposed to the scattered irradiance. The scattered irradiances at distances of 100, 200, 500, 1000 μm from the bubble are plotted in the figure. As shown in the figure, the scattered irradiance dies off quickly and the distribution in the lateral direction becomes more uniform. It indicates that the bubbles further from the resist have less effect on resist imaging.

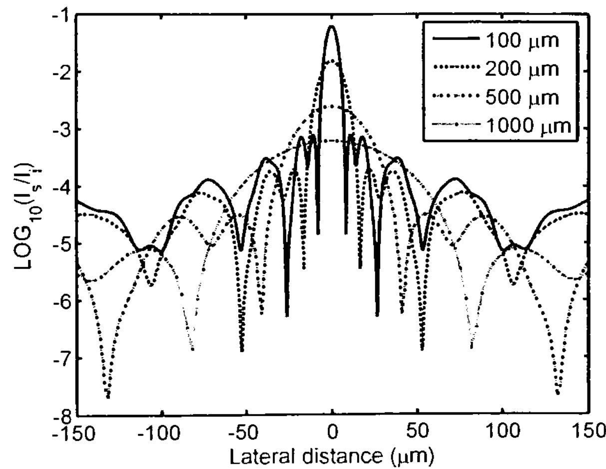

Figure 8.2 Lateral distribution of relative scattered irradiance of an air bubble in diameter of 2 μm from various distances from the bubble.

The fact that the bubble size and population in the water cannot be precisely controlled delivers extra difficulties to experimental bubble-scattering studies. Therefore, it would be beneficial to find synthetic spheres that are stable in water and possess similar scattering properties to air bubbles so that they can be used to mimic air bubble scattering in water. At the wavelength of 193 nm, air bubbles are transparent with a refractive index

of approximately 1.0. Ideally, a synthetic sphere with refractive index of 1.874+0*i* (so that the refractive index difference with water is the same as air bubble) would serve the purpose. Unfortunately, synthetic spheres with this index were not commercially available. Polystyrene (PST) beads (n=1.67+1.02*i*) and poly-methyl methacrylate (PMMA) (n=1.55+0.01*i*) are the closest matches. Mie scattering calculations of PST and PMMA beads 2 μm in diameter are conducted with the results plotted in Figure 8.3 and Figure 8.4 respectively. The results suggest that PST beads have a similar scattering pattern to air bubbles even though PMMA is more transparent at 193 nm. The 2-D distribution of scattered irradiance about air bubble, PST and PMMA were plotted in Figure 8.5, Figure 8.6 and Figure 8.7 respectively. It is obvious that the scattering pattern of PST beads resembles that of air bubble, especially in the forward direction. The results further suggest that PST beads are suitable to mimic air bubble in scattering study.

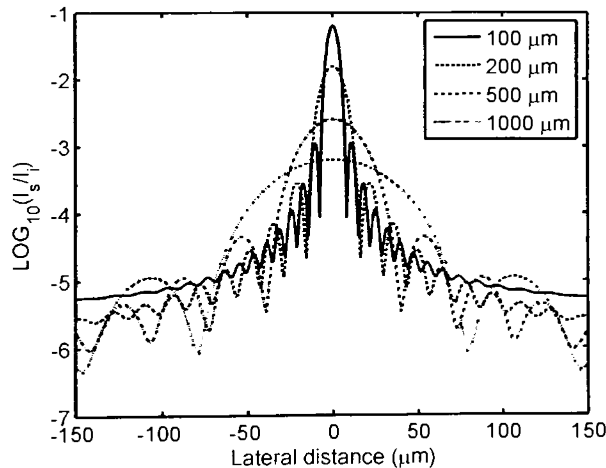

Figure 8.3 Lateral distribution of relative scattered irradiance of polystyrene sphere 2 μm in diameter from various distances from the bubble.

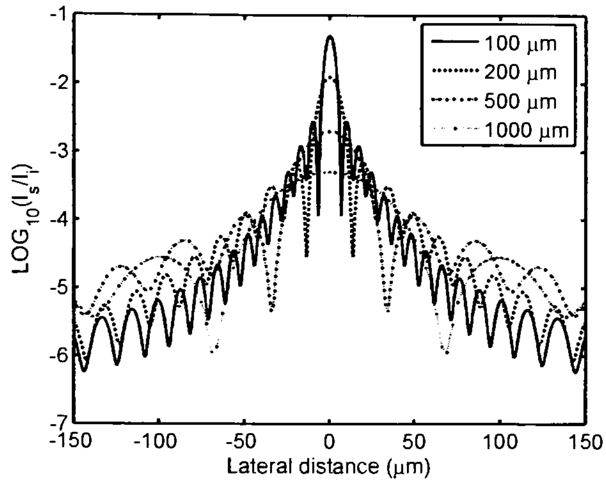

Figure 8.4 Lateral distribution of relative scattered irradiance of a PMMA sphere 2 μm in diameter from various distances from the bubble.

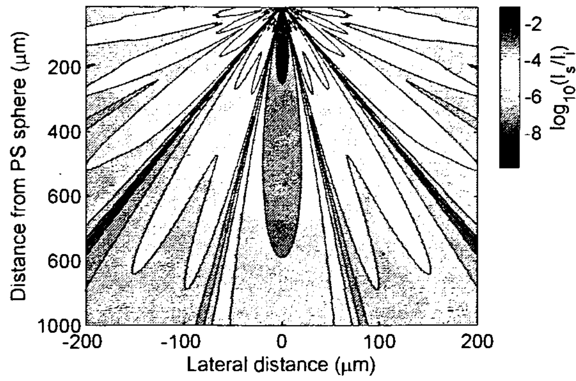

Figure 8.5 Distribution of relative scattered irradiance of an air bubble 2 μm in diameter in water.

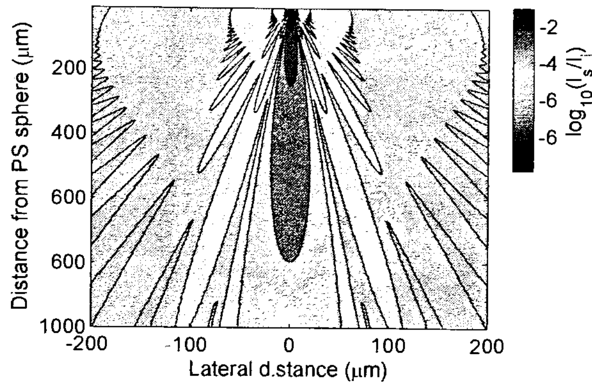

Figure 8.6 Distribution of relative scattered irradiance of a polystyrene sphere 2 μm in diameter in water.

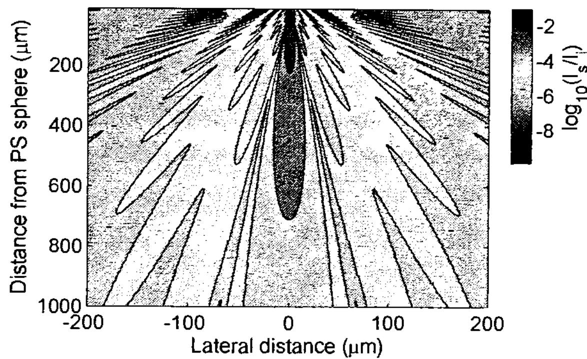

Figure 8.7 Distribution of relative scattered irradiance of a PMMA sphere 2 μm in diameter in water.

The size of the bubble is another important parameter determining its scattering pattern. In Figure 8.8 and Figure 8.9, the Mie scattering patterns of air bubbles 1 μm and 0.5 μm in diameter were plotted respectively. Along with Figure 8.5, it can be seen that the scattered irradiance in the forward directions becomes more uniform as the size

becomes smaller. It is fair to say that scattering due to smaller bubbles tends to form uniform background irradiance on the resist.

In the above numerical calculations, only one scattering sphere is involved but multiple spheres take part in scattering in a real situation. Due to the random distribution of scattering spheres in the media, the contribution to scattered irradiance from separate spheres is incoherent. The incoherent summation of scattered irradiance from all spheres is the total scattered irradiance. The Mie scattering calculation of two bubbles 2 μm in diameter with 100 μm separation was plotted in Figure 8.10, Figure 8.11, and Figure 8.12, for unpolarized, TE-polarized, and TM-polarized illumination, respectively. The scattered irradiance on the resist film is averaged to be more like a uniform background due to contributions from multiple spheres.

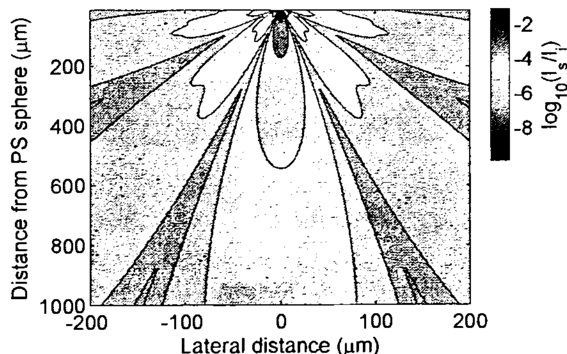

Figure 8.8 Distribution of relative scattered irradiance of an air bubble 1 μm in diameter in water.

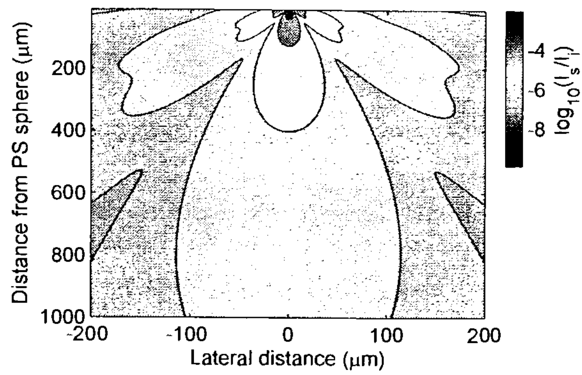

Figure 8.9 Distribution of relative scattered irradiance of an air bubble 0.5 μm in diameter in water.

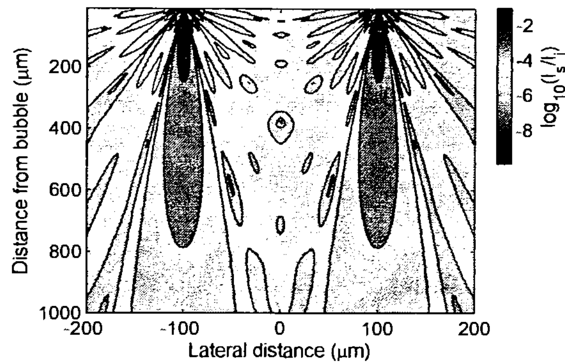

Figure 8.10 Distribution of relative scattered irradiance of 2 air bubbles 2 μm in diameter separated by 100 μm in water under unpolarized irradiation.

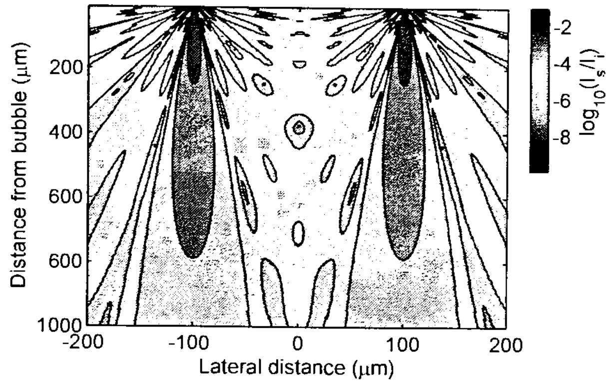

Figure 8.11 Distribution of relative scattered irradiance of 2 air bubbles 2 μm in diameter separated by 100 μm in water under TE-polarized irradiation.

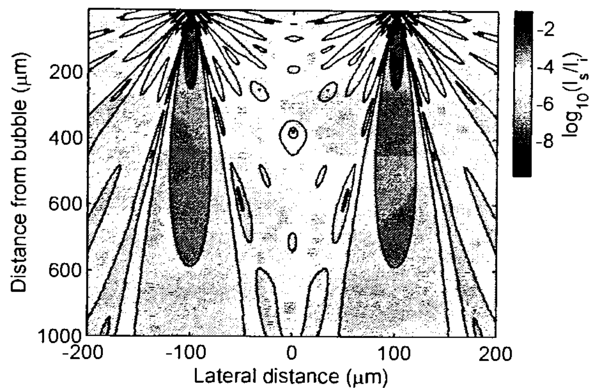

Figure 8.12 Distribution of relative scattered irradiance of 2 air bubbles 2 μm in diameter separated by 100 μm in water under TM-polarized irradiation.

In a lithographic imaging system, at least two beams are needed to resolve a useful image. That means that an air bubble in the optical path scatters two coherent incident beams. The resulting scattered irradiance is the coherent summation of the single

beam scattered irradiance. The Mie scattering patterns of two-beam scattering for an air bubble in diameter of 2 μm were plotted in Figure 8.13, Figure 8.14 and Figure 8.15 for unpolarized, TE-polarized and TM-polarized illumination for the case of numerical aperture equaling 1.2 where the oblique angle in water is 56°.

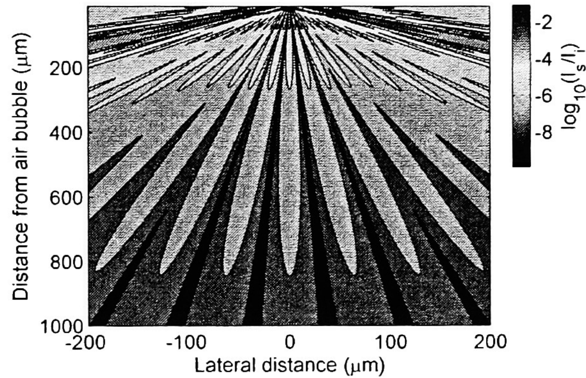

Figure 8.13 Distribution of relative scattered irradiance of an air bubble 2 μm in diameter in water illuminated by two oblique (±56°) beams without polarization.

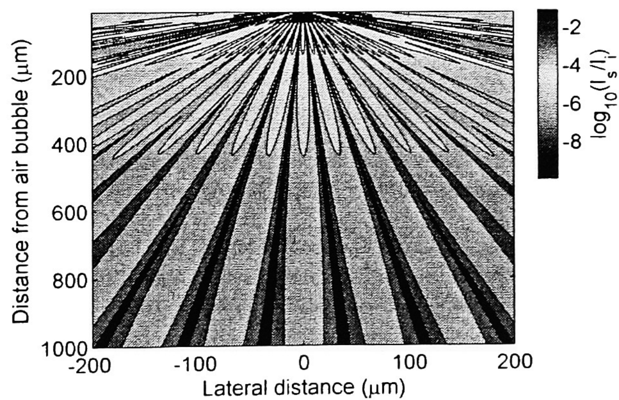

Figure 8.14 Distribution of relative scattered irradiance of an air bubble 2 μm in diameter in water illuminated by two oblique (±56°) beams with TE-polarization.

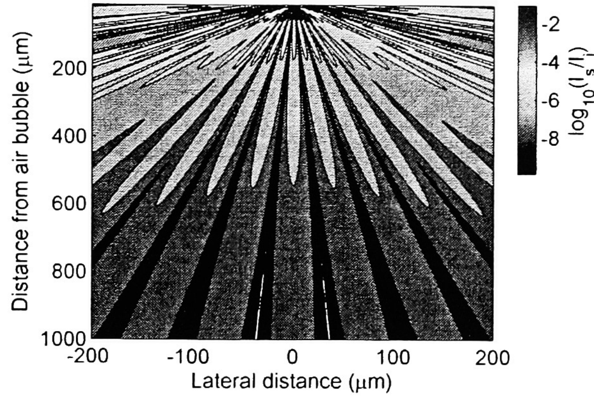

Figure 8.15 Distribution of relative scattered irradiance of an air bubble 2 μm in diameter in water illuminated by two oblique (±56°) beams with TM-polarization.

8.4 Scatter Measurements

A modified VASE (Variable Angle Spectroscopic Ellipsometry) tool was used to measure Variable Angle Scattering (VASS). The relative scattered irradiance of PST beads (2 μm in diameter, 2×10^{-4} %) at 10° off the forward direction was plotted versus wavelength in Figure 8.16. The corresponding Mie scattering calculation was plotted in Figure 8.17. The results show that our experimental measurements agree with Mie theory, so we are confident with our numerical calculations. The discrepancy between experiments and theory in the short wavelengths lies in the fact the scattered intensity is so weak that the signal is approximating the detector noises. The light source we used in the measurements is a xenon lamp, which can provide a wide spectrum of wavelength but the light is significantly weak approaching the DUV regime.

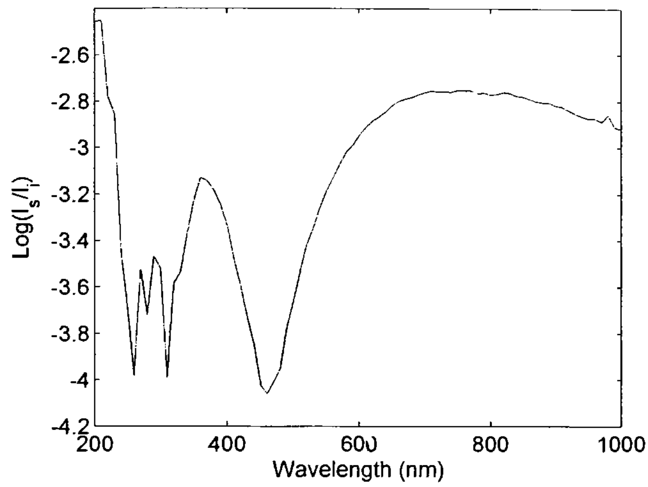

Figure 8.16 Measured relative scattered irradiance of PST beads (2 μm in diameter, 2×10^{-4} %) at 10° off the forward direction.

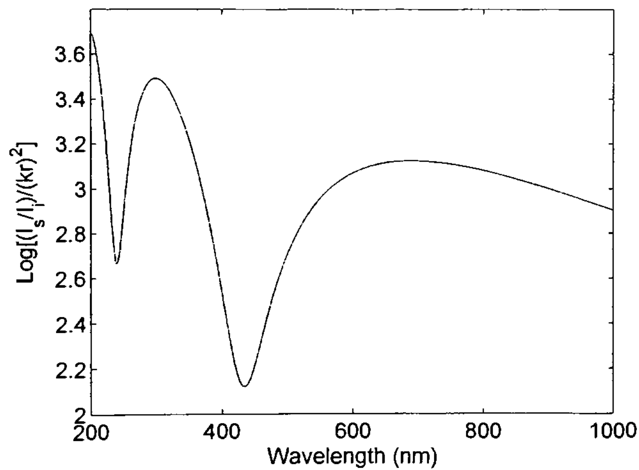

Figure 8.17 Mie Scattering calculation for PST beads (2 μm in diameter), at 10° off the forward direction.

8.5 Lithographic Imaging of "Bubbles"

The purpose of this paper is to find a clue to the question "what if there are air bubbles in water gap in immersion lithography?". The presence of air bubbles affect imaging in two ways: 1) scattering of exposure light; 2) causing defects if the bubble are actually imaged on the resist. The first issue can be characterized as "flare" while the second issue has the potential to be a yield killer. It is beneficial to understand under what circumstances the bubbles will actually be printed on the resist. Experimental studies on the imaging actual bubbles would be hard because the size and population of artificially generated air bubbles are not well controlled. Solid beads that could mimic air bubbles are therefore very interesting. Polymeric beads made of PMMA, PST, *etc* are commercially available and well characterized. However, the refractive indices of those beads are higher than those of water. The phenomenon of total reflection in the case of air bubbles will not be shown. Also, the absorption coefficient of PST beads at 193 nm is very large as compared with air bubbles. Fortunately, at the diameter size of interest, neither total reflection nor absorption on the sense of macroscopic scale would be able to exactly describe scattering behaviors. That is why Mie scattering theory is sought to calculate the scattering. Previous numerical calculations of Mie scattering in this work have suggested that PST beads are similar to air bubbles regarding to scattering patterns. Our objective is to seek a type of beads that is available to simulate the behavior of air bubbles. The calculations showed that PST beads could approximate air bubble in scatter behavior, although it is not exact. The application of polystyrene beads to mimic air bubbles will provide insights into scattering behaviors of air bubbles.

In this work, PST beads were suspended in HPLC (High Performance Liquid Chromatography) grade water which was then used as immersion lithographic media for air bubble scattering study. Our simplified hypothesis is that there is a threshold distance for a polystyrene bead of certain size, beyond which the bead will not be imaged into the resist. The hypothesis is based on very dilute concentrations, where the beads are far apart from each other so that the threshold distance is concentration independent. Therefore, concentration is only correlated with the number density of bead images in the resist.

The first experimental set-up is shown in Figure 8.18. A water gap suspended with PST spheres 2 μm in diameter is formed between a resist-coated wafer and a 0.6 mm fused silica flat plate. The thickness of the water gap is controlled by spacers with thickness larger than Λ^2/λ. A phase grating with 600 nm pitch is placed on top of the flat plate, groove side facing down. The total number of spheres that could be imaged on the resist can be calculated from the sphere concentration and the optical path length, while the total number of spheres that are eventually printed on the resist can be found out by counting the "bubble" images on the resist. The results are plotted in Figure 8.19. As shown in the figure, the total number of "bubbles" in the optical path increases proportionally with water gap thickness while the total number of imaged "bubbles" levels off at about 0.3 mm. It indicates that the "bubbles" which are 0.33 mm or farther away from the wafer will not be imaged. Figure 8.20 shows the scanning electron microscope pictures of a PST sphere and their images in resist.

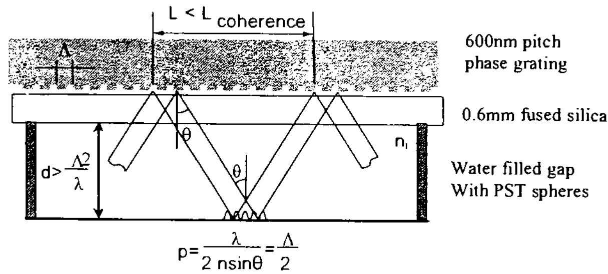

Figure 8.18 Set-up for direct lithographic imaging of "bubbles"

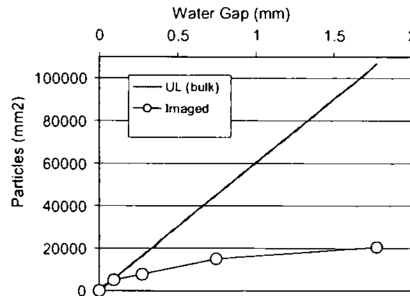

Figure 8.19 Total number of "bubbles" in optical path versus total number eventually imaged.

The second experimental set-up is shown in Figure 8.21. As shown in the figure, the laser beam is split by a phase grating into diffraction orders, ±1 orders of which are directed towards the wafer where two-beam interference occurs. The water gap suspended with PST spheres is contained between the wafer and a silica flat plat or half ball, as illustrated in the explode-up picture in Figure 8.22. The thickness of the water gap is controlled by spacers. The NA value determines the use of the flat plate or the half ball. A series of experiments were conducted at NA=0.5 with PST spheres 2 μm in diameter were conducted. Following a similar methodology as the first experiment, it is found that the "bubbles" which are 0.33 mm or farther away from the wafer will not be imaged. A SEM picture of the "bubble" and "bubble" image in resist is shown in Figure 8.23. The

results of polystyrene spheres 0.5 μm in diameter of at $2.5x10^{-5}$ weight concentration are surprising. None of the "bubbles" are actually printed in the resist, as shown in Figure 8.24, though the sphere is much larger than the line-width (100 nm). If a PST sphere was in contact with the resist, it would be printed in the resist. It is likely that the surface tension repels the PST spheres away from the resist film to the distance beyond which they will not be printed. It can be argued that this distance for a 0.5 μm PST sphere is very much smaller than 1.3 mm, beyond which PST spheres 2 μm in diameter will not print.

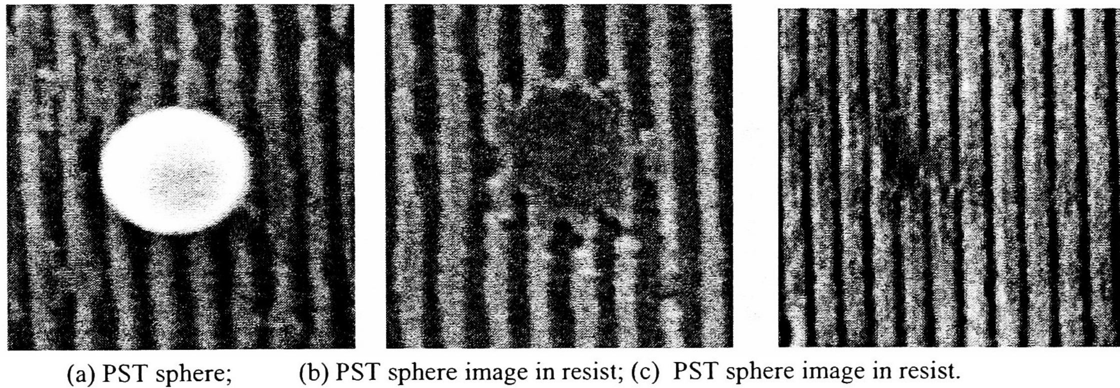

(a) PST sphere; (b) PST sphere image in resist; (c) PST sphere image in resist.

Figure 8.20 SEM pictures of a PST sphere and their image in resist.

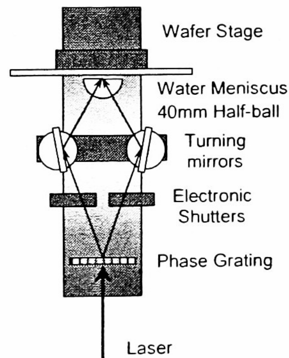

Figure 8.21 Interferometric system for "bubble" imaging.

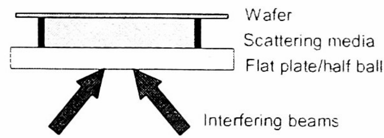

Figure 8.22 Set-up for two-beam interference through scattering media.

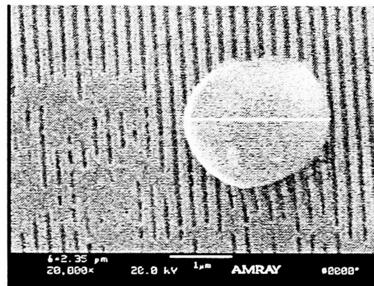

Figure 8.23 Interferometric image in water suspended with polystyrene beads of 2 μm diameter at $5x10^{-5}$ weight concentration.

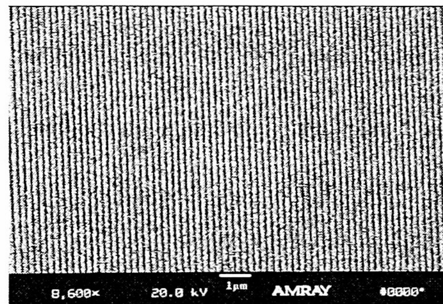

Figure 8.24 Interferometric image in water suspended with polystyrene beads of 0.5 μm diameter at $2.5x10^{-5}$ weight concentration.

8.6 Summary

In this work, scattering induced by an air bubble in water was first analyzed by geometrical optics. The total reflection of light causes the enhancement of scattering in the region where the scattering angle is less than critical scattering angle. At 193 nm, the calculated critical scattering angle is 92 degrees, indicating a strong scattering in all the forward directions. A rigorous scattering solution was numerically evaluated by partial wave (Mie) theory. Mie scattering of air bubbles was compared with that of PST and PMMA spheres at 193 nm in the cases of TE, TM or unpolarized incident light. Multiple particle scattering as well as two oblique beams scattering was also numerically computed. Analysis of the scattering patterns shows that the scattering effects of PST spheres resemble those of air bubbles in water. The Mie results of polystyrene spheres were verified by actual scatterometry measurements on a modified UV VASE tool.

Lithographic imaging of "bubbles" in an immersion water gap was studied by mimicking air bubbles with polystyrene spheres. By counting the number of "bubbles" which are actually imaged and evaluating the number of "bubbles" which are present in the optical path, the distance beyond which "bubbles" will not print can be estimated. In direct interference lithography, this distance is found to be 0.3 mm in the case of PST spheres 2 μm in diameter. In interferometric lithography at 0.5NA, this distance is estimated to be 1.3 mm in the case of PST spheres in diameter of 2 μm. Repelling of "bubbles" from the resist film by surface tension was proposed to explain the fact that PST spheres 0.5 μm in diameter will not image. The conclusion can be drawn that actual imaging of an air bubble in the resist depends on the size of the bubble and its distance from the resist film while scatter of exposure light can be characterized as "flare".

The work reveals that microbubbles are not a technical barrier to immersion lithography. Nevertheless, degassing of immersion water is very necessary. Also, consideration should be taken to minimize the possibilities of trapping air when designing water-introducing devices.

CHAPTER 9 CONCLUSIONS

This study was devoted to studying the imaging behaviors of hyper-NA optics in the context of liquid immersion and solid immersion lithography. It was also devoted to exploring the resolution limits of immersion imaging technique.

Two-beam interferometric lithography was used as a tool to study hyper-NA imaging. The full-vector interference theory was described for two-beam and multi-beam interference. The field distribution within the resist is derived using the standard thin film calculation techniques. With the built optical model, simulation examples of hyper-NA interferometric imaging were discussed with regard to some special phenomena associated with hyper-NA imaging. Polarization effects, resist absorption effects and BARC optimization were analyzed respectively.

A two beam interference setup along with a half ball, half cylinder or prism was used for interferometric immersion lithographic studies. The response the experimental setup to laser beam tilting was analyzed with a simple geometrical ray tracing technique and basic interference theory, which can serve as a vibration model to analyze the setup's tolerance on vibration. Moreover, the dependence of setup on the source's temporal coherence and spatial coherence were analyzed. It has been shown that a properly configured setup could ease the stringent temporal and spatial coherence requirements on the source.

The theoretical predictions about hyper-NA effects were verified experimentally with two-beam interferometric lithography. The verification relied on the examination of

SEM cross-sectional view of the resist film. The polarization effects were experimentally studied at 1.05NA, where the imaging behavior of TE and TM polarization is in great contrast. The experimental results agree with simulation results for TE polarization. In the case of TM polarization, the experimental results did not agree with the simple threshold model. Analysis showed that the fringe contrast difference might have contributed to the discrepancy. The optimization of bottom anti-reflection coatings (BARC) was studied experimentally. A bi-layer BARC has been shown capable of reducing standing wave effects over a broad range of oblique angles. The experimental results agree with the numerical predictions regarding BARC optimization.

To explore the resolution of immersion imaging, solid immersion lithography was investigated experimentally. An equilateral triangle prim of sapphire material was used to couple light into the resist film. The prism is capable of 1.05-1.92NA. The experimental results agreed with simulation results. The resist absorption effect increases with NA values due to that light beams traveling at higher oblique angles in the resist film experience longer optical path. Also, it has been found that the NA values can be pushed higher than the real part of the refractive index of the resist, i.e., exposing resist with "evanescent waves", but with the resist pattern limited to a thickness of only a few nanometers. The experimental results have verified the idea that solid immersion imaging is a potential technique for sub-30 nanometer lithography and is a valuable tool for hyper-NA imaging research.

As part of the dissertation, air bubble induced light scattering effects on lithographic imaging were studied. It was analyzed by geometrical optics and Mie scattering model. Analysis of the scattering patterns shows that the scattering effects of

PST spheres resemble those of air bubbles in water. Lithographic imaging of "bubbles" in an immersion water gap was studied by mimicking air bubbles with polystyrene spheres. By counting the number of "bubbles" which are actually imaged and evaluating the number of "bubbles" which are present in the optical path, the distance beyond which "bubbles" will not print can be estimated. Actual imaging of an air bubble in the resist depends on the size of the bubble and its distance from the resist film while scatter of exposure light can be characterized as "flare". The work revealed that microbubbles were not a technical barrier to immersion lithography.

APPENDIX A1

A brief description of ILSim

– A compact simulation tool for interferometric lithography

Based on the model described in the preceding section, a simulator called ILSim was built on Matlab for high NA modeling of interferometric lithography, allowing for image prediction and optimization. ILSsm's Inputs include optical constants for imaging media, thin films from the film stack and substrate, as well as imaging optics such as wavelength, polarization, demodulation, propagation angle, numerical aperture, etc. The Outputs include the image in media, 2-D image in resist, 3-D image in resist, two-pass exposure images, reflection from top surface and substrate (BARC), etc. The inputs and outputs of ILSim were summarized in Table A1-1. The interactive interface (Figure A1-1) to ILSim is used to define film stack data and imaging conditions. ILSim generates 2D and 3D intensity plot output for line/space patterns (two-and three-beam interference) and 'contact holes' (four- and five-beam interference).

Table A1-1 Summary of ILSim's inputs and outputs

ILSim Input	*ILsim Output*
Fluid properties	Image in media
Top coat	2D image in resist
Photoresist	3D image in resist
Multilayer BARCs	Two-pass exposure (top)
Substrate properties	Two-pass exposure (cross-section)
Wavelength	Polarized two-pass exposure
Polarization	Top Surface reflection
Demodulation	Substrate (BARC) reflection
Propagation angle	
Numerical aperture	

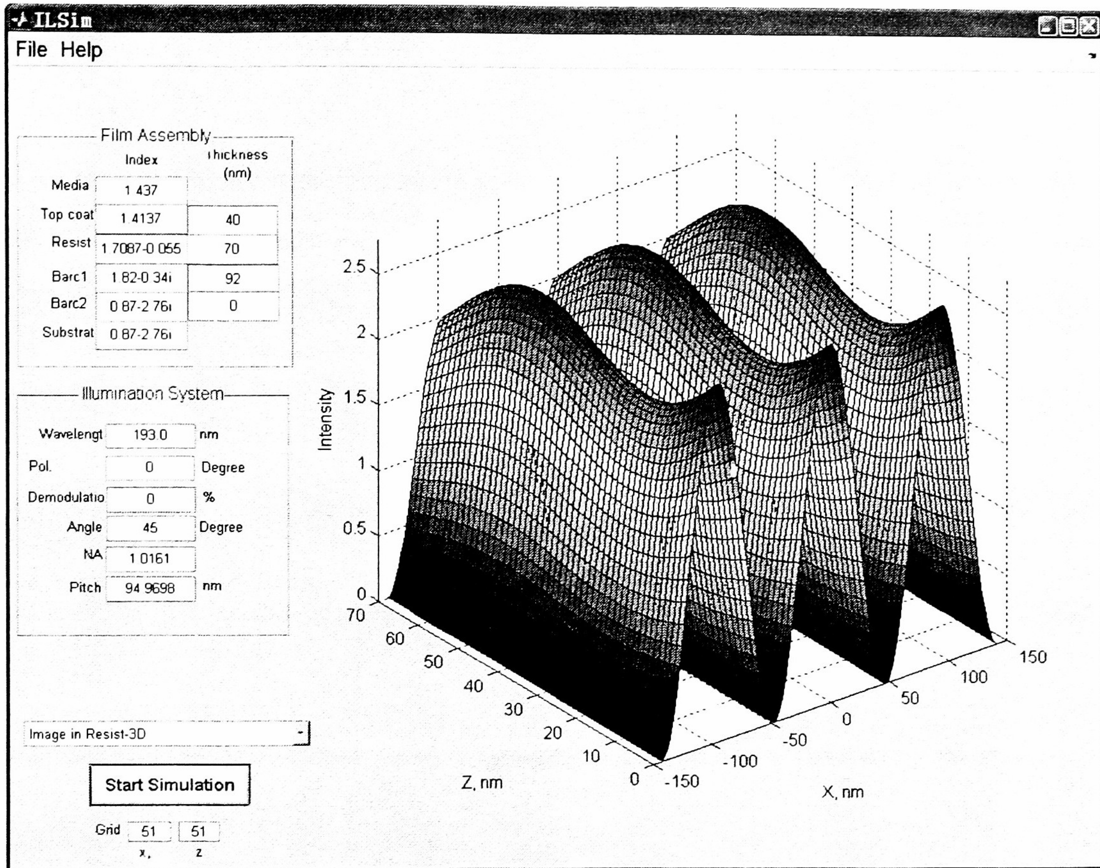

Figure A1-1 Graphical interface of ILSim.

In this appendix, a number of simulation examples are given to illustrate various features of ILSim. The imaging optics conditions and film stack parameters are listed along with the simulation plots. In the plots, x, y and z are spatial coordinates with z denoting the depth into the resist.

Example A1-1: Image in immersion media

The image in immersion media is the interferometric fringe in a uniform media in absence of a film stack. An example is shown in Figure A1-2 with the corresponding simulation parameters listed in Table A1-2.

Table A1.2 Simulation parameters for Example A1-1

Film Assembly		Optics	
Media	1.437	Wavelength	193 nm
Top coat	1.437	Polarization	TM
Resist	1.437	NA	1.05
BARC	1.437	Demodulation	0
Substrate	1.437		

EXAMPLE A1-2: 2-D image in resist

The 2-D image in resist is the plot for iso-image contours. An example is shown in Figure A1-3 with the corresponding simulation parameters listed in Table A1-3. A simulation plot for the same simulation parameters but with TM polarization is shown in Figure A1-4.

Table A1-3 Simulation parameters for Example A1-2

Film Assembly		Optics	
Media	1.437	Wavelength	193 nm
Top coat	1.414, 40nm	Polarization	TE
Resist	1.71-0.0039i, 200nm	NA	1.2
Barc	1.82-0.34i, 39nm	Demodulation	0
Substrate	0.87-2.76i		

EXAMPLE A1-3: 3-D image in resist

The 3-D image in resist is the surface plot for light intensity distribution within the resist. An example is shown in Figure A1-5 with the corresponding simulation parameters listed in Table A1-3.

EXAMPLE A1-4: Image contrast in resist

The image contrast in resist is plotted against the thickness of the resist. An example is shown in Figure A1-6 with the corresponding simulation parameters listed in Table A1-3 but with TM polarization.

EXAMPLE A1-5: 2-Pass exposure with orthogonal/parallel polarization

The wafer is exposed once, then it is turned 90 degree for a second-pass exposure. If the polarization direction remains the same for the second exposure, it is called orthogonal polarization 2-pass exposure configuration. If the polarization direction is turned 90degree for the second exposure, it is called parallel polarization 2-pass exposure configuration. The iso-image contours of a top-down view or cross-section of the resist can be simulated as illustrated in Figure A1-7 and Figure A1-8. The corresponding simulation parameters listed in Table A1-3.

EXAMPLE A1-6: Reflection from top surface and substrate (BARC)

The reflection from the top surface and the substrate (BARC) as a function of top layer thickness or BARC thickness can be simulated for optimal thickness. An example is shown in Figure A1-9 and Figure A1-10. The reflection for both TE and TM is shown. An optical thickness for TE polarization is shown in the plot. The corresponding simulation parameters listed in Table A1-3.

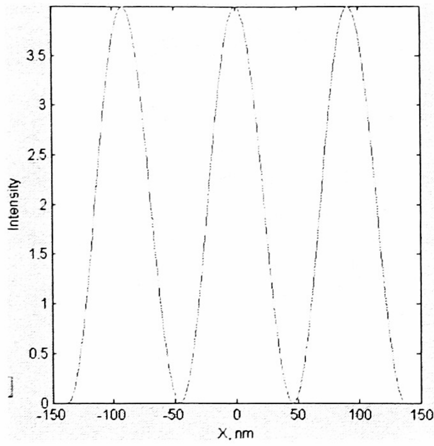

Figure A1-2 Image in immersion media.

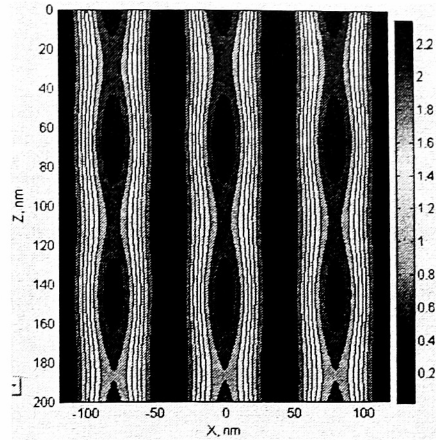

Figure A1-3 2-D image in resist.

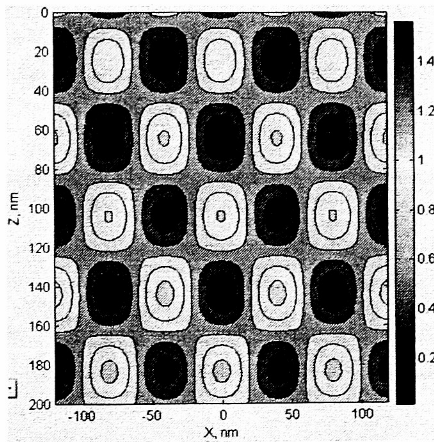

Figure A1-4 2-D image in resist.

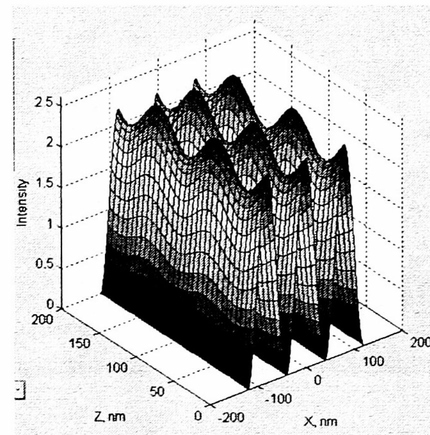

Figure A1-5 3-D image in resist.

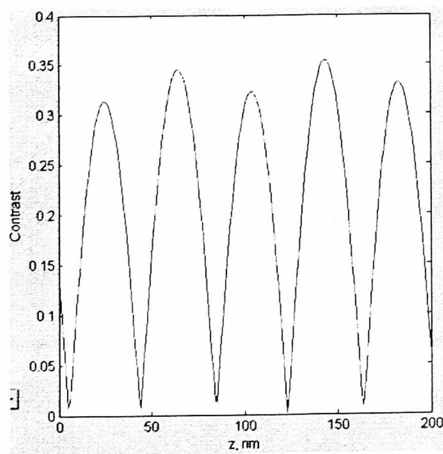

Figure A1-6 Image contrast in resist.

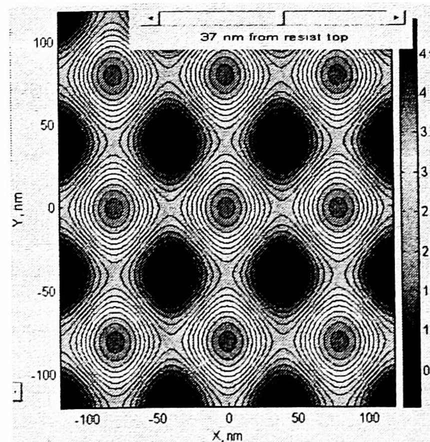

Figure A1-7 2-Pass, orthogonal pol., top down.

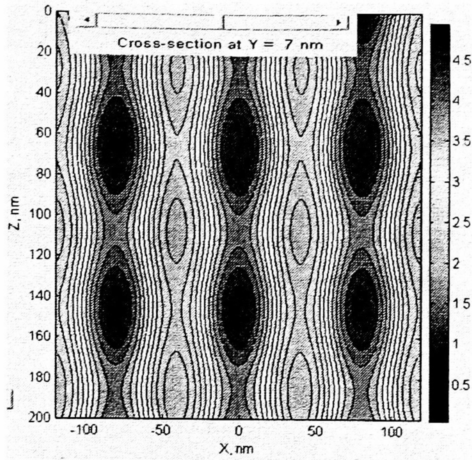

Figure A1-8 2-Pass, orthogonal pol., cross-section.

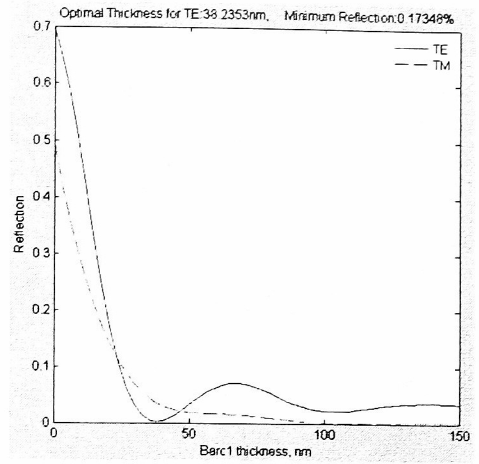

Figure A1-9 Substrate (BARC) reflection.

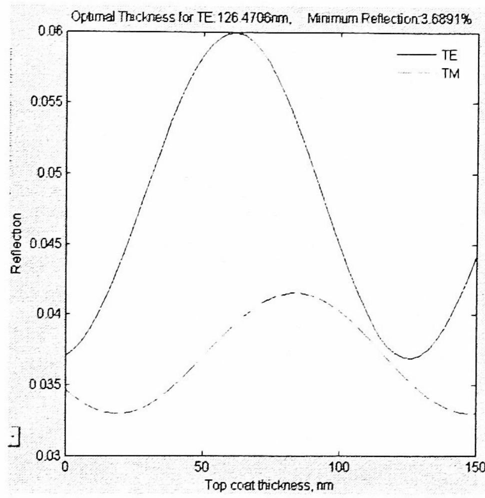

Figure A1-10 Top surface reflection.

APPENDIX A2 Programming Flowchart for ILSim

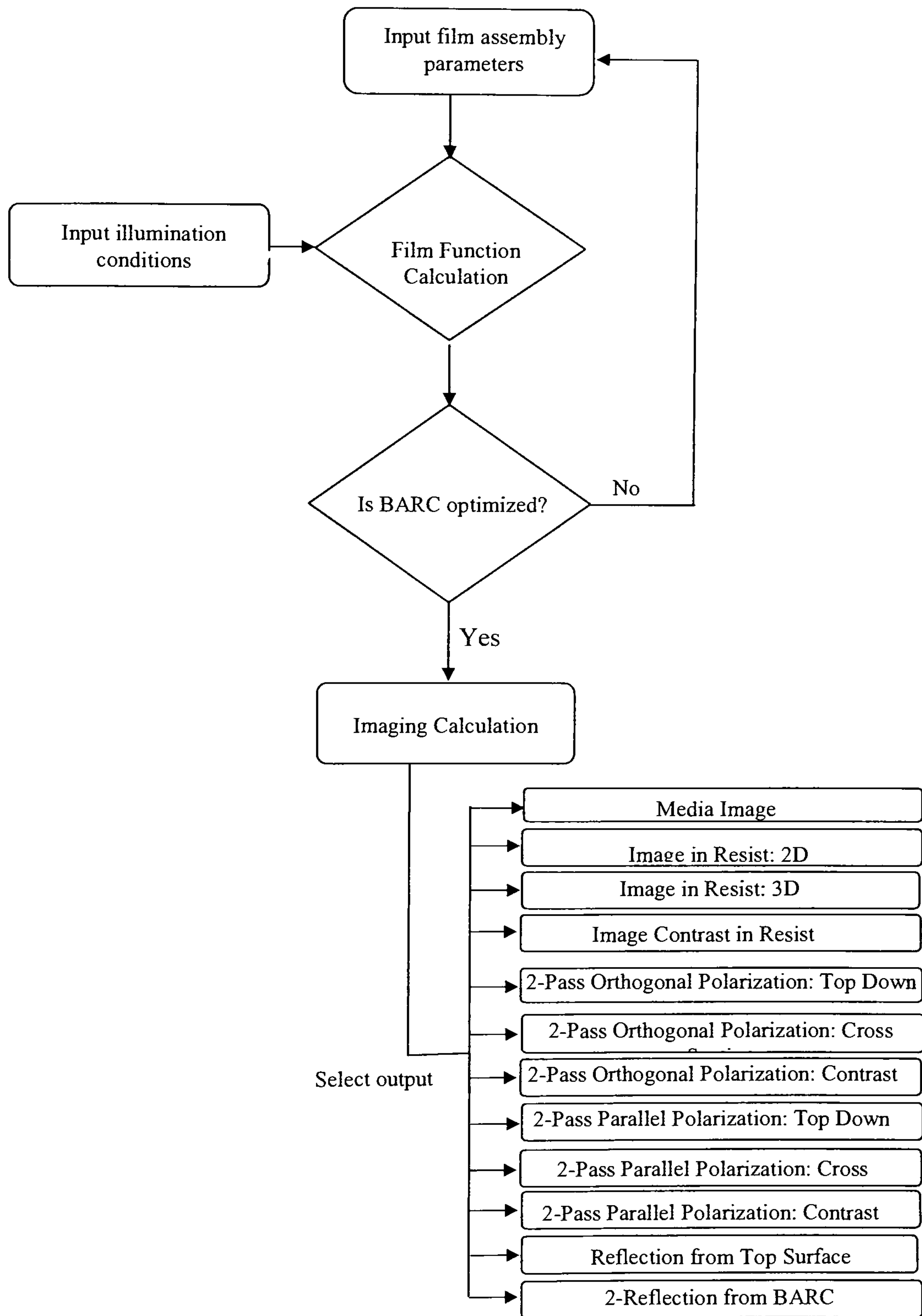

REFERENCES

1. F. Maloberti, P. Malcovati, "Microsystems and smart sensor interfaces: A review," Analog Integrated Circuits and Signal Processing **15**, 9-26 (1998).
2. G. E. Moore, "Lithography and the future of Moore's law," in *Electron-Beam, X-Ray, EUV, and Ion-Beam Submicrometer Lithographies for Manufacturing V*, John M. Warlaumont ed., Proc. SPIE **2439**, 2-17 (1995).
3. B. W. Smith, "Optics for Photolithography," in *Microlithography Science and Technology*, J. R. Sheats, B. W. Smith, eds. (Marcel Dekker, 1998) , pp172.
4. B. W. Smith, "Optics for Photolithography," in *Microlithography Science and Technology*, J. R. Sheats, B. W. Smith, eds. (Marcel Dekker, 1998) , pp209.
5. A. M. Hawryluk, N. M.Ceglio, D. A. Markle, "EUV lithography," Solid State Technology **40**, 75-78 (1997).
6. A. M. Hawryluk, N. M.Ceglio, D. A. Markle, "EUV lithography," Solid State Technology **40**, 151-159 (1997).
7. A. M. Hawryluk, N. M.Ceglio, D. A. Markle, "EUV lithography," Microlithography World **6**(3), 17-22 (1997).
8. B. Fay, "Advanced optical lithography development, from UV to EUV," Microelectronic Engineering **61-62**, 11-24 (2002).
9. N. N. Matsuzawa, S. Okazaki, A. Ishitani, "Researching photoresist materials for F2 (157nm) and EUV (13nm)," Microlithography World **9**(4), 20-22, 28 (2000).
10. C. Wagner, W. Kaiser, J. Mulkens, D. G. Flagello, "Technical considerations of extending optical lithography," Solid State Technology **43**(9), 97-108 (2000).

11. T. Yamazaki, T. ltani, "157-nm Resist Material Design for Improvement of lts Transparency Using Highly Precise Theoretical Calculation," Jpn. J. Appl. Phys. **42**, 3881-3884 (2003).

12. K. Ronse, P. De Bisschop, A. M. Goethals, J. Hermans, R. Jonckheere, S. Light, U. Okoroanyanwu, R. Watso, D. McAfferty, J. Ivaldi, T. Oneil, H. Sewell, "Status and critical challenges for 157-nm lithography," Microelectronic Engineering **73-74**, 5-10 (2004).

13. F. Eschbach, A. Tregub, K. Orvek, C. Foster, F. Lo, 1. Matsukura, N. Tsushima, "Development of polymer membranes for 157 nm lithography," in *Optical Microlithography XVII*, B. W. Smith ed., Proc. SPIE **5377**, 1627-1640 (2004).

14. A. Engel, K. Knapp, L. Aschke, E. Morsen, W. Triebel, C. Chojetzki, S. Bruckner, "Development and investigation of high quality CaF2 used for 157 nm micro lithography," in *Optical Microlithography XIV*, J. P. Christopher ed., Proc. SPIE **4346**, 1183-1189 (2001).

15. N. Seong, K. Lai, A. E. Rosenbluth, G. Gallatin, "Assessing the impact of intrinsic birefringence on 157nm lithography," in *Optical Microlithography XVII*, B. W. Smith ed., Proc. SPIE **5377**, 99-103 (2004).

16. J. A. Mcclay, A. S. L. Mcintyre, "157nm optical lithography: The accomplishments and the challenges," Solid State Technology **42**(6), 57-68(1999).

17. H. Nakano, H. Hata, H. Nogawa, N. Deguchi, M. Kohno, Y. Chiba, "Development status of a 157nm full field scanner," in *Optical Microlithography XVI*, A. Yen ed., Proc. SPIE **5040**, 763 -771 (2003).

18. S. Yamada, S. Cho, A. Zampini, "Design and study of resist materials for 157nm lithography," in *Optical Microlithography XVI*, A. Yen ed., Proc. SPIE **5039I**, 569 - 579 (2003).

19. P. A. Zimmerman, P. C. Van Peski, D. Miller, R. P. Callahan, M. Cashion, "Production of novel materials for 157nm and 193nm soft pellicles," in *Optical Microlithography XVII*, B. W. Smith ed., Proc. SPIE **5377**, 124-130 (2004).

20. F. M. Schellenberg, "Resolution enhancement technology: The past, the present, and extensions for the future," in *Optical Microlithography XVII*, B. W. Smith ed., Proc. SPIE **5377**, 1-20 (2004).

21. L. Liebmann, "Resolution enhancement technoniques in optical lithography, it's not just a mask problem," in *Photomask and next-generation lithography mask technology VIII*, H. Kawahira ed., Proc. SPIE **4409**, 23-32 (2004).

22. C. Mack, "Resolution enhancement technologies," Microlithography World **12**(2), 14-16, (2003).

23. H. Levinson, "Confronting the diffraction limit," in *Principles of Lithography* (SPIE Press, 2005), pp. 273-308.

24. B. W. Smith, "Optics for Photolithography," in *Microlithography Science and Technology*, J. R. Sheats, B. W. Smith, eds. (Marcel Dekker, 1998) , pp. 235-237.

25. C. Mack, "Off-axis illumination," Microlithography World **12**(3), 14-16, (2003).

26. Y. Granik, "Illuminator optimization methods in microlithography," in Novel *Optical Systems Design and Optimization VII*, Proc. SPIE **5524**, 217-229 (2004).

27. Y. Granik, "Source optimization for image fidelity and throughput," Journal of Microlithography, Microfabrication and Microsystems **3**(4), 509-522 (2004).

28. W. N. Partlo, P. J. Tompkins, P. G. Dewa, P. F. Michaloski, "Depth of focus and resolution enhancement for i-line and deep-UV lithography using annular illumination," in *Optical/Laser Microlithography VI*, Proc. SPIE **1927**, 137-157 (1993).

29. S. Hsu, M. Eurlings, E. Hendrickx, D. Van Den Broeke, T. B. Chiou, J. F. Chen, T. Laidig, X. Shi, J. Finders, "Double dipole lithography for 65nm node and beyond: A technology readiness review," in *Photomask and Next-Generation Lithography Mask Technology XI*, Proc. SPIE **5446**, 481-498 (2004).

30. J. Garofalo, C. J. Biddick, R. L. Kostelak, S. Vaidya, " Mask assisted off-axis illumination technique for random logic," J. Vac. Sci. Technol. B. **11**(6), 2651-2658 (1993)

31. M. D. Levenson, "Extending the lifetime of optical lithography technologies with wavefront engineering," Jpn. J. Appl. Phys. **33**, 6765-6773 (1994).

32. E. Tamechika, T. Horiuchi, K. Harada, "Resolution improvement using auxiliary pattern groups in oblique illumination lithography," Jpn. J. Appl. Phys. **32**(12B), 5856-5862 (1993).

33. M. D. Levenson, N. S. Viswanathan, R. A. Simpson, "Improving resolution in photolithography with a phase-shifting mask," IEEE Transactions on Electron Devices **ED-29**(12), 1828-1836 (1982).

34. C. Mack, "Depth-of-focus and the alternating phase-shift mask," Microlithography World **13**(4), 20-21 (2004).

35. J. F. Chen, D. Van Den Broeke, M. Hsu, T. Laidig, K. E.Wampler, X. Shi, S. Hsu, T. Shafer, "Mask design optimization for 70 nm technology node using chromeless

phase lithography (CPL) based on 100% transmission phase shifting mask," in *Photomask and Next Generation Lithography Mask Technology IX*, Proc. SPIE **4754**, 361-372 (2002).

36. M. D. Levenson, D. S. Goodman, S. Lindsey, P. W. Bayer, H. A. E. Santini, "The phase-shifting mask II: Imaging simulations and submicrometer resist exposures," IEEE Transactions on Electron Devices **ED-31**(6), 1828-1836 (1984).

37. J. F. Chen, J. S. Petersen, R. Socha, T. Laidig, K. E. Wampler, K. Nakagawa, G. Hughes, S. MacDonald, W. Ng, "Binary halftone chromeless PSM technology for λ/4 optical lithography," in *Optical Microlithography XIV*, Proc., SPIE **4346**, 515-533 (2001).

38. D. Van Den Broeke, J. F. Chen, T. Laidig, S. Hsu, K. E. Wampler, R. Socha, J. S. Peterson, "Complex two-dimensional pattern lithography using chromeless phase lithography," J. Microlith., Microfab., Microsyst. **1**(3), 229-242 (2002).

39. B. W. Smith, "Optics for Photolithography," in *Microlithography Science and Technology*, J. R. Sheats, B. W. Smith, eds. (Marcel Dekker, 1998) , pp. 253.

40. H. Kawahira, N. Hayashi, H. Hamada, "PMJ'99 panel discussion review: OPC mask technology for KrF lithography," in *19th Annual BACUS Symposium on Photomask Technology*, Proc., SPIE **3873**, 318-327 (1999).

41. T. Kotani, S. Tanaka, K. Yamamoto, S. Kobayashi, T. Uno, S. Inoue, "Highly accurate process proximity correction based on empirical model for 0.18 μm generation and beyond," Japanese Journal of Applied Physics, Part 1: Regular Papers and Short Notes and Review Papers **38**(12B), 6957-6962 (1999).

42. B. W. Smith, H. Kang, A. Bourov, F. Cropanese, Y. Fan, "Water immersion Optical Lithography for the 45 nm node," in *Optical Microlithography XVI*, A. Yen eds. Proc., **SPIE** 5040, 679-689 (2003).

43. B. W. Smith, A. Bourov, H. Kang, F. Cropanese, Y. Fan, N. Lafferty, L. Zavyalova, "Water immersion optical lithography at 193 nm," J. Microlith., Microfab., Microsyst. **3**(1), 44-51 (2004).

44. B. W. Smith, Y. Fan, M. Slocum, L. Zavyalova, "25 nm immersion lithography at 193 nm wavelength," B. W. Smith ed., in *Optical Microlithography XVII*, B. W. Smith ed., Proc. SPIE **5754**, 141-147 (2005).

45. B. W. Smith, Y. Fan, J. Zhou, A. Bourov, L. Zavyalova, N. Lafferty, F. Cropanese, A. Estroff, "Hyper NA water immersion lithography at 193 nm and 248 nm," Journal of Vacuum Science and Technology B: Microelectronics and Nanometer Structures **22**(6), 3439-3443 (2004).

46. B. J. Lin, "Immersion lithography and its impact on semiconductor manufacturing", in *Optical Microlithography XVII*, B. W. Smith ed., Proc. SPIE **5377**, 46-66 (2004).

47. S. R. J. Brueck, A. M. Biswas, "Extension of 193-nm immersion optical lithography to the 22-nm half-pitch node," in *Optical Microlithography XVII*, B. W. Smith ed., Proc. SPIE **5377**, 1315-1322 (2004).

48. J. A. Hoffnagle, W. D. Hinsberg, M. Sanchez, F. A. Houle, "Liquid immersion deep-ultraviolet interferometric lithography," J. Vac. Sci. Technol. B **17**(6), 3306-3309 (1999).

49. S. Owa, H. Nagasaka, Y. Ishii, O. Hirakawa, T. Yamamoto, "Feasibility of immersion lithography," in *Optical Microlithography XVII*, B. W. Smith ed., Proc. SPIE **5377**, 264-272 (2004).

50. M. Cheng, B. Ho, R. Yamaguchi, K. Yoshioka, H. Yaegashi, "Optical coupling of lens, liquid and resist in immersion lithography: Rigorous model and assessment," in *Optical Microlithography XVII*, B. W. Smith ed., Proc. SPIE **5377**, 405-414 (2004).

51. B. J. Lin, "The k_3 coefficient in nonparaxial λ/NA scaling equations for resolution, depth of focus, and immersion lithography," J. Microlith., Microfab., Microsyst., **1**(1), 7-12 (2002).

52. S. Owa, H. Nagasaka, "Immersion lithography: its potential performance and issues," in *Optical Microlithography XVI*, A. Yen ed., Proc. SPIE **5040**, 724-732 (2003).

53. J. Zhou, Y. Fan, A. Bourov, N. Lafferty, F. Cropanese, L. Zavyalova, A. Estroff and B. W. Smith, "Immersion lithography fluids for high NA 193 nm lithography," in *Optical Microlithography XVIII*, B. W. Smith ed., Proc. SPIE **5754,** 630-637 (2005).

54. J. H. Burnett and S. Kaplan, "Measurement of the refractive index and thermo-optic coefficient of water near 193 nm, " in *Optical Microlithography XVI*, A. Yen ed., Proc. SPIE **5740,** 1742-1749 (2003).

55. E. D. Palik, *Handbook of optical constants of solids* (Academic Press, San Diego, 1998).

56. T. Chen, T. D. Milster, D. Nam and S. H. Yang, "Experimental investigation of solid immersion lens lithography," in *Optical Microlithography XVIII*, B. W. Smith ed., Proc. SPIE **5754,** 254-261 (2005).

57. T. D. Milster, J. S. Jo, K. Hirota, K. Shimura and Y. Zhang, " The nature of the coupling field in optical data storage using solid immersion lenses," Jpn. J. Appl. Phys.**38**, 1793-1794 (1999).

58. S. Tang and T. D. Milster, "Consideration and control of writing conditions with near-field aperture solid immersion lens probe," Jpn. J. Appl. Phys. **42**, 1090-1094 (2003).

59. T. D. Milster, J. S. Jo and K. Hirota, "Roles of propagating and evanescent saves in solid immersion lens systems," Applied Optics **38**, 5046-5056 (1999).

60. T. R. Corle, G. S. Kino. "Lithography system employing a solid immersion lens", **US** 5,121,256.

61. H. A. Macleod, *Thin-film optical filters* (Macmillan Publishing Company, 1985).

62. D. G. Flagello, "High numerical aperture imaging in homogeneous thin films," Ph.D. Dissertation, University of Arizona, 1993.

63. D. G. Flagello, T. D. Milster, "High-numerical-aperture effects in photoresist," Applied Optics **36**, 8944-8951 (1997)

64. D. G. Flagello, T. D. Milster, A. E. Rosenbluth, "Theory of high-NA imaging in homogeneous thin films," J. Opt. Soc. Am. A **13**, 53-64 (1999).

65. R. F. Delmdahl, "Pulsed excimer lasers for thin film applications," in *Fifth International Symposium on Laser Precision Microfabrication*, Proc. SPIE **5662**, 655-660 (2004).

66. J. Woollam, B. Johs, C. Herzinger, J. Hilfiker, R. Synowicki, C. Bungay, "Overview of variable angle spectroscopic Ellipsometry, Pat 1: basic theory and typical applications," Optical metrology **CR72**, 3-28 (1999).

67. J. Woollam, B. Johs, C. Herzinger, J. Hilfiker, R. Synowicki, C. Bungay, "Overview of variable angle spectroscopic Ellipsometry, Pat I: basic theory and typical applications," Optical metrology **CR72**, 29-58 (1999).

68. H. Krebs, Fundamentals of inorganic crystal chemistry (McGraw-Hill 1968), pp243

69. M. Born, E. Wolf, *Principles of Optics* (Cambridge University Press, 2001), pp.50.

70. A. Espanet, C. Ecoffet, D. J. Lougnot, "PEW: Photopolymerization by evanescent wves. II Revealing dramatic inhibiting effects of oxygen at submicrometer scale", J. of Polymer Science Part A: Polymer Chemistry, **37**, 2075-2085 (1998).

71. C. Ecoffet , A. Espanet, D. J. Lougnot, " Photopolymerization by evanescent waves: a new method to obtain nanoparts", Advanced Materials, **10**(5), 411-414 (1998).

72. S. Sainov, "Nanoscale surface-wave holographic recording", J. Phys.: Condens. Matter, **11**, 9857-9860 (1999).

73. K. G. Muller, S. Sainov, S. Mittler-Neher, W. Knoll, "Evanscent (surface) wave holographic recording thin polymeric film", ", J. Phys.: Condens. Matter, **11**, 9851-9855 (1999).

74. S. Sainov, A. Espanet, C. Ecoffet, D. J. Lougnot, "High spatial frequency evanescent wave holographic recording in photopolymers", J. Opt. A: Pure Appl. Opt., **5**, 142-146 (2003)

75. T. S. Gau, C. K. Chen, and B. J. Lin, ''The image characterization of bubbles in water for 193-nm immersion lithography,'' J. Microlithogr., Microfabr., Microsyst. **3**(1), 61–67 (2004).

76. Y. Fan, N. V. Lafferty, A. Bourov, L. V. Zavyalova, and B. W. Smith ", Air Bubble Induced Light Scattering Effect On Image Quality in 193 nm Immersion Lithography, " Applied Optics, **44**, 3904-3011 (2005).

77 P. L. Marston, "Light scattering from bubbles in water," in *Proceedings of Oceans 89*, Publication 89CH2780-5 (Institute of Electrical and Electronics Engineers, Piscataway, N.J., 1989), pp. 1186–1193

78. C. F. Bohren, D. R. Huffman, "Absorption and scattering by a sphere," in *Absorption and Scattering of Light by Small Particles* (John Wiley & Sons, 1998), pp. 82-129.